Rip Current Dynamics and Nearshore Circulation

by

Merrick C. Haller

and

Robert A. Dalrymple

RESEARCH REPORT NO. CACR-99-05

August, 1999

Center for Applied Coastal Research
Ocean Engineering Laboratory
University of Delaware
Newark, DE 19716

ACKNOWLEDGMENTS

This research was sponsored by the Office of Naval Research Coastal Dynamics Program grants N00014-95-1-0075 and N00014-98-1-0521.

This work was originally submitted as a dissertation by Merrick C. Haller in the Summer of 1999 to the Faculty of the University of Delaware in partial fulfillment of the requirements for the degree of Doctor of Philosophy in Civil Engineering. The color plots contained in the dissertation are reproduced in black and white in this report. Copies of the color plots can be obtained by contacting the first author directly.

TABLE OF CONTENTS

LIST OF FIGURES

LIST OF TABLES

ABSTRACT

In this dissertation previous field observations of rip currents are reviewed along with rip current forcing mechanisms. Next, a laboratory experiment is detailed. The physical model consists of a longshore bar on a planar beach with two rip channels located at 1/4 and 3/4 of the basin width. Results from the experimental investigation demonstrate the presence of two circulation systems; a primary system consisting of longshore feeder currents and a strong offshore directed rip current, and a secondary system, rotating in the opposite direction, consisting of flows driven away from the rip channel and located shoreward from the primary system. The relationship between incident wave conditions and the nearshore currents are also described.

The experiments also clearly demonstrate the presence of low frequency rip current oscillations. These motions are shown to be restricted to regions of strong rip current flow and are highly suggestive of a jet instability mechanism. Finally, an analytic model for the rip current mean flows is developed and its linear stability characteristics are investigated. The linear stability model includes the effects of increasing depth in the flow direction and of bottom friction. The model results strongly suggest that much of the low frequency rip current motion can be explained by a linear instability mechanism.

Chapter 1

INTRODUCTION

The nearshore is an active zone that can be quite inhospitable to humans due to violent wave breaking and dangerous rip currents. Study of the nearshore is also important in areas where the coastline is heavily developed and prediction and possible mitigation of coastal erosion are valid concerns of the general public. An understanding of nearshore processes is also needed for the management of harbors and inlets as the nearshore dynamics have a dominant influence on navigation and accessibility and can have a significant impact on the strategic, economic, and environmental interests of our society.

In general, the coastal scientist is concerned with large scale fluid motions such as long waves which can have wavelengths approaching 1000 m, and yet, must also have a working knowledge of the forces that initiate motion in sand grains of 1 mm scale. The complex suite of motions prevalent in the nearshore includes surf beat, storm surge, and edge waves. In addition, large enclosed basins may contain inertial modes, seiche modes, and density driven currents. Strong nearshore currents can take the form of rip currents, undertow, longshore currents, and tidal jets. Much of the dynamics is driven by the breaking of wind generated waves, but this can be complicated by the modulation of the incident waves and their tendency to organize themselves into groups; and by a complex interaction between the bathymetry, the incident waves, and the larger scale shelf/estuarine dynamics. It is these complex fluid motions which drive the similarly complex nearshore morphology and give rise

to features such as crescentic bars, tidal shoals, rip channels, mega-ripples, and beach cusps and which govern the overall sediment budget.

In this context, the present study will concentrate on the dynamics of rip currents and their influence on nearshore circulation. Rip currents are distinct offshore directed flows which can be quite strong (O(1 m/s)) and have been known to extend more than 1000 m offshore. The presence of rip currents tends to dominate the nearshore current system and thus has a direct impact on the transport and deposition of sediments and swimmers. Since field measurements of rip currents can be very difficult to obtain, because rips tend to have short residence times (O(10 min)) and can migrate longshore, we will investigate rip currents in the laboratory environment.

Our study on rip currents also has applications to the study of tidal jets. Tidal jets are the strong outward directed flow found at tidal inlets during ebb tide. Both rip currents and tidal jets usually act as shallow water, turbulent jets or, more simply, nearshore jets. Tidal entrances such as inlets and bay mouths serve as conduits through which estuarine waters mix and exchange with the coastal ocean. These jets influence the distribution of sediments and can determine the fate of artificially introduced pollutants.

The concepts we will focus on include the effects of periodic rip channels on the nearshore circulation found on barred beaches, the relationship between the incident wave field and the strength of rip currents, and the source of unsteady rip currents. The work is motivated directly by the lack of experimental data that quantifies the effect of longshore varying bathymetry on the forcing of longshore currents. In addition, the experiments have given insight into the role of wave-current interaction in the presence of rip currents, and demonstrated that rip currents can be unstable, which is a previously unexamined phenomenon.

1.1 Effects of longshore variability on the longshore momentum balance

The analysis of the longshore momentum balance in the surf zone is a very active area of nearshore research. One of the many intriguing questions involves the discrepancy between present models of wave-induced longshore currents on barred beaches and field measurements. Specifically, present models tend to predict local longshore current maxima at the bar crest and near the shoreline, while field data often show only one maximum located in the bar trough. The effects of longshore pressure gradients induced by longshore varying morphology tend to be overlooked in longshore current models, however, there is a significant body of work which has addressed the problem.

The works of Gourlay (1976), Keeley and Bowen (1977), and Wu *et al.* (1985) investigated the effects of longshore nonuniformities of wave breaking heights on the longshore current and found them to be significant. Mei and Liu (1977) solved for the wave-induced mean currents in the case of normally incident waves and gave a qualitative picture of the nearshore circulation patterns. Dalrymple (1978) suggested that the longshore gradient of mean water levels, induced by a longshore bar with periodic rip channels, could drive a strong longshore current in the bar trough. Putrevu *et al.* (1995) further generalized the work of Mei and Liu (1977) and showed that longshore mean water level gradients could contribute a forcing of longshore currents comparable to that of longshore wave height variations.

Our work seeks to quantify the longshore mean water level gradients induced by longshore bathymetric nonuniformities. There is a significant lack of experimental data that addresses longshore nonuniformities, a somewhat surprising fact, since the previous studies have indicated that longshore variability plays a significant role in the nearshore circulation. The present study presents a comprehensive data set that should serve as a vital resource for evaluating present nearshore circulation models.

1.2 Rip current stability

The unsteadiness of nearshore currents is a topic that has received much recent interest. Long period current oscillations due to edge waves and wave groups have been well known for at least two decades. Shear waves, induced by a hydrodynamic instability of the longshore current (Bowen and Holman, 1989) have received the most attention in the very recent past. These vorticity motions have a wavelike signature in longshore current measurements and are driven by the shear in the cross-shore profile of the longshore current.

Rip currents also exhibit long period oscillations (e.g. Sonu, 1972; Bowman *et al.* 1988; and many others). These oscillations have always been attributed to long period modulations in incoming wave heights. However, rip currents are analogous to plane jets, since they are generally long and narrow and flow offshore into relatively quiescent waters. Hydrodynamic jets have long been known to exhibit instabilities (Bickley, 1939;Drazin and Howard, 1966), and the work herein is heavily based on this long history of hydrodynamic stability theory. We will apply classical approaches for the analysis of turbulent jets in our application to the hydrodynamic stability of rip currents.

1.3 Outline of present work

This dissertation is organized as follows: in Chapter 2 we review the literature regarding rip current observations and rip current generation theory. It is evident from the review that there is a considerable quantity of field-based rip current observational work, however, it is mostly qualitative in nature. Also, based on the review, we divide the models for rip current generation into two categories: forced and unforced circulations, and these are described in detail.

In Chapter 3 we describe the laboratory facilities and the wave basin that were utilized in our experimental modeling. The physical model is described and the results of the experiments are detailed for the time-averaged motions only.

In Chapter 4 we discuss the presence of low frequency rip current motions. Data are presented that clearly indicate significant low frequency motion associated with strong rip currents. The natural seiche modes of the wave basin are computed and shown to not significantly affect the experiments.

In Chapter 5 we present an analytic model for the rip current based on self-similar turbulent jet theory. The model is used to investigate the stability characteristics of rip currents, including the importance of bottom slope and other nonparallel effects. The model is then applied to the experimental results and the comparison strongly suggests that rip currents exhibit jet instabilities.

Finally, in Chapter 6 we summarize our conclusions and give suggestions for future research.

Chapter 2

RIP CURRENTS: A REVIEW

2.1 Introduction

Rip currents have captured the interest of nearshore scientists for most of this century. Even the casual beachgoer is likely familiar with the hazards of rip currents and any seasoned lifeguard is trained in rip current safety. To the non-scientist rip currents often seem mysterious and unpredictable; appearing suddenly and snatching swimmers out to sea. However, in the last half of this century there has been a considerable effort to understand the nature of rip currents, their causes and effects. A vast majority of this work has been observational and qualitative, yet, recent theoretical and computational advances have also enabled researchers to perform some quantitative analyses and postulate complex rip current generation mechanisms.

The influence of rip currents is not limited to public safety issues, rip currents can also have dramatic effects on the general coastal environment. The presence and persistence of rip currents modifies the incident wave environment, the circulation of water in the surf zone, the direction of sediment transport, and ultimately the shape of the coastline. In this chapter much of the existing literature on rip currents will be reviewed in order to discuss three subjects: 1) what constitutes a rip current 2) how do rip currents affect nearshore morphology and 3) what are the driving forces that produce rip currents and determine where rip currents form.

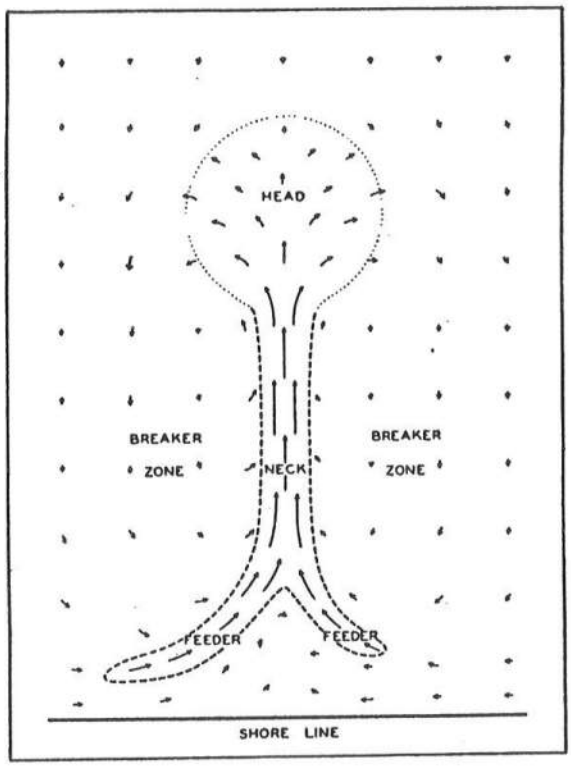

Figure 2.1: Diagram of a rip current showing its component parts and associated current vectors (from Shepard *et al.* , 1941).

2.2 What is a rip current?

A rip current is a narrow, seaward directed current which extends from the inner surf zone out through the line of breaking waves. In general, rip currents return the water carried landward by waves and, under certain conditions of nearshore slope and wave activity, rip currents are the primary agent for seaward drainage of water. The distinction between undertow, which is the milder, diffuse, near-bottom return current omnipresent under breaking waves, and rip currents, which are narrow (extending 10-20 m in the longshore direction) and often confined to the upper reaches of the water column, had been muddled in the scientific literature during the early part of this century. F. P. Shepard was the first to address the

issue directly, and the term rip current was first coined by him in a 1936 article in the journal *Science.*

A more complete general description of rip currents was given by Shepard *et al.* (1941). Those authors, using visual observations of rip currents seen off the coast of La Jolla, California, described rip currents as having three major features: the *feeder*, the *neck*, and the *head.* A representative sketch of their rip current model is shown in Figure 2.1. The figure shows that the feeder currents are the converging flows which supply the base of the rip current, the rip neck is the narrow region where the rip current is strongest, and the rip head is where the flow diverges and slows offshore of the breaker zone.

Since rip currents serve as a drainage conduit for the water that is brought shoreward and piled up on the beach by breaking waves, the size, number and location of rips are influenced by the ambient wave conditions. McKenzie (1958), citing observations made on sandy Australian beaches, noted that rip currents are generally absent under very low wave conditions except for miniature rip currents caused by the convergence of swash in the hollows of beach cusps. The author further notes that rips are more numerous and somewhat larger under light to moderate swell, and with increasing wave conditions the increased volume of water moving shoreward requires the rips to grow in size and activity. As the rips grow in intensity some rips are eliminated while others migrate in the longshore direction as they strengthen resulting in broad, strong rip currents with large longshore separations under storm conditions. In addition, the magnitude of flow velocities associated with rip currents is directly related to the height of the incident waves (Shepard and Inman, 1950). An increase in wave height will increase the strength of existing rip currents and the response of the rips to wave height variations is relatively instantaneous. These wave height variations will not necessarily modify the form of the rip current system (McKenzie, 1958), however, variations in rip current strength

can significantly affect their erosion power and have consequences for beach profile equilibrium. For example, an equilibrium or accretionary beach profile under light wave conditions might be quickly eroded by an increase in wave height due to the increased erosion power of waves and currents.

2.3 Morphologic effects of rip currents

Shepard *et al.* (1941) noted that on fine sand or silt beaches rip currents can be identified by a dark colored streak of sediment laden water which extends past the breaker zone. After the brown streaks penetrate the breaker zone they tend to spread out and disperse. This suggests that rip currents can have a significant effect on the nearshore morphology. These same authors describe some of the morphologic features associated with rips. They note that rips often are associated with channels in the beach. This indicates that, near to shore, rip current flow velocities extend to the bottom of the water column and can scour out sediment from the beach face. In addition, the authors note that many rip currents are located near indentations in the coastline and they observed rips tending to move outward from the center of indentations when there was no prevailing longshore current. They also noted that rip currents are found on sandy and rocky coasts and can also be found extending seaward from protrusions from the shoreline such as headlands or manmade structures (e.g. piers, jetties). These descriptions of rip currents show that rip currents are of significant geological importance and act as a transport mechanism moving suspended sediment offshore.

Cooke (1970) conducted a study at Redondo Beach, California, that concentrated on the role of rip currents in the nearshore sediment transport system. He noted that, at this site, stationary rip channels were commonly present, and well-defined rip currents were only present during falling or low tides. The prevalence of rip currents during falling tides was also noted by McKenzie (1958) and was attributed to the concentration of the drainage system into the current channels

resulting in stronger current flows. Cooke describes the floor of the rip channels as consisting of coarse mega-rippled sand, which represents the bed load carried by the current, and observed that the ripples did not extend past the breaker line. It is thought that, offshore of the surf zone, rip currents do not extend to the sea floor and only suspended sediment is carried offshore. Cooke attempted to quantify the amount of sediment which is transported in rip currents, but his sampling size was restricted to a handful of measurements per rip current. However, his results suggested that most sediment transport in rips is done during brief periods when velocities are high. In contrast to his finding of wide variability in sedimentation rates, he found the size of sediment grains settling out of rip currents to be remarkably homogeneous with a general trend of coarser grains settling out nearer to shore and finer grains offshore. Thus, rip currents represent an important mechanism for moving fine sediments from the beach face to the inner continental shelf, and for concentrating heavier grains on the shore. He also suggests that elongate bands of coarse sand, oriented normal to a paleoshoreline, would indicate the paleoshoreline to be a high energy environment.

Komar (1971) conducted a study which focused on the role of rip currents and their associated longshore currents in the creation of giant beach cusps. He noted that, while isolated large beach cusps exist, rhythmic series of cusps along a shoreline are more common. Komar cites a study by Dolan (1971) who measured rhythmic beach cusps along the North Carolina shoreline. These cusps had longshore spacings of 150 to 1000 m and cross-shore projections of 15 to 25 m seaward from their embayments. Komar applied the concept of circulation cells, as first described by Shepard and Inman (1951), to the formation of rhythmic beach cusps in order to understand how sediment is transported in these cells. Shepard and Inman described the nearshore circulation system (shown here in Figure 2.2) as being comprised of a slow, broad current brought shoreward through the breaker zone which generates

a system of longshore currents alternating in direction. The longshore currents increase from zero midway between the rips to a maximum where the alternating currents converge and are turned offshore in the base of the rip current.

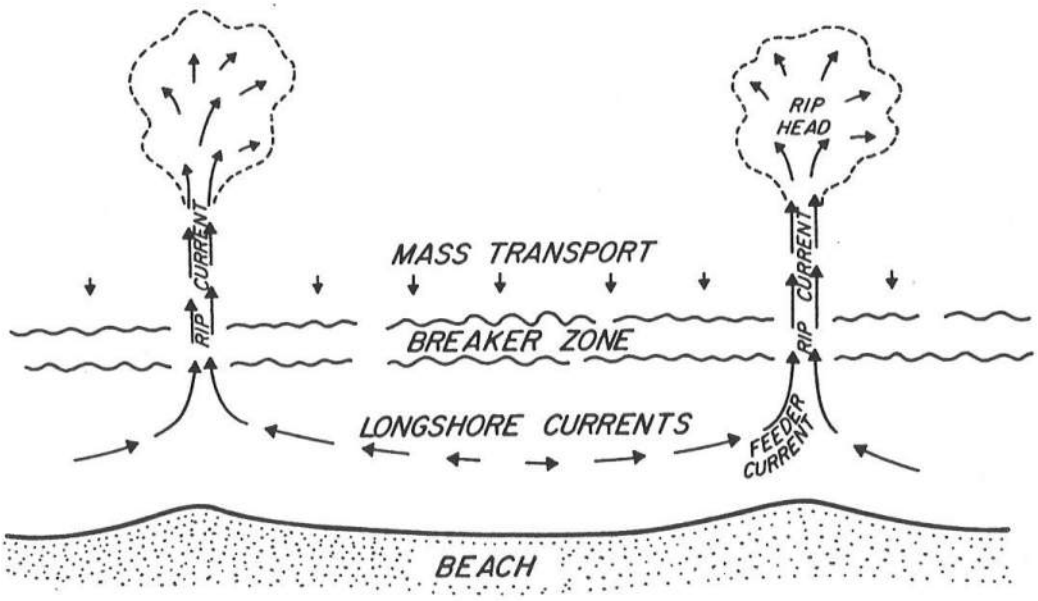

Figure 2.2: Nearshore circulation system, including rip currents, with associated beach configuration (modified from Shepard and Inman, 1951).

Komar hypothesized that, since stronger longshore currents should entrain more sediment, where the longshore currents diverge and velocities are smallest deposition should occur (or at least minimal erosion); while at the base of the rip current, where flows are strongest, the shoreline should be scoured out. Thus he proposed an alternate shoreline configuration for the nearshore circulation cell model shown here in Figure 2.3. He tested his hypothesis by conducting laboratory experiments where rip currents were generated on an initially straight beach by the standing edge wave mechanism (this mechanism is described further in Section 2.4). He found that while initially cusps sometimes developed midway between rip currents (as in Figure 2.3) they disappeared within a few minutes. This was due to

the effect of longshore swash velocities, induced by the incipient cusp, *reinforcing* the small local longshore current of the circulation cell and quickly eroding any deposited sediment. Komar also found that cusps formed, and persisted, in the lee of the rip currents and the beach evolved into the shape described by Shepard and Inman (Figure 2.2). Komar made additional observations in the field at a low energy beach on the coast of Scotland, there he also observed cusps located at the lee of rip currents and noticed that the cusps contained relatively coarser sediments than the remainder of the beach. An additional interesting feature of the laboratory

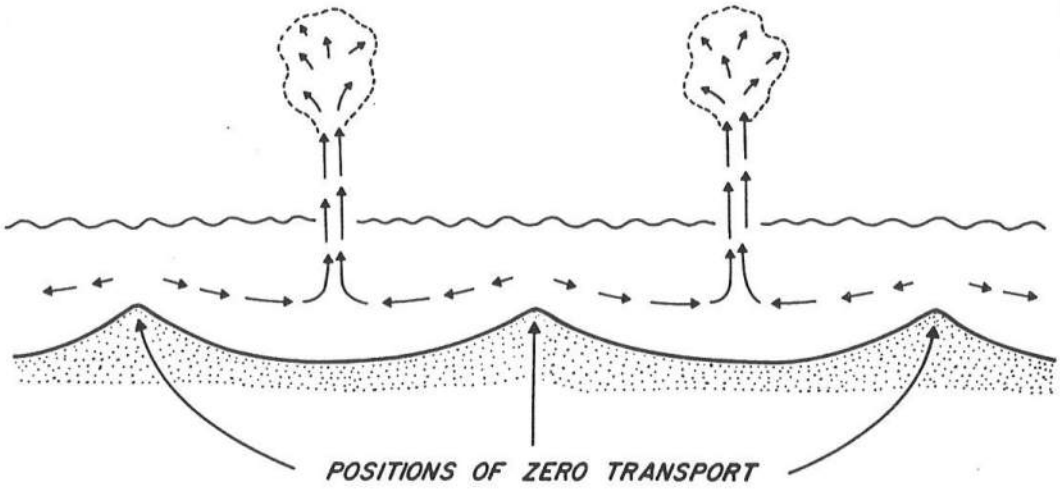

Figure 2.3: Proposed nearshore circulation system and associated beach configuration of Komar (1971).

experiments by Komar was that after a certain amount of time had passed, an equilibrium condition was reached where the rip currents and associated circulation ceased and the cusps remained stable. He postulated that this equilibrium condition was the result of a balance between the longshore wave height variation, which would force the feeder currents towards the cusps, and the swash velocities induced by oblique wave attack on the cusps, which would oppose the feeder currents. He

also suggested that this equilibrium condition would allow for cusps produced by rip currents to exist beyond the lifetime of the individual rips.

The previous mentioned works have indicated that the movement of sediment by rip currents is generally limited to a region near the surf zone. McKenzie (1958) did note that rip currents have been observed extending up to 1500 m from the shoreline, however, outside the surf zone, rip currents were thought to ride over bottom waters and occupy only the upper 3 to 5 m of the water column (Shepard and Inman, 1950; Cooke, 1970). The work of Reimintz *et al.* (1976) suggested that rip currents might influence bottom sediments and bed forms farther from the shore and in deeper water depths than previously thought. Reimintz and his colleagues imaged bed forms off the Pacific Coast of Mexico using side-scan sonar. These images revealed zones of distinct ripples, with wavelengths of 1.25 - 1.5 m, extending seaward perpendicular to the shoreline to depths of 30 m. These ripples occupied channels in the bottom some 0.5 m below the adjacent seafloor. Those authors proposed that rip currents were the cause of these features and noted that the local beach environment was characterized by high energy waves and rip currents were observed extending large distances ($\sim$ 1500 m) offshore. These results suggest that under storm conditions, when most coastal erosion occurs, rip currents can be a primary factor in the movement and distribution of sediments and are a mechanism for moving sediment (even bottom sediments) very long distances out of the nearshore system to the shelf regions.

A comprehensive observational study of rip currents was conducted by Short (1985) on Narrabeen Beach, Australia. Short compiled data on more than 3500 observed rip currents over a period of 19 months. His study led to an empirical classification scheme for rip currents and represents the most complete description of rip current behavior to date. Short classified rips into three types: 1) erosion rips 2) mega rips and 3) accretion rips. He stated that rip spacing is a direct result

of the wave conditions, which are only indirectly related to the tides; rips increase in spacing and intensity as waves rise and conversely as they fall. Therefore the ambient rip currents are determined from the prevailing and the antecedent wave conditions and the direction and rate of change of wave conditions. He states that erosion rips are generated in rising seas on beaches with longshore beach variability. These rips accompany general beach erosion and increase in size and intensity until the beach profile is modified into a fully dissipational state and the rips disappear. He describes erosion rips as usually being highly variable in both time and space and usually persisting for less than a day.

Mega rips are the very large scale ($\sim$ 1 km) erosion rips that are topographically controlled. Mega rips persist when nearshore topography prevents the beach from obtaining a fully dissipative state and instead induces wave refraction which induces persistent longshore wave height gradients that drive rip circulation. Accretion rips usually follow erosion rips and prevail in stable or falling wave conditions. They are relatively stable in space and time and may persist in one location for days or weeks. They are closely spaced and associated with general beach accretion. Finally, Short noted that rip currents are generally absent when the beach profile is fully dissipative. The study by Short presented a general criterion for rip behavior, however, models that incorporate the forces which drive rip currents in a more specific way are required in order to gain a more detailed description of rip current dynamics.

2.4 Models for rip current generation

Shepard *et al.* (1941) described the following three characteristics of rip currents: 1) they are driven by longshore variations in wave height 2) they exhibit periodic fluctuations in time and often have periodic distributions in the longshore direction and 3) they increase in velocity with increasing wave height. In their study

the major source of longshore wave height variations was the convergence and divergence of wave rays induced by offshore canyons. However, there are many possible mechanisms which can induce longshore wave height variations near a shoreline and lead to rip current generation. Dalrymple (1978) divided the existing models for rip current generation into two categories: 1) wave interaction and 2) structural interaction. It is important to note that since any somewhat steady wave height variations will generate rip currents, the question becomes instead, what causes steady wave height variations? Herein, we will divide rip current generation models into the following categories: 1) forced circulations and 2) free circulations.

2.4.1 Forced circulations

The most direct mechanism for driving nearshore currents is the momentum transfer from breaking surface gravity waves to the nearshore flow field. A common example of such a mechanism is the generation of longshore currents from obliquely incident waves (e.g. Longuet-Higgins and Stewart, 1962). Similarly, longshore periodic variations in the incident wave field can force coherent circulation cells. These cells are generally defined as a broad regions of shoreward flow separated by narrow regions of offshore directed flow. If these narrow regions of offshore flow are sufficiently strong they would appear as rip currents.

We define forced circulations as circulations arising from longshore wave height variations imposed by boundary effects (e.g. nonplanar beaches or groin fields) or by a superposition of wave trains. The first models in this category were proposed by Bowen (1969), Bowen and Inman (1970), and independently by Harris (1967). The model of Bowen (1969) imposed longshore bathymetric variations (or alternatively longshore variations in mean water level) which in turn modified the incident wave field. Bowen and Inman (1970) and Harris further supposed that the incident waves could be likewise modified in the presence of synchronous edge

waves. Those authors also demonstrated in a laboratory wave basin that standing edge waves, synchronous with a monochromatic incident wave, will generate stationary rip currents. However, the requirement of synchronous edge waves is somewhat restrictive in the field. Two possible sources of synchronous edge waves are a nearshore reflective structure, such as a headland, or through a nonlinear resonance of the incident wave field. The work of Guza and Davis (1974), however, showed that the synchronous mode was not the most resonant edge wave mode.

Noda (1974) and Mei and Liu (1977) further generalized the wave forcing formulation of Bowen (1970) to include the effects of wave refraction on the incident wave forcing and again found forced circulations induced by periodic bathymetry. Models for rip current generation due to the modification of an initially uniform incident wave train by longshore varying bathymetry have also been proposed by Dalrymple (1978), and Zyserman *et al.* (1990). In addition, laboratory evidence presented by Haller *et al.* (1997) has shown that relatively small longshore bottom variations can generate strong rip currents. Computational efforts by Sancho *et al.* (1995), Haas *et al.* (1998), Sorensen *et al.* (1998), Svendsen and Haas (1999), and Chen *et al.* (1999) have given further evidence of the complexities of such systems.

In addition to interactions with the bottom boundary, interactions between the flow field and the lateral boundaries of the beach often generate rip currents. Rip currents are often observed extending offshore from headlands, especially when waves are obliquely incident. When waves propagate towards a headland, the headland can act to divert the longshore current into an offshore directed rip current. Conversely, when waves propagate away from a headland the headland acts as a shadow zone inducing lower breaker heights on the shore near the headland. The longshore variation of breaker height induces a longshore current towards the region of lowest breakers which again is diverted by the headland into an offshore flow. Experimental evidence demonstrating rip current generation by lateral boundaries has

been given by Dalrymple *et al.* (1977) and Visser (1984) and the effects of bottom friction, convection, and turbulent viscosity in such a system have been investigated by Wind and Vreugdenhil (1986).

Dalrymple (1975) circumvented the requirement of synchronous edge waves or of longshore bottom variability by showing that intersecting monochromatic ocean waves could generate longshore wave height variations and therefore, circulation cells on a longshore uniform coast. The theory was additionally verified in the laboratory. However, the presence of directional or frequency spreading in the incident wave field would tend to smear out the wave height variations and obscure any induced circulation cells. Dalrymple and Lanan (1976) expounded on the idea of Branner (1900), who theorized that intersecting waves form beach cusps, by demonstrating in the laboratory that intersecting waves form rip currents which in turn form beach cusps. Subsequently, Fowler and Dalrymple (1990) extended this model to show that slightly asynchronous waves will produce wave height variations that propagate along the coast, and they conducted laboratory experiments that demonstrated that propagating wave height modulations can generate migrating rip currents. Tang and Dalrymple (1989) presented field data from Torrey Pines Beach, Santa Barbara, California that suggested this mechanism can occur in the field. Most recently, Hammack *et al.* (1991) have demonstrated in the laboratory that rip currents can be generated by short-crested *nonlinear* wave trains.

2.4.2 Unforced circulations

Unforced circulations arise from resonant interactions between the incident waves and the nearshore currents. These circulations manifest themselves as solutions to a representative set of equations that govern the nearshore dynamics. In general, an initial, circulation free state is presumed with a superimposed small perturbation of the dependent variables. The resulting eigenvalue problem is then

solved for the natural states of the system, which may, in fact, have growing instabilities. These unforced circulations derive their energy from the incident waves through a feedback mechanism. In effect, a small perturbation to the current system modifies the incident uniform wave train such that more energy is fed into the circulation system which further modifies the incident waves and so on and so forth.

Arthur (1950, 1962) first speculated that wave-current interaction could affect and even strengthen rip currents through refractive effects. Harris (1967) later noted in his laboratory experiments that waves normally incident to the beach were slowed by the outflowing rips and this caused a curvature of the wave fronts. Early efforts by LeBlond and Tang (1974), Iwata (1976) and Miller and Barcilon (1978) incorporated the effect of rip currents on the local energy and wavelength of the incident waves in an attempt to predict rip current spacing. However, the model of Dalrymple and Lozano (1978) clearly demonstrates that the effect of wave refraction on the currents must be included for steady longshore periodic circulation cells (and rip currents) to be generated. The refraction of the incident waves on the rip current causes the waves to converge towards the base of the rip and induces longshore currents which flow towards the rip as a sustaining mechanism. This model finds the unforced circulation system to be a steady-state solution to the nearshore equations. However, the initial instability which leads to this steady-state is not addressed.

Hino (1974) allowed for a mobile bottom boundary and found steady circulation states along with associated cuspate bottom features. However, his characteristic cell spacing was found to be unreasonably small. A model of similar type was given by Mizuguchi (1976), however, this model required an unjustified bottom friction variability.

2.5 Summary

Rip currents have been capturing the interest of researchers for most of this century. This interest can be attributed to the fact that rip currents are found on

most beaches and have the ability to move large volumes of water and sediment. Also, many find them interesting because they exhibit mysterious behavior; sometimes popping up out of nowhere, other times migrating away and disappearing. They also have an aura of danger about them because of their ability to swiftly carry an unwary swimmer out to sea.

Much of the literature prior to the late 1960's focused on describing rip currents in a qualitative way. Observers noted where rip currents were commonly found and how they behaved and interacted with their surroundings. These observers laid much of the groundwork for future theoreticians and modelers by providing details of the size and structure of rip currents and pointed the direction to possible forcing mechanisms. They also gave insights as to how important rip currents are to the nearshore sediment balance. Finally, they compiled an observational data base which later modelers could use to evaluate the applicability of their theories.

The question of how often the previously described rip current generation mechanisms exist on real beaches is still unknown. The presence of longshore varying bathymetry is certainly quite common on most coastlines and the spatial inhomogeneities of the nearshore circulations on real beaches has long been overlooked but is receiving much recent attention by the modeling community. Also, with the continuing rapid development of the world's coastlines, the number of coastal structures has been multiplying leading to the increased importance of structural effects on the nearshore circulation system.

The researchers of the last 25 years have made great strides in the formulation of nearshore circulation models which can predict many of the features of rip current systems. These models are being used to sort out the many postulated mechanisms of rip current generation and point the way to the most likely sources of rips. Also, some of the recent nearshore models have suggested new mechanisms of rip current generation. However, there are still many unanswered questions. Two

major questions are 1) what is the offshore extent of rip currents and 2) which generation mechanisms are dominant. What is known for sure is that rip currents can have a significant impact on beaches and people. For that reason rip currents will continue to be an active area of research.

Chapter 3

NEARSHORE CIRCULATION EXPERIMENTS: MEAN FLOWS

In this chapter we present results from a set of laboratory experiments investigating the effects of rip currents and longshore varying bathymetry on the nearshore circulation system. Of interest are the influence of the bathymetry on the nearshore wave field, the quantification of currents (longshore currents, rip currents) induced by longshore gradients in mean water levels, and the dominant mechanisms which drive the nearshore circulation on such topographies.

Previous researchers have advanced the theory governing nearshore circulation on longshore varying bathymetries, these include Bowen (1970), Mei and Liu (1977), Dalrymple (1978), Zyserman *et al.* (1990), and Putrevu *et al.* (1995). The combined efforts clearly demonstrate that small longshore pressure gradients, which are commonly neglected in most longshore current models, can drive strong longshore currents. Also, sophisticated computational models (Sancho *et al.* , 1995; Haas *et al.* , 1998; Sorensen *et al.* 1998; Svendsen and Haas, 1999; and Chen *et al.* 1999) have been successfully used to investigate numerically the governing forces and the inherent variability in these systems.

We have sought to obtain a comprehensive data set of nearshore waves and currents from a set of laboratory experiments. It is expected that this data set will be useful in quantifying the nearshore driving forces and therefore verifying previously advanced theories. The data set has already begun to be used in validating

the complex, and computationally intensive numerical circulation models. There are extremely few comprehensive data sets involving rip currents in general. Since, in the field, rip currents tend to be transient, they tend to elude investigators intent on measuring them with stationary instrument deployments, though limited quantitative measurements do exist (Sonu 1972; Sasaki *et al.* 1980; Bowman *et al.* 1988; Huntley *et al.* 1988; Dette *et al.* 1995; Smith and Largier, 1995).

The laboratory, however, is rather conducive to the study of nearshore circulation in the presence of rip currents, since the environment is more easily controlled. However, the extent of laboratory data involving rip currents on longshore varying bathymetry is limited to one brief study by Hamm (1992). Our laboratory study represents the most comprehensive to date on this topic. The results provide a description of the nearshore circulation system under the influence of variable wave conditions. In addition, the results (see Chapter 4) indicate that rip current systems of this type are unstable. These rip current instabilities are a previously unexamined phenomenon.

3.1 Experimental Setup

3.1.1 Physical Model

The laboratory experiments were performed in the Directional Wave Basin located in the Ocean Engineering Laboratory at the University of Delaware. The internal dimensions of the wave basin are approximately 17.2 m long by 18.2 m wide with a three-dimensional "snake" wavemaker at one end. The wavemaker consists of 34 paddles of flap-type. Each paddle is controlled by a separate servo control motor through a complex arrangement of pulleys and cables. Each paddle is 0.51 m wide, 1 m in height, and hinged at its base. The paddles are mounted approximately 11.6 cm from the floor and there is a small vertical gap of approximately 2.5 cm between paddles to allow them to slide freely past each other.

Certain aspects of the wavemaker configuration were sources of noise in the incident wave field. There is approximately 30 cm between the back of the paddles and the basin wall and, since the experiments consisted solely of monochromatic wave fields, standing waves of significant amplitude were often present in the space behind the paddles causing some disturbances to leak out from between the paddles. Additionally, there is a 15 cm gap between the last paddle and the basin sidewall. These problems were combatted somewhat by the use of a swimming pool lane line both immediately in front of and in back of the paddles, and by mounting a wooden barrier in the gap between the paddle and the sidewall. Also, the majority of the measurements were taken in the basin area opposite from the paddle/sidewall gap to help avoid any effects of the gap.

As part of this experimental project, the Center for Applied Coastal Research installed a new concrete beach. The beach consists of a steep (1:5) toe located between 1.5 m and 3 m from the wavemaker with the milder (1:30) sloping section extending from the toe to the opposite wall of the basin. The design and construction of the shore parallel bars was undertaken after the construction of the concrete beach, and was performed by the author with some assistance from Doug Baker (Technician, Civil Engineering Dept.). The bar sections were made in the shape of a generalized bar profile from sheets of High Density Polyethylene (HDP). The interior of the bars contained supports oriented perpendicular to the shoreline. These supports were made from HDP sections 1.27 cm (0.5 in) in thickness spanning 1.2 m in the cross-shore direction with a maximum vertical height of 6 cm at a distance 90 cm from the seaward edge and tapering to sharp corners at both ends. The sharp corner at the bar crest due to the initial triangular shape of the support cross-section was rounded into a parabolic shape "by eye" by the technician. The supports were mounted directly into the concrete beach using small corner irons with stainless steel screws and plastic anchors. The supports were spaced approximately 61 cm

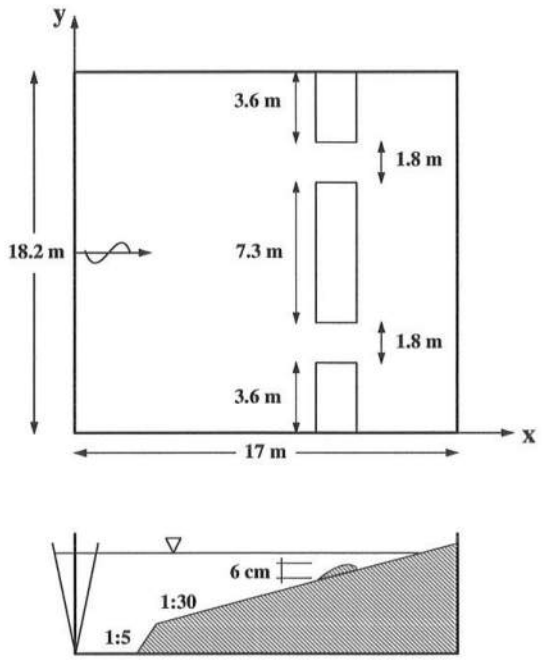

Figure 3.1: Plan view and cross-section of the experimental basin.

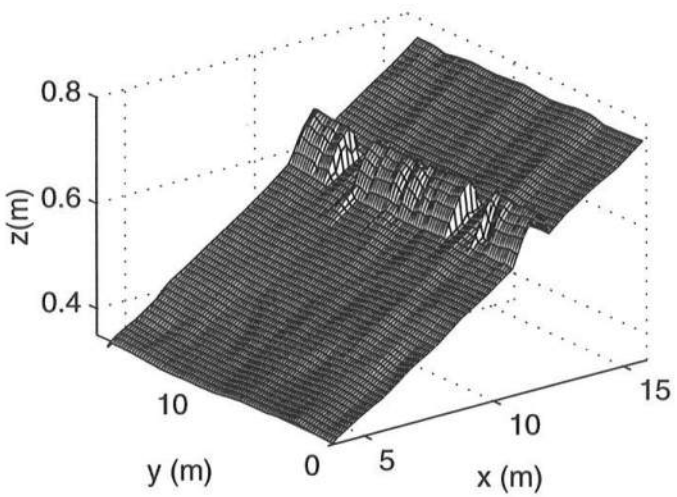

Figure 3.2: 3-D interpolation of the wave basin survey data.

apart in the longshore direction and overlayed with sheets of HDP .318 cm (.125 in) thick so that the bar sections were completely enclosed. The cover sheets were attached directly to the supports with stainless steel screws. After each bar section was completed all exposed joints and the contact between the HDP and the beach were sealed with caulking meant for underwater use.

The completed bar system consisted of three sections: one main section spanning approximately 7.32 m longshore and two sections approximately 3.66 m each. The longest section was centered in the middle of the tank and the two smaller sections placed against the sidewalls. This left two gaps of approximately 1.82 m width located at 1/4 and 3/4 of the basin width that served as rip channels. The steep slopes at the channel sidewalls were reduced by packing cement along the bar edges in order to reduce somewhat wave reflections from the channel sides. A plan view of the wave basin is shown in Figure 3.1 along with the location of the coordinate axes used in this experiment. The seaward edges of the bar sections were located x=11.1 m with the bar crest at x=12 m, and their shoreward edges at x=12.3 m. The wavemaker is located at x=0 m. This configuration caused the ratio of rip current spacing to surf zone width to range between 2.7 and 4.0 during the experiments. In the field this ratio has been found to vary between 1.5 and 8 (Huntley and Short, 1992).

After the longshore bars were installed, a bathymetric survey was performed using a Total Station Theodolite. The survey data were used to establish the exact dimensions of the basin and the coordinate y-axis was placed along the wavemaker. The survey also provided details on the variations from longshore uniformity in the planar beach which had settled somewhat. A map of the bathymetry determined by interpolating the survey data is shown in Figure 3.2. The map shows there are periodic variations in the concrete beach due to the concrete settling between the three support beams running in the x-direction underneath the beach. There are

also smaller scale variations in the longshore bars. Figure 3.3 shows the standard deviation of the depth in the longshore direction as a function of cross-shore position. The effect of the rip channels has been removed from this figure. The data shows that the variations are reasonably small and fairly consistent in the cross-shore direction with a maximum near x=11.3 m.

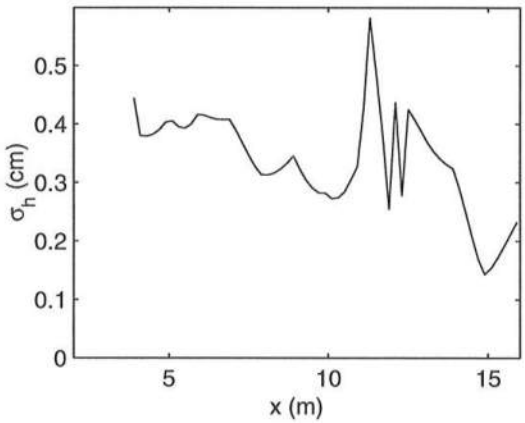

Figure 3.3: Standard deviation of the depth vs. cross-shore distance (from interpolated survey data, effect of rip channels has been filtered out).

3.1.2 Instruments

Ten capacitance wave gauges were used to measure time series of water surface elevation during the experiments. These gauges have nearly linear response of output voltage versus water level at the gauge wire and performed fairly well during the experiments. The wave gauges were calibrated quite often during the experiments. In general, gauges were calibrated every morning and repeatedly during the day whenever the gauges were moved. Nine gauges were mounted on a mobile carriage that spanned the basin in the longshore direction; the tenth gauge was mounted on a separate quadripod which moved around the basin to provide reference measurements.

Three 2-D side-looking Acoustic Doppler Velocimeters (ADV's) were used to obtain time series of horizontal currents. These probes are designed to work in water depths as small as 3 cm and are hardwired to a dedicated PC for data acquisition. This PC was linked, also by cable, to the mainframe that acquired the wave data, so that the onset of data acquisition was synchronized between the ADV's and the wave gauges. The ADV's do not require calibration and a mounting system was designed that allowed them to be mounted either on the beam holding the wave gauges or separate aluminum box beams that could be oriented in both the x and y directions and rigged to the carriage at various locations. Considerable amount of time was spent positioning the ADV's during the experiment. Each time the sensors were moved their position had to be adjusted in three coordinate directions and their orientation was determined "by eye". This was an iterative process that involved repeated adjustments of the sensors, measuring their position, then standing at a distance and visually determining their orientation.

3.1.3 Experimental Procedure

The waves were generated using the Designer Waves theory of Dalrymple (1989) assuming longshore uniformity. The mean beach profile used in the wave generation program was obtained by averaging cross-shore transects (including the bars) from the survey data. All of the tested wave conditions were monochromatic and normally incident except for one (Test F), therefore the full capabilities of the Designer Waves theory were generally not utilized. In all the experiments the theory was used to generate a uniform plane wave with target amplitude at the seaward edge of the bar system. In general, the criterion of a uniform plane wave was fairly well met offshore from the bars. However, certain longshore variations in the wave height offshore of the bars were evident during all tests. Some of these variations were attributed to a longshore modulation in the beach due to concrete settling, especially at the centerline of the tank. Also, smaller scale variations in

the amplitude were present and become pronounced with increasing offshore wave height. These can be attributed to several factors including nonlinear wave effects, noise due to the gaps between paddles, and high frequency basin seiche modes.

For all experimental runs data were sampled at 10 Hz by all sensors and data acquisition was started at or very near the onset of wave generation. During wave generation 16384 data points were sampled by each sensor, except for a few tests of longer duration. A typical experimental run consisted of the following:

1. moving all wave gauges and ADV's to their given locations and making sure they are properly oriented
2. waiting for the basin oscillations to settle down, then calibrating the wave gauges
3. sampling the wave gauges for 102.4 seconds (at 10 Hz) during still water in order to establish a reference zero elevation
4. starting wave generation and data acquisition for all sensors
5. after each run (27.3 minutes, 1638.4 s) wait for the seiching to dissipate then repeat still water reference measurement
6. return to step 1.

3.2 Experimental Results

3.2.1 Wave and current measurements

Initial pilot experiments were performed in order to gain a feel for how the system behaved, the results from those experiments will not be specifically discussed herein. As the experimental work proceeded, the measuring location plan for all the sensors evolved. The first test (Test B) contains the most extensive spatial map of currents. This test, in addition to earlier pilot experiments, showed that the

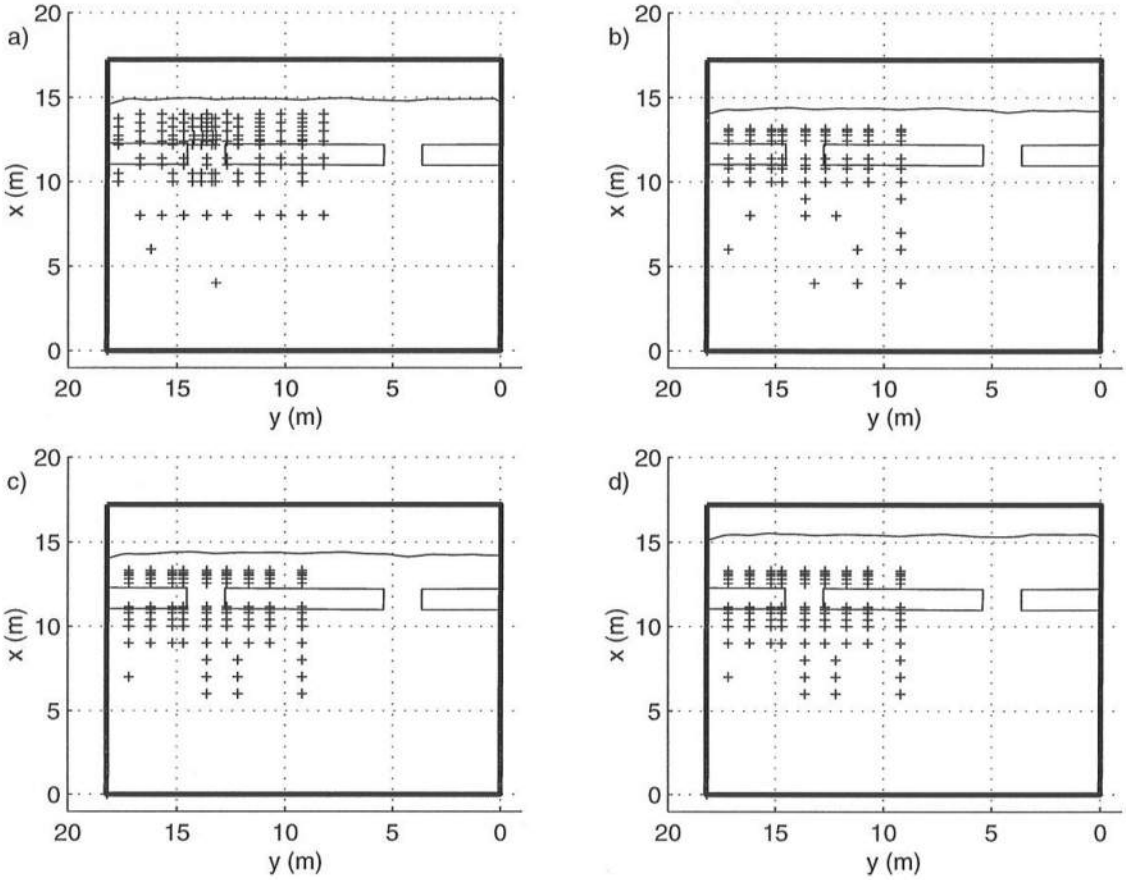

Figure 3.4: Wave gauge sampling locations for (*a*) Test B (*b*) Test C (*c*) Tests D-F (*d*) Test G, the shoreline is shown as the solid line.

circulation fields associated with the two rip currents were reasonably equivalent and therefore we could concentrate our measurements on one half of the basin. The subsequent test (Test C) concentrated on measuring the rip current flow field in detail, and the remaining tests (Tests D-G) obtained basic velocity measurements in the longshore current and in the rip. All tests contain a reasonably extensive map of the wave heights since there were many more wave gauges, whereas the current measurements were always at a premium due to the lack of sensors. The locations of the wave gauges and the ADV's are shown in Figures 3.4-3.5 for all tests. In general the ADV measurements were made 3 cm from the bottom, but certain offshore

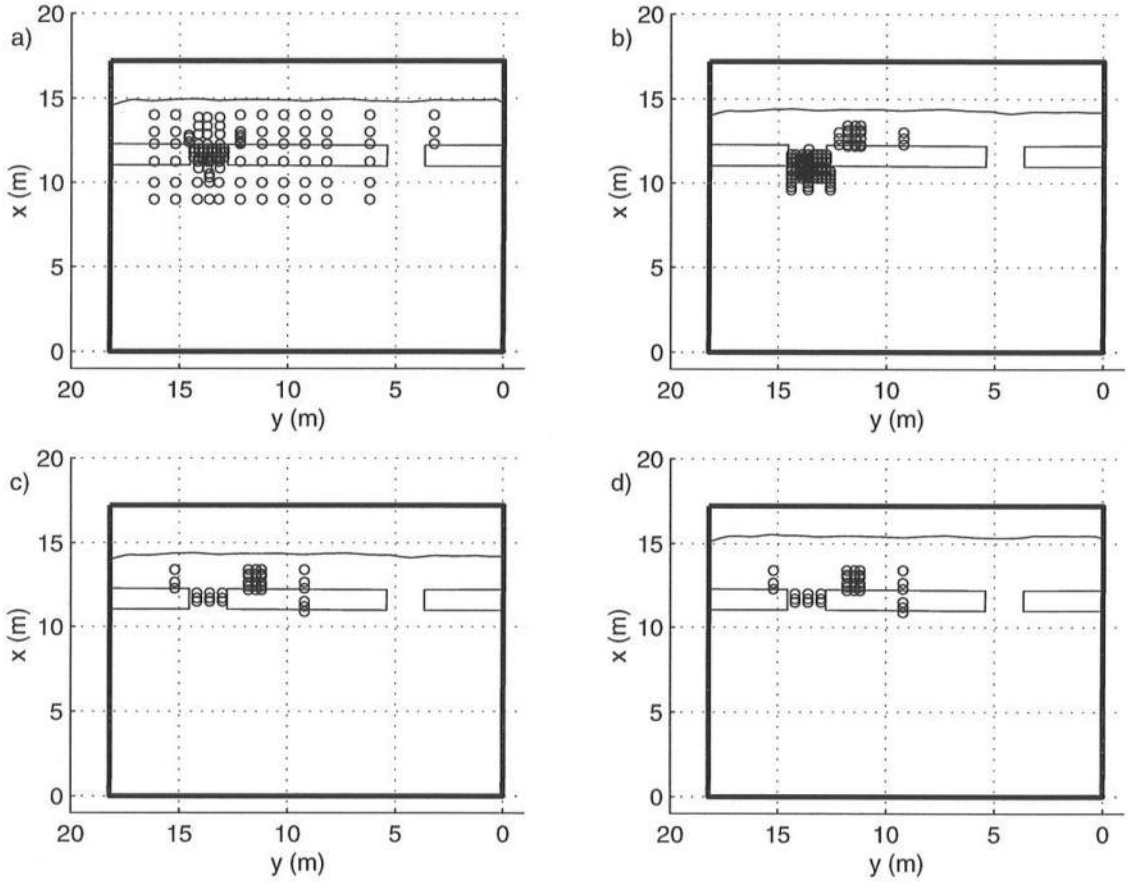

Figure 3.5: Current meter sampling locations for (*a*) Test B (*b*) Test C (*c*) Tests D-F (*d*) Test G, the shoreline is shown as the solid line.

measurements were made at locations higher in the water column. The specific measuring locations for all sensors and the depths of the ADV measurements are listed in Appendix A.

The experimental conditions such as wave height (H), water depth at the bar crest (h_c), shoreline location (x_{swl}), wave period (T), and incident angle (θ) are given in Table 3.1. Most of the tests had normally incident waves with $T = 1$ s and different wave heights and water levels. However, Test E had waves of 0.8 s period and Test F has an incident angle of $\theta = 10$ degrees. It is important to note that for Test F the Designer Wave theory was used to generate a uniform wave train with

Test	H (cm)	T (sec)	$\theta(deg)$	h_c (cm)	x_{swl} (m)
B	4.41	1.0	0	4.73	14.9
C	4.94	1.0	0	2.67	14.3
D	7.56	1.0	0	2.67	14.3
E	3.68	1.0	0	2.67	14.3
F	2.63	0.8	10	2.67	14.3
G	6.79	1.0	0	6.72	15.4

Table 3.1: Table of experimental conditions, mean wave height (H) measured near offshore edge of center bar (x=11 m y= 9.2 m), wave period (T), angle of incidence (θ) at x=11 m, average water depth at the bar crest (h_c), and cross-shore location of the still water line (x_{swl}).

$\theta = 10$ degrees near the seaward edge of the bars (x=11 m).

The energy spectra of the incident waves measured at the seaward edge of the bar near the basin center are shown in Figure 3.6 for all the tests. The spectra are all of very similar shape and demonstrate the presence of energetic higher harmonics due to strong nonlinearity at this location. All energy spectra computed in this study utilized standard Fast Fourier Transform techniques with application of Hanning windows and Bartlett averaging to reduce spectral leakage. The 95% confidence intervals were computed assuming the spectral estimates follow a χ^2 distribution. The intervals are given by

$$\frac{n\,E[\tilde{S}(f)]}{\chi(n, 1-\frac{.05}{2})} > S(f) > \frac{n\,E[\tilde{S}(f)]}{\chi(n, \frac{.05}{2})} \tag{3.1}$$

where n is the number of degrees of freedom (d.o.f.), $S(f)$ is the true spectrum, and $E[\tilde{S}(f)]$ is the estimated spectrum.

For this analysis, the first 1024 points of all wave and velocity data were removed before processing in order to remove wavemaker startup effects. Individual wave heights were determined using a zero-up crossing method and then averaged to determine the mean. Figure 3.7 shows the spatial variation of the measured mean wave heights computed in this manner during each test.

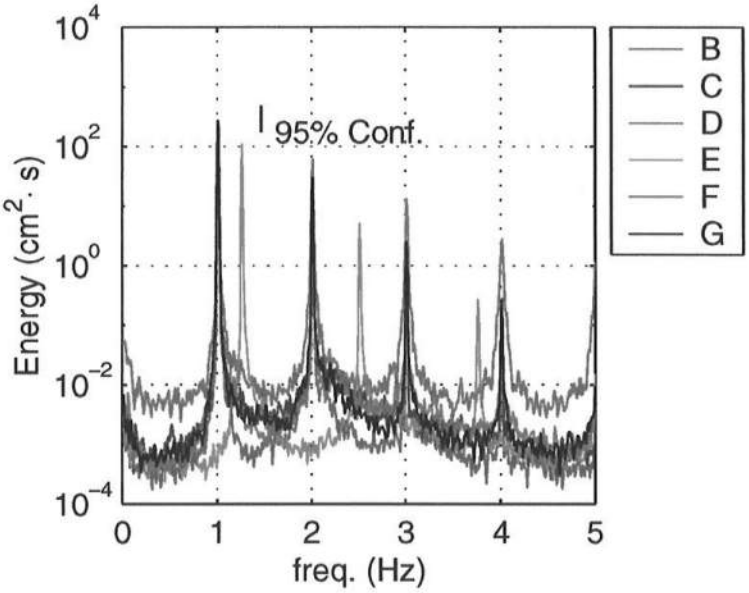

Figure 3.6: Energy spectra of incident waves measured at (x,y)=(11 m, 9.2 m) for Test B (red), Test C (blue), Test D (green), Test E (cyan), Test F (magenta), and Test G (black), Δf=0.01 Hz, d.o.f. =30.

Some common features for all the tests are evident in Figure 3.7. Wave heights offshore of the bar are fairly longshore uniform. As the waves approach the rip channel, they steepen, relative to those near the bars, due to the opposing rip current. The waves broke sharply over the bars for all tests; however a small ridge of wave energy persists through the rip channel (y=12.72-14.54 m) due to the less intense breaking on the rip current. Shoreward of the bars the wave heights were relatively longshore uniform except for near the rip channel.

Figure 3.8 shows the measured spatial variations of mean water level (mwl) during each test. Each test shows a steep increase in the mwl across the bar due to the strong wave breaking. The maximum setup of approximately 1.4 cm was measured near the shoreline during Test D; correspondingly, this test involved the largest wave height to bar crest depth ratio (H/h_c). Shoreward of the bars each test

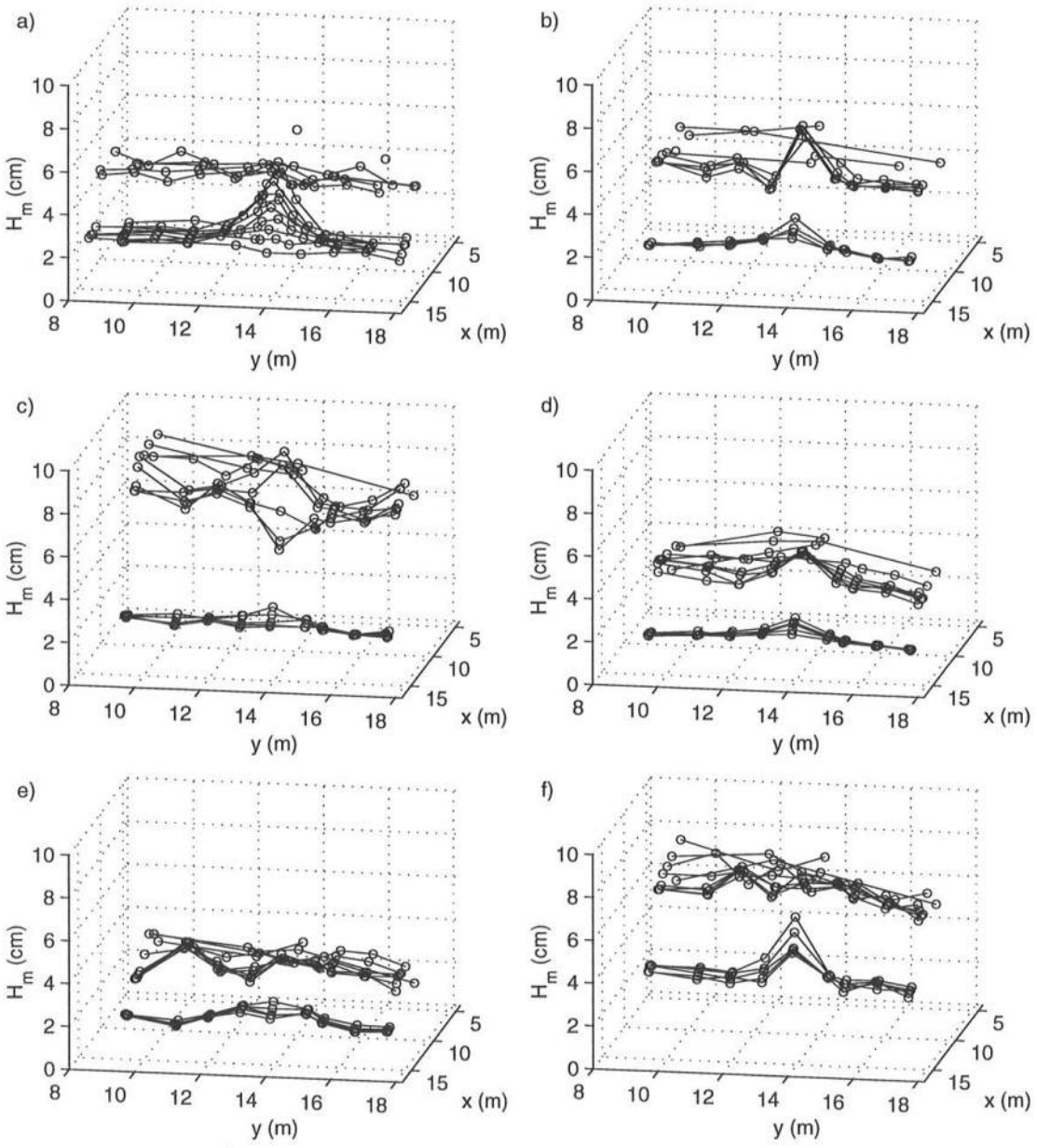

Figure 3.7: Measured mean wave heights for (*a*) Test B (*b*) Test C (*c*) Test D (*d*) Test E (*e*) Test F (*f*) Test G.

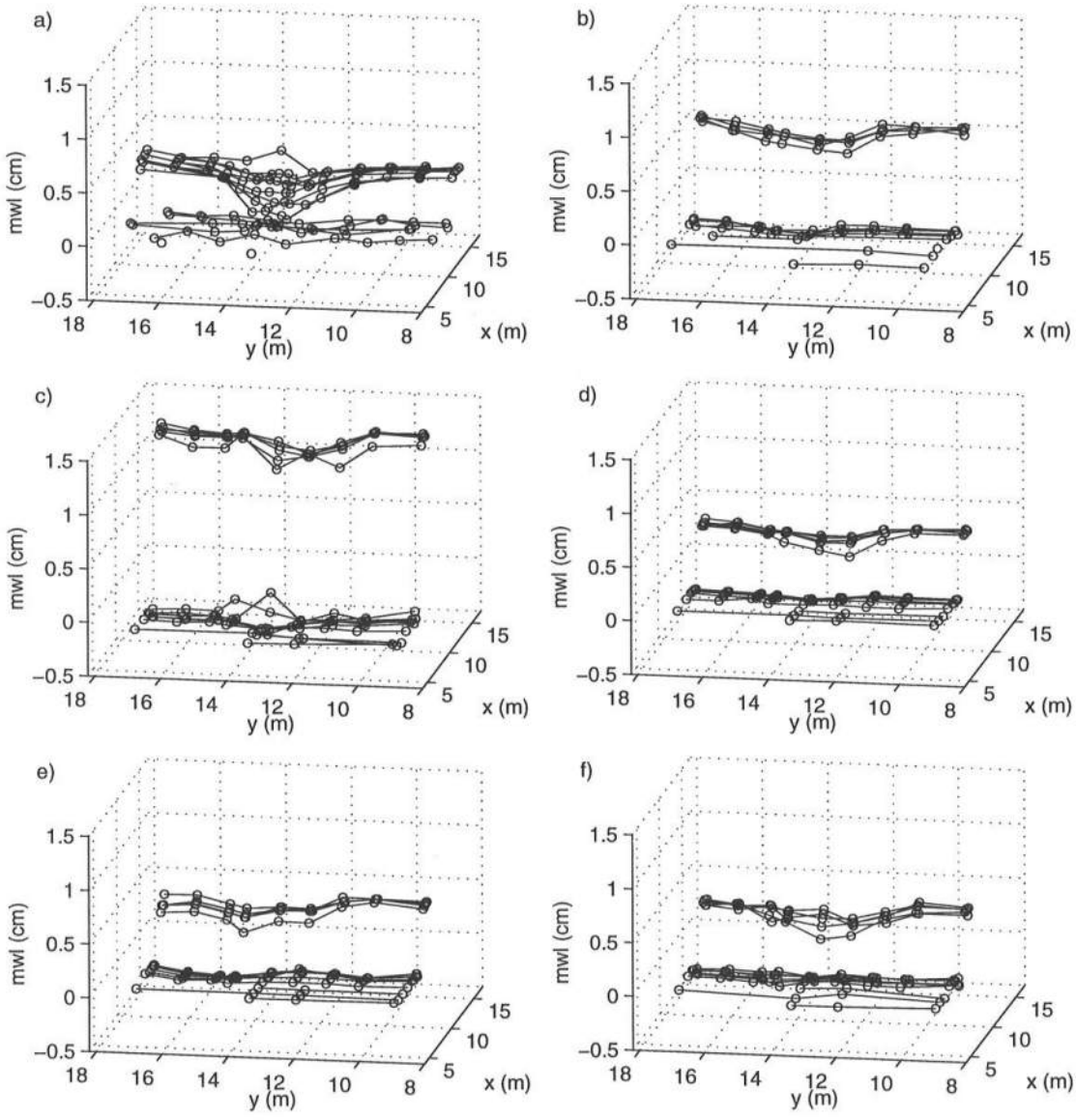

Figure 3.8: Measured mean water levels for (*a*) Test B (*b*) Test C (*c*) Test D (*d*) Test E (*e*) Test F (*f*) Test G.

shows a longshore gradient in mwl sloping downwards towards the rip channel. This hydrostatic pressure gradient drives the feeder currents that supply the offshore-directed rip current in the rip channel.

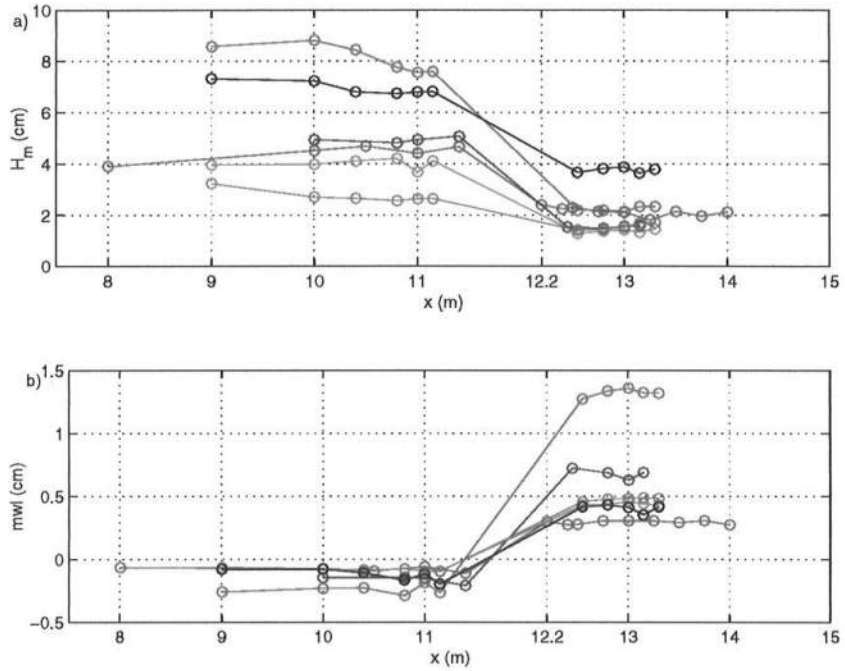

Figure 3.9: Cross-shore profiles of (*a*) mean wave heights and (*b*) mean water levels measured at y=9.2 m, for Test B (red), Test C (blue), Test D (green), Test E (cyan), Test F (magenta), and Test G (black). Colors are defined in Figure 3.6.

Figure 3.9 shows the cross-shore variation of the mean wave heights and mwl as measured near the center of the basin (y=9.2 m) for all the tests. The figure shows little cross-shore variation in mwl offshore of the bar for all tests. Test D shows the largest offshore setdown due to its large wave heights and lower still water level, which cause higher surf zone setup. The cross-shore location of maximum setdown corresponds approximately to the onset of wave breaking at the shoreward edge of the bar, however, it appears wave breaking began slightly further seaward during Test D due to the very large wave heights. The figure also shows an approximate correlation between the decay in wave height across the bar and the increase in mwl

across the bar, as the highly energetic wave breaking in Tests C and D leads to the steepest cross-shore gradients in mwl. Also, there is very little evidence of shoaling shoreward of the bar and the cross-shore gradient of mean water level appears very small in this region.

Figure 3.10 compares cross-shore profiles of mean wave height and mwl measured near the center of the basin (y=9.2 m) and through the center of the rip channel (y=13.6 m). These profiles illustrate the longshore gradients in mean wave height, which are forced for the most part by the longshore bathymetric variations, and which in turn force the longshore gradients in mwl. The data show that the largest longshore gradients in mwl are found shoreward of the bars at approximately x=12.5 m. It is also interesting to note the variation between tests of the wave height profiles measured through the channel. The rate of wave height decay in the channel gives some indication as to the strength of the rip current. Also, the data from Test B indicate that, very near the shoreline, the mwl gradient is reversed such that the center of the basin is down slope. This is due to relatively more wave dissipation shoreward of the channel than shoreward of the bar. This reversal of the longshore gradient is only evident in Test B data since only during Test B were the wave gauges located extremely close to the shoreline. However, it is likely that this gradient reversal occurred in most if not all the experiments.

The mean velocities were computed by averaging the last ($102.4<t\leq1638.4$ s) 15361 points of each time series. The measured mean circulation patterns are shown in Figure 3.11. The measurements in Test B span the largest area of the basin and comparisons with Figure 3.8 suggest that the mean flows are driven very strongly by the water surface gradients. In addition, the current vectors (Test B) indicate that the dominant feature of the nearshore circulation is the strong offshore directed jet in the rip channel and that two separate circulation systems exist. The first is the classical rip current circulation that encompasses the longshore feeder

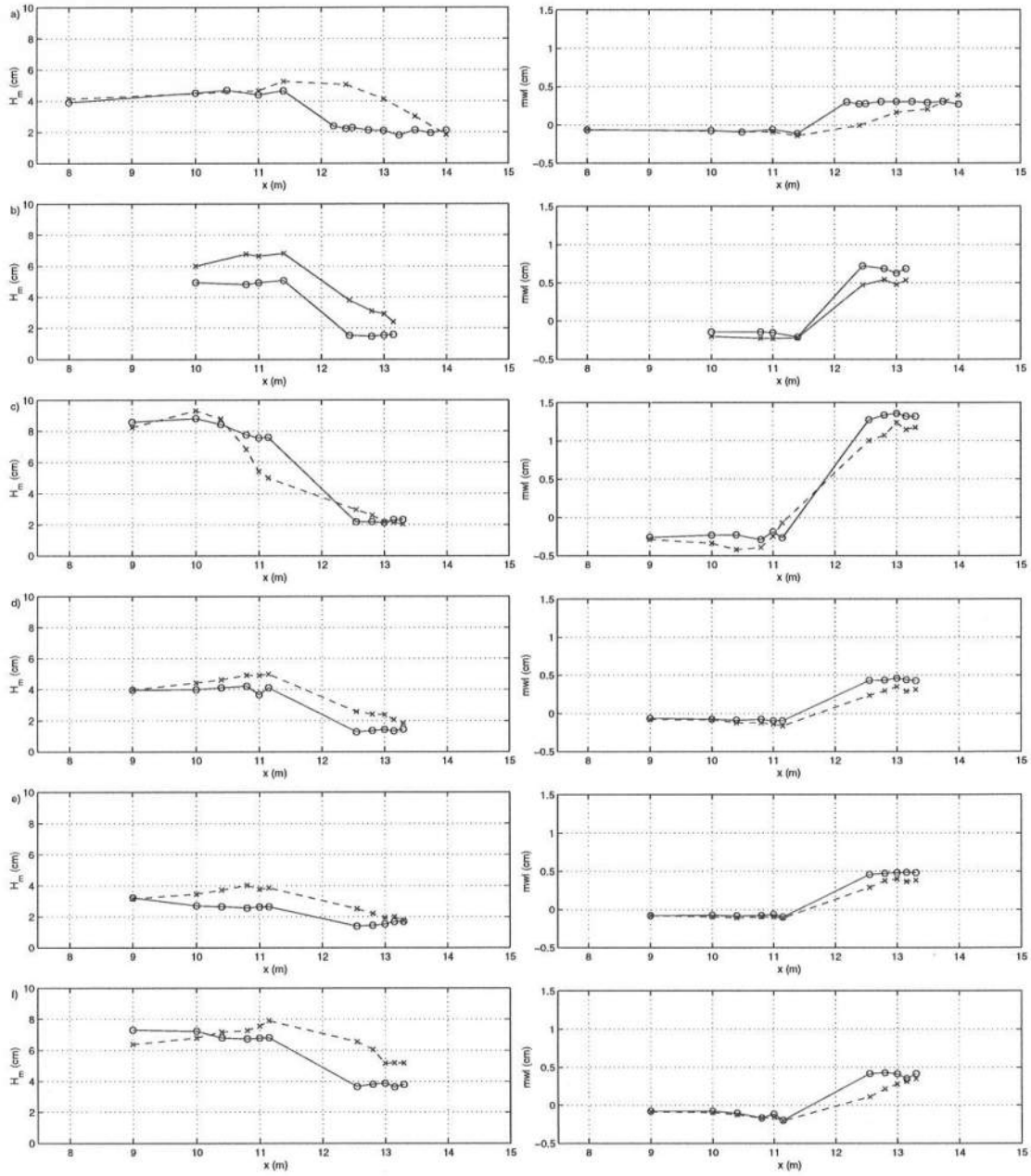

Figure 3.10: Cross-shore profiles of mean wave heights (left) and mean water levels (right) measured at basin center (y=9.2 m) (o: solid line) and at channel centerline (y=13.6 m) (x: dashed line), for (*a*) Test B, (*b*) Test C, (*c*) Test D, (*d*) Test E, (*e*) Test F, and (*f*) Test G.

currents at the base of the rip, the narrow rip neck where the currents are strongest, and the rip head where the current spreads out and diminishes. Offshore of the rip head the flow diverges and returns shoreward over the bars.

The second system encompasses the reverse flows just shoreward of the base of the rips. Here, the waves which have shoaled through the rip channels break again at the shoreline driving flows *away* from the rip channels, which is opposite from the primary circulation, and then the flows are entrained in the feeder currents and returned towards the rips. It is also interesting to note the strong asymmetry in the rip current during Test F. This is obviously directly related to the non-zero incident wave angle. In addition, during Test F there remains a small feeder current on the wall side of the rip. The presence of this feeder current strongly suggests that during this test the longshore pressure gradient, due to the depression in the water surface at the rip, is strong enough to overcome the traditional longshore radiation stress forcing that tries to drive the longshore flow towards the wall.

Figure 3.12 shows the cross-shore profile of the longshore feeder current measured at three locations (y=9.2,11.2,11.8 m) for all tests. The figure shows that near the center of the basin (y=9.2 m, red) there is very little longshore flow shoreward of the bar except for Test F. Profiles measured closer to the rip channel demonstrate that the longshore current is accelerating as it flows towards the rip. Also, the peak of the longshore current is at approximately x=13-13.15 m for all the tests. It is interesting to note that the peak of the longshore current is significantly shoreward of the location of maximum longshore water surface gradient. The data from Test F indicate that there is strong longshore flow even near the center of the basin due to the nonzero angle of incidence. In addition, the magnitude of the longshore current near the bar crest appears stronger during this test. This suggests that the radiation stress forcing of the longshore current occurs at a separate cross-shore location from the pressure gradient forcing.

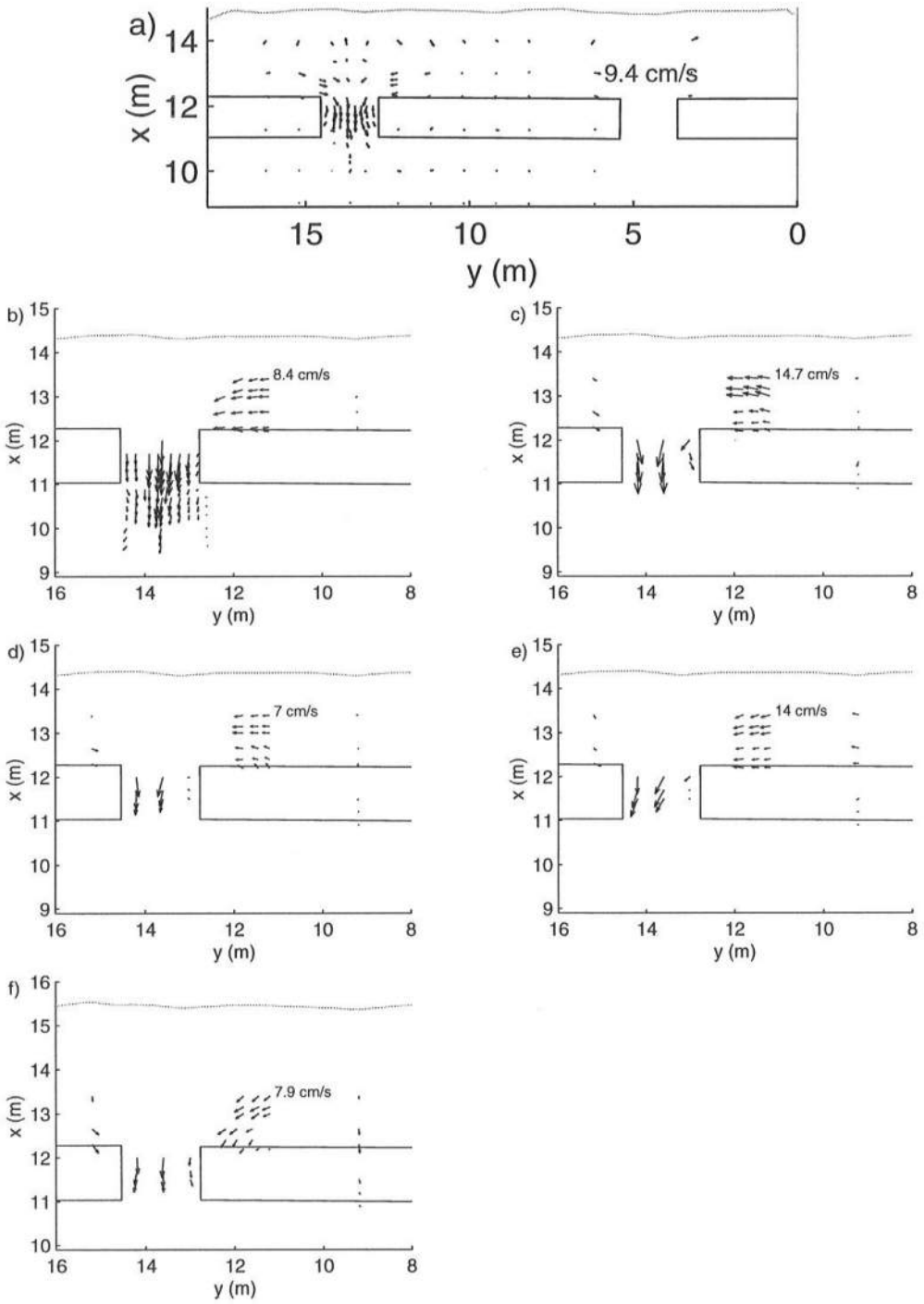

Figure 3.11: Measured mean current velocities for (*a*) Test B (*b*) Test C (*c*) Test D (*d*) Test E (*e*) Test F (*f*) Test G (solid line signifies still water shoreline).

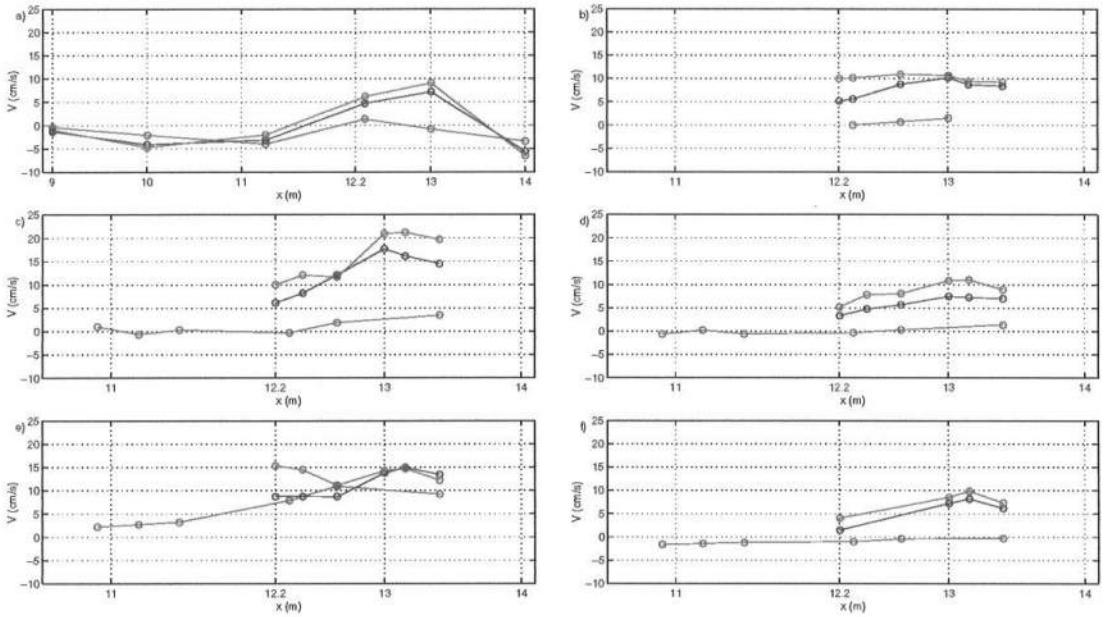

Figure 3.12: Measured mean longshore current velocities measured at y=9.2 m - red, y=11.2 m - blue, y=11.8 m - green, for (*a*) Test B (*b*) Test C (*c*) Test D (*d*) Test E (*e*) Test F (*f*) Test G. Colors are defined in Figure 3.6.

Figures 3.13-3.14 show the mean velocity profiles of the offshore directed rip currents for each test. Some of the cross-shore velocity profiles show significant asymmetry about the channel centerline (y=13.65 m). The asymmetry is most likely related to the momentum flux in the feeder currents. Any asymmetry of momentum flux in the oppositely directed feeder currents that supply the rip will likely cause the rip to shift to one side of the channel. This certainly explains the asymmetry in Test F, during which the waves were obliquely incident. In addition, the presence of the basin sidewalls tended to decrease the waveheight near the walls, therefore decreasing the momentum flux in the feeder currents driven away from the walls.

It is also interesting to note the cross-shore location of the maximum rip velocities and the variation of the velocities down the channel. The data show that, for Tests C and D, the maximum velocity is further seaward in the channel (x=11.7 m and 11.5 m, respectively), while for Tests B, E, and G the maximum is at x=12

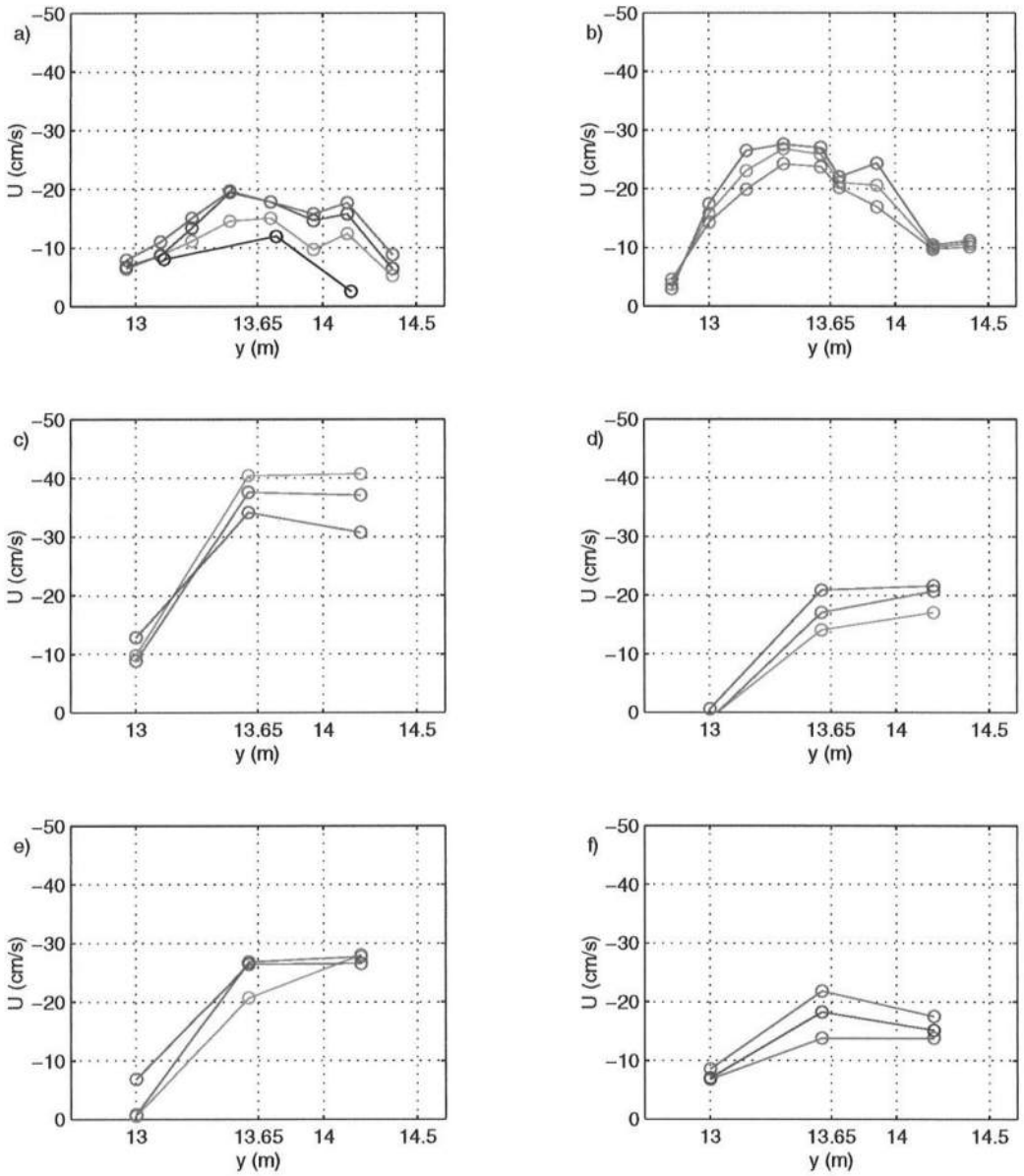

Figure 3.13: Mean cross-shore velocities measured in the rip channel: x=12 m (red), x=11.8 m (blue), x=11.7 m (green), x=11.5 m (cyan), x=11.3 m (magenta), x=11.25 m (black) for (*a*) Test B (*b*) Test C (*c*) Test D (*d*) Test E (*e*) Test F (*f*) Test G. Colors are defined in Figure 3.6.

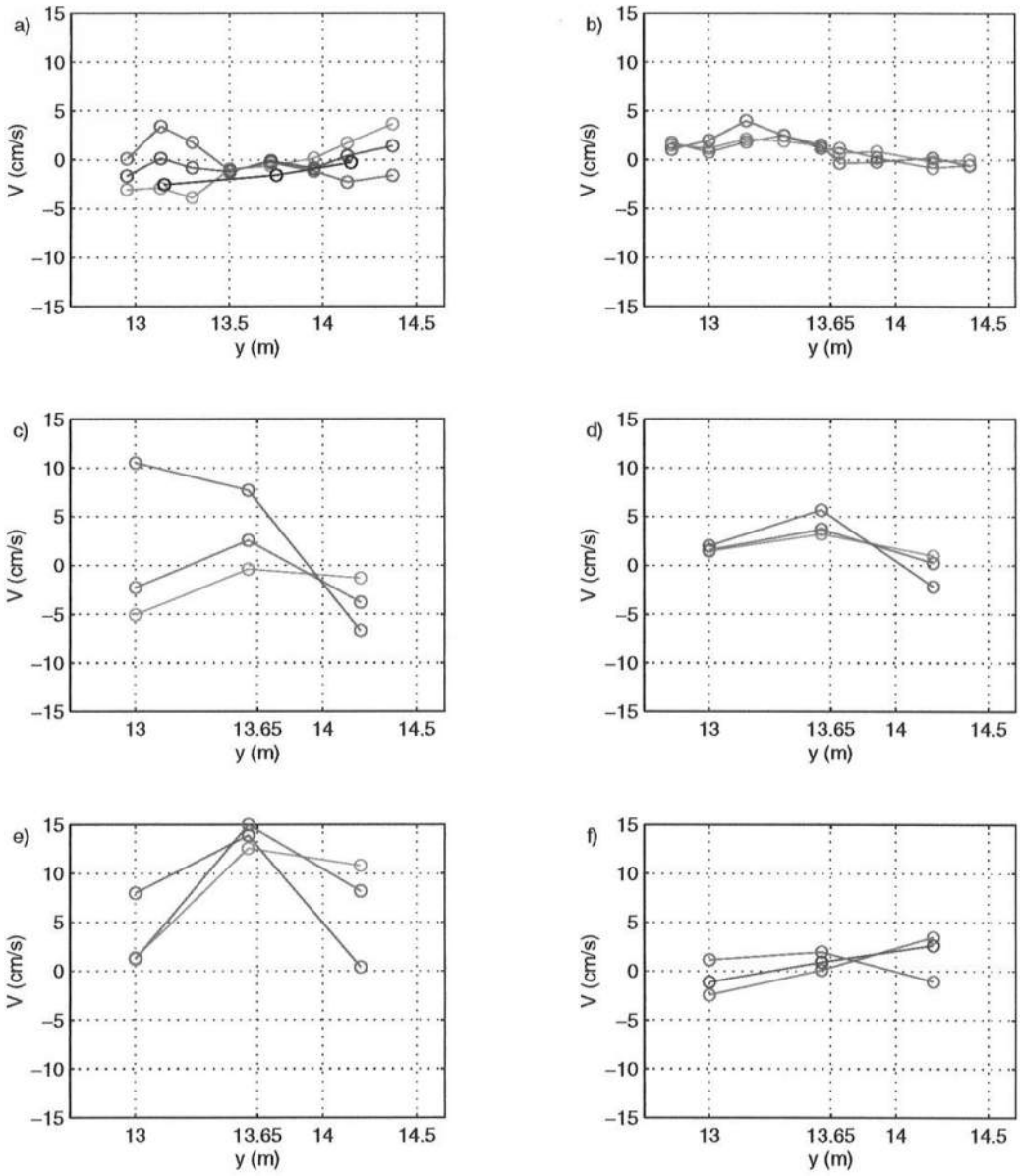

Figure 3.14: Mean longshore velocities measured in the rip channel: x=12 m (red), x=11.8 m (blue), x=11.7 m (green), x=11.5 m (cyan), x=11.3 m (magenta), x=11.25 m (black) for (*a*) Test B (*b*) Test C (*c*) Test D (*d*) Test E (*e*) Test F (*f*) Test G. Colors are defined in Figure 3.6.

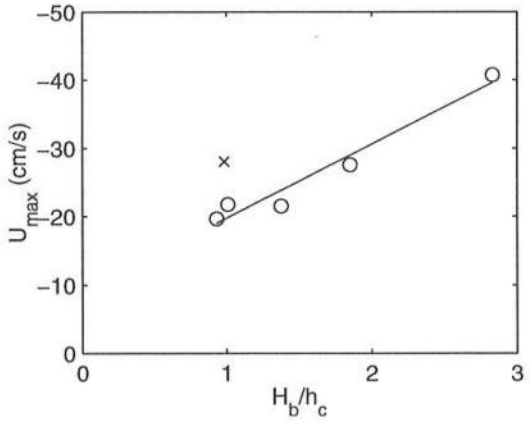

Figure 3.15: Maximum measured mean rip velocity vs. wave height over water depth ratio. H_b is mean wave height measured near the center bar (x=11 m, y=9.2 m), h_c is the average water depth at the bar crest. Test F is indicated by the x.

m. The location of the maximum velocity shows some correspondence with the magnitude of the current, as Tests C and D show the largest rip velocities. Test F also shows slight increase in velocity in the seaward direction, but it is difficult to draw conclusions about this test considering the nonzero angle of incidence.

Figure 3.15 shows the maximum mean rip velocity, measured anywhere in the rip channel, plotted against a wave height to water depth ratio. The wave height to water depth ratio is computed using the mean wave height measured at the shoreward edge of the bar near the basin center (x=11 m, y=9.2 m) and the average water depth at the bar crest. The figure indicates an approximately linear relationship between rip current strength and the wave height to water depth ratio at the bar crest (where the waves break) for normally incident waves. The data point from Test F was not included in the linear fit to the data; however, it seems intuitively correct that for Test F the rip current would be stronger than predicted by the linear fit due to the increased forcing of the longshore current by oblique wave incidence.

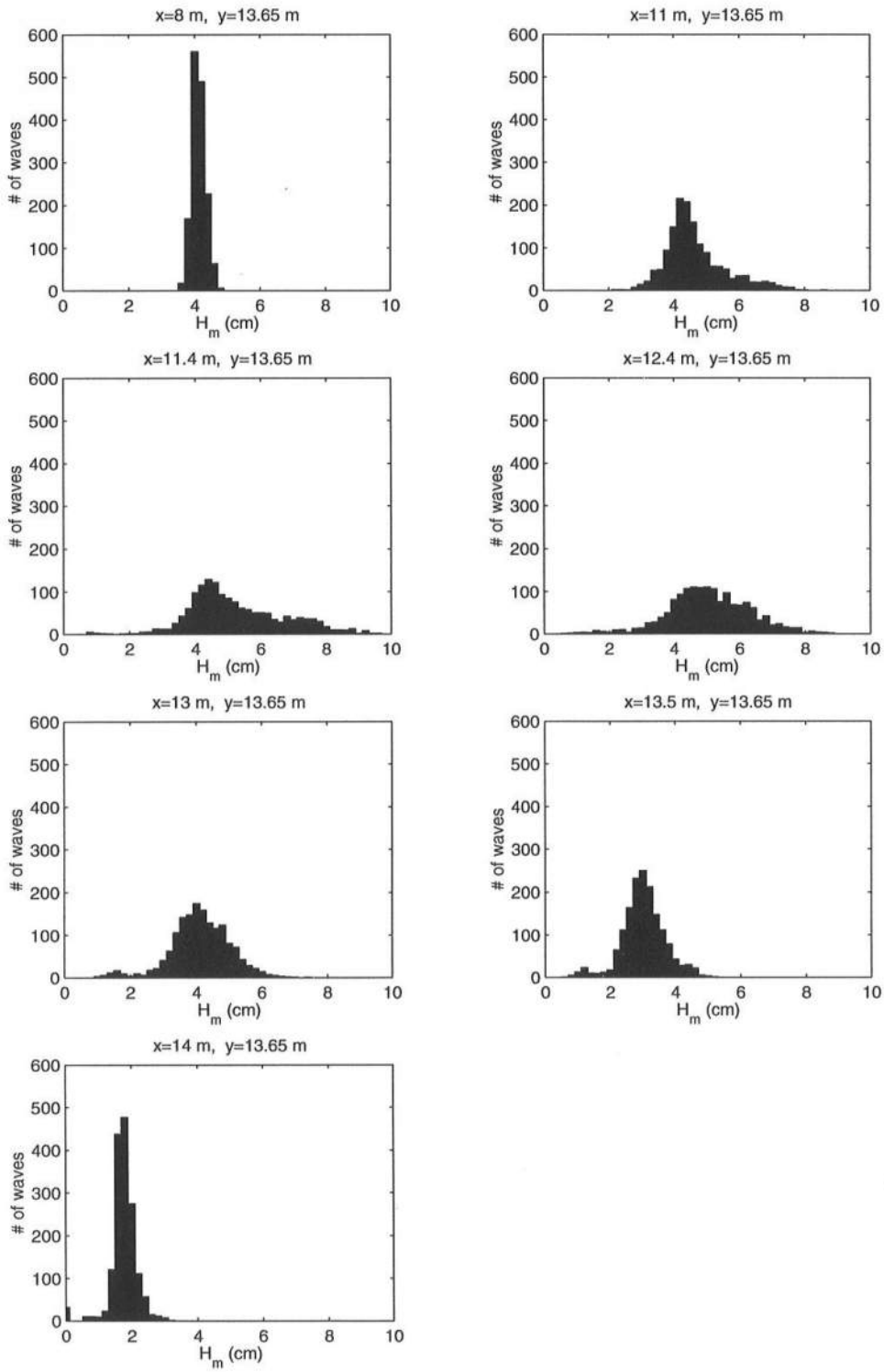

Figure 3.16: Wave height distributions during Test B (bin width 0.1 cm).

Figure 3.16 shows the influence of the strong opposing rip current on the wave height distributions along a cross-shore line extending seaward of the rip channel. It is evident that offshore of the channel (x=8 m, y=13.65 m) the waves are little influenced by the current and the wave height distribution is very narrow. As the waves near the channel they have a wider distribution and are somewhat skewed towards higher wave heights, relative to the incident wave. At x=13.5 m the figure indicates that the waves have started breaking, since their distribution is centered near a smaller wave height (H=3 cm). Finally, as the waves approach the shore, they have passed the influence of the opposing rip and as the highest waves break and dissipate the distribution narrows again.

3.2.2 Repeatability of Measurements

In order to generate a map of this circulation system with dense spatial resolution, the tests had to be repeated numerous times for a given set of experimental conditions. Therefore, it is important to determine how repeatable the experimental conditions were and how much variability existed among a given set of testing runs. Tests B and C consisted of 40 and 34 runs each, respectively, and during these tests certain wave measuring locations were repeated numerous times. The offshore gauge remained stationary for much of Test B and represents the best estimate of experimental repeatability. The longshore instrument carriage was also left stationary from time to time which allows for additional estimates of repeatability. Table 3.2 lists the repeated measurements made by the offshore gauge during Tests B and C. Included are the measurement location, mean wave height (H_m) for each run at that location, and the standard deviation of mean wave height (σ_H) and the mean water level (σ_η). An estimate of the wave height variability is given as σ_H/H_m. The data show that the variability in wave height measured at the offshore gauge was quite small during these tests, remaining less than 5 percent for all cases and approximately 1 percent for most cases. The variability in the mwl measured at the

n	Test	x(m)	y(m)	H_m(cm)	σ_H(cm)	% var.	σ_η(cm)
30	B	4	13.2	4.75	0.06	1	0.02
10	B	6	16.2	4.11	0.05	1	0.01
5	C	4	13.2	4.82	0.05	1	0.02
5	C	7	9.2	4.32	0.04	1	0.01
4	C	4	9.2	4.17	0.02	<1	<0.01
3	C	6	9.2	5.13	0.06	1	0.01
3	C	6	11.2	5.08	0.01	<1	0.02
3	C	4	11.2	4.33	0.14	3	<0.01
2	C	9	9.2	4.76	0.02	<1	<0.01
2	C	9	4.57	4.63	0.14	3	0.01
2	C	8	4.57	4.55	0.06	1	<0.01

Table 3.2: Repeatability of measurements made at the offshore wave gauge. Listed are number of realizations n, associated test, measurement location (x,y), mean wave height (H_m), standard deviation of mean wave height σ_H, percent variability (% var=$100 \cdot \sigma_H/H_m$), and standard deviation of mwl (σ_η). Colors are defined in Figure 3.6.

offshore gauge was also very small and the σ_η was always less than 0.3 mm at the offshore gauge.

Figure 3.17 shows the variability of wave measurements made using the longshore instrument array. These measurements were made closer to the bars and therefore can be strongly influenced by the variability of the circulation system. The increase in variability at these measuring locations is most likely a direct result of the inherent variability of the circulation near the longshore bars which will be discussed further in the next chapter. However, the variability in the wave measurements is still reasonably small at these measuring locations. The variability in the measured mean water levels is also very small (<0.5 mm) except for the measuring line at x=10 m. The larger variability at this location was limited to two runs (C12,C13), and was probably due to human error.

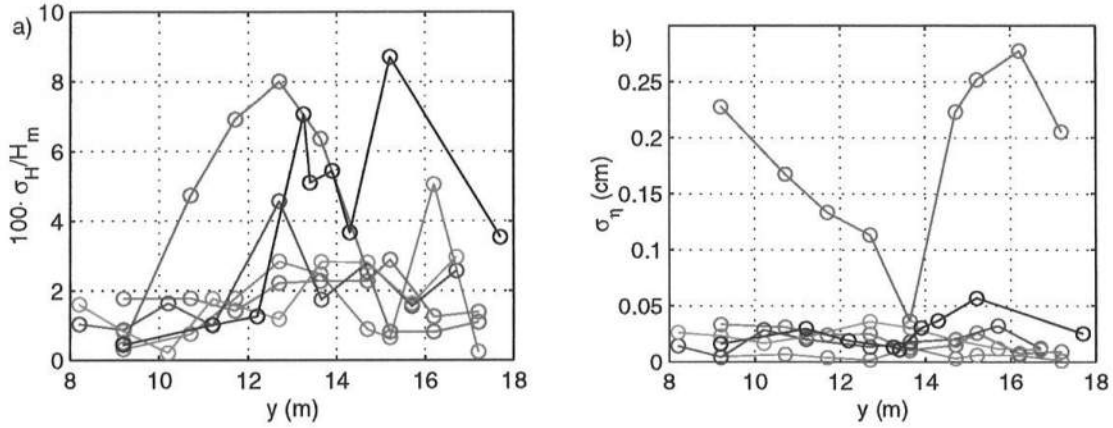

Figure 3.17: Repeatability of (*a*) mean wave heights and (*b*) mwl measured at the longshore instrument array. Measuring locations and experiments shown are x=10 m, n=3, Test C (red); x=11 m, n=5, Test B (blue); x=11 m, n=4, Test C (green); x=11.4 m, n=3, Test B (cyan); x=11.4, n=2, Test C (magenta); x=12.2 m, n=3, Test B (black).

Other sources of experimental error include spatial errors due to inexact positioning of the sensors, these errors are estimated to be less than 1 cm. Most importantly, the sensors were positioned according to the coordinate system established in the physical basin. This coordinate system is different from the survey coordinates used herein and this has introduced further spatial errors in sensor postions. These errors are estimated to be less than ±10 cm, but may be corrected using the survey information. Also, the position of the ADV's relative to the bottom is estimated to be accurate within 0.5 cm. Finally, the measuring device that determined the still water depth was calibrated using the survey data and is estimated to be accurate to ±2-3 mm.

3.3 Summary

This chapter describes a series of wave basin experiments to investigate the effects of periodically spaced rip channels on the mean nearshore circulation. The

physical model is described and the experimental procedure is listed in detail. The experiments evaluated the nearshore circulation under six different incident wave conditions. The spatial variations of mean quantities, such as wave height, water surface elevation, cross- and longshore currents, are described. The mean current patterns indicate the circulation consists of primary and secondary circulation systems, each containing a pair of counter-rotating cells. The primary system consists of the longshore feeder currents and the rip current. The secondary system is located shoreward of the primary and is driven by wave breaking shoreward of the rip that drives flows away from the rip channel. The experiments also suggest that the mean circulation is strongly driven by pressure gradients due to variable mean water surface elevations.

Analysis of the cross-shore profile of the longshore current shows a peak in the profile shoreward of the bar crest in what may be considered the bar trough. This peak is significantly shoreward of the location of maximum longshore water surface gradient in the trough. Analysis of the mean offshore flows in the rip channel shows that the magnitude of the rip current can be as large as 40 cm/s, which is quite large for laboratory scale. The maximum offshore component of the rip current is shown to be linearly related to the wave height to water depth ratio at the bar crest for the cases shown.

Finally, an analysis of experimental repeatability is performed. Variability of mean wave measurements (H_m, mwl) from run to run is shown to be very small at the offshore gauge. There is increased variability for wave measurements made closer to the nearshore bar system. However, the increased variability is still reasonably small and is likely associated with the inherent variability of the nearshore circulation.

Chapter 4

NEARSHORE CIRCULATION EXPERIMENTS: UNSTEADY MOTIONS

The previous chapter described and quantified the mean circulation patterns in the experimental bar/channel system; however, an additional and important aspect of this system is the unsteady nature of the rip currents. Simultaneous visual observations and video recording of the rip current were made during the experiments with the aid of dye injected into the feeder currents. It was also possible to track the location of the rip by watching the distinct breaking pattern (whitecapping) of the incident waves that was limited to a narrow region of strong flow in the rip neck. Though a strong rip current was present in the rip channel throughout most of each experimental run, during many of the tests the entire rip current slowly migrated back and forth in the channel. This rip migration was easily tracked by watching the narrow region of breaking waves move back and forth in the channel. At times the rip would migrate quite quickly, and could migrate out of the channel onto the bars or even temporarily bifurcate into two separate currents. The spatial extent of the rip migration seemed to be correlated with the still water level in the basin. At high still water levels, the rip was less constrained in the channel and there tended to be more offshore flows over the bars.

An analysis of velocity time series measured near the rip channel demonstrated that the rip was unsteady at multiple time scales during certain tests. In

this chapter we will present evidence indicating the presence of low frequency motions during the experiments; we will determine the specific time scales associated with the unsteady motions; and we will specify their spatial distribution in the circulation system. We will also discuss possible sources for these motions and discuss which of these possible sources is more likely.

4.1 Test B

Figures 4.1-4.5 show the complete cross-shore and longshore velocity records measured during runs B33-B36 and B13 (see Appendix A for a complete list of experimental runs). These measurements, except for B13, were made along cross-shore lines near the center of the rip channel. Figure 4.6 shows the mean current vectors for these same sensors, and their relation to the bar/channel system. Although the mean longshore component is very small for these records, the individual records show large amplitude oscillations at relatively long time scales. These oscillations, however, are not strongly evident in the cross-shore records. The record from run B33, shown in Figure 4.5, is a much longer record (2733 s) than the other runs. This record indicates that these low frequency oscillations were present throughout the experiment at this location and it also suggests that the oscillations increase in frequency slightly after t=1200 s.

Since these unsteady motions have such long periods, the longer records from B33 were most suitable for spectral analysis. Figure 4.7 shows the averaged energy spectrum of the longshore velocities measured during this run. The spectrum shows a significant peak near 0.005 Hz that is more energetic than the longshore incident wave signal (1 Hz) at this location by at least an order of magnitude. It should be noted that this approximately 200 s time scale is unusually large for laboratory scale systems.

Figure 4.8 provides insight into the dynamics of these very low frequency oscillations. Shown as colored lines are lowpass (f <0.01 Hz) filtered longshore

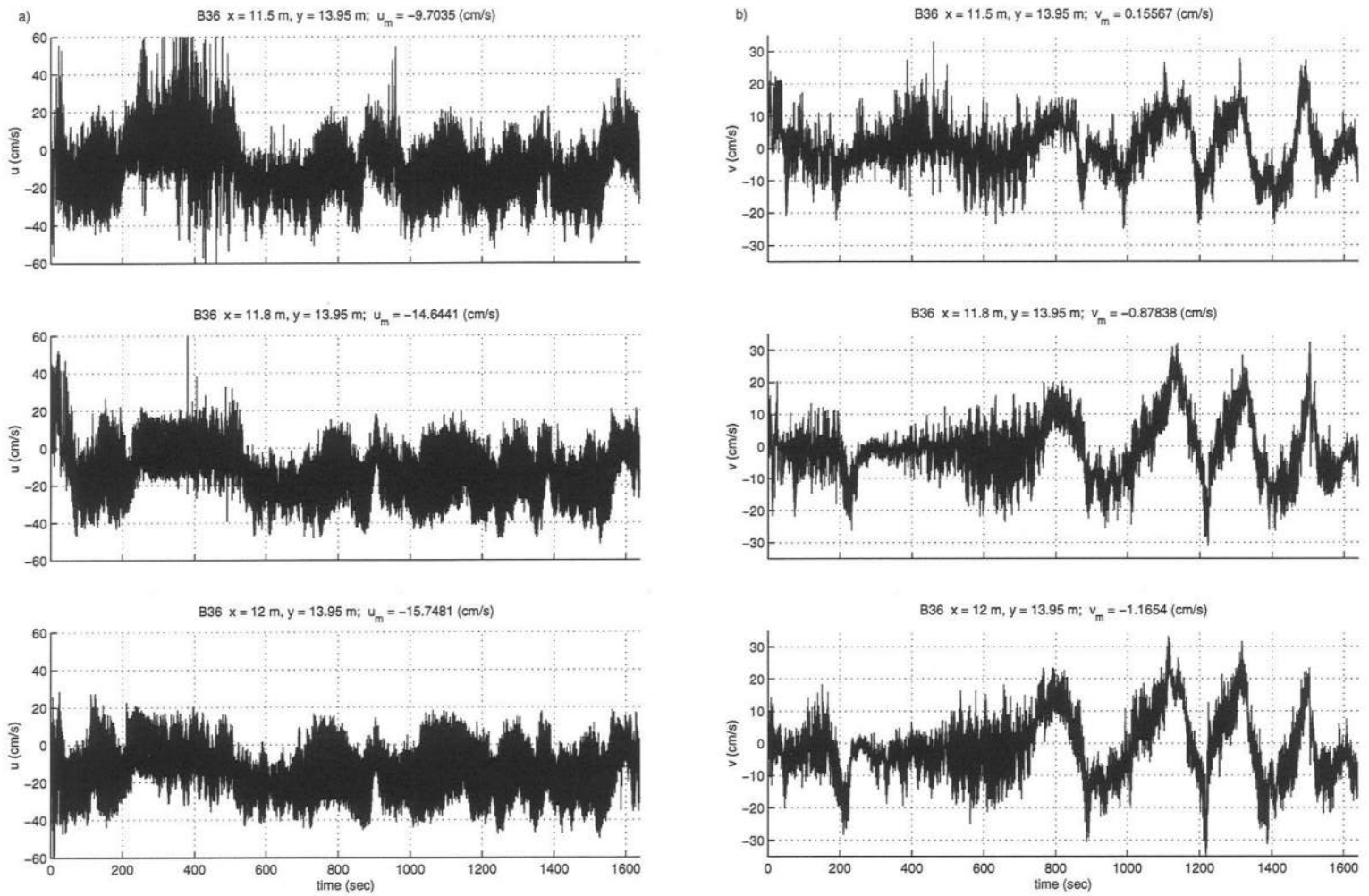

Figure 4.1: Time series of (*a*) cross-shore velocity (u) (*b*) longshore velocity (v) measured near the rip neck (B36; x=11.5 m,11.8 m,12.0 m; y= 13.95 m).

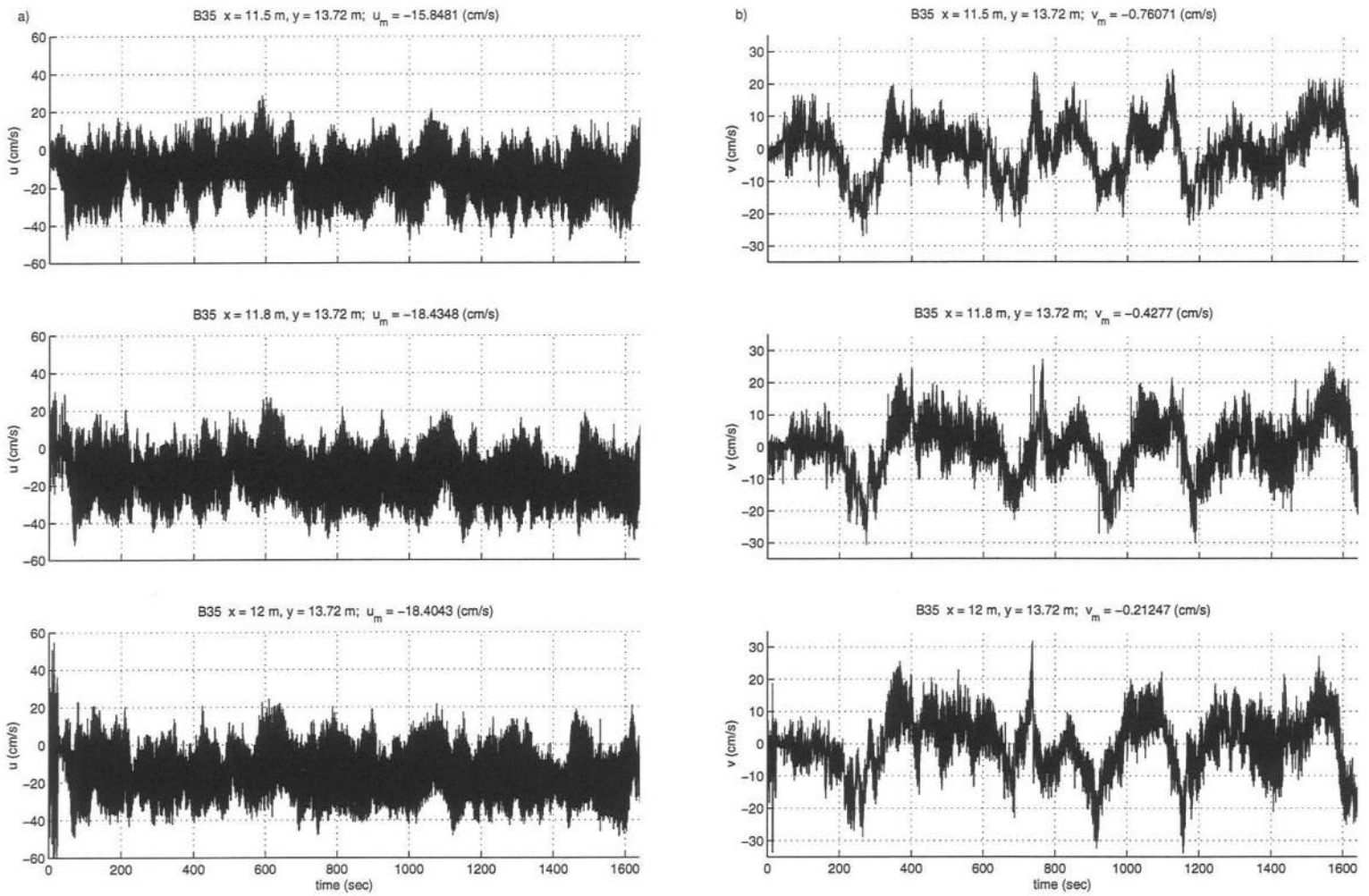

Figure 4.2: Time series of (*a*) cross-shore velocity (u) (*b*) longshore velocity (v) measured near the rip neck (B35; x=11.5 m,11.8 m,12.0 m; y= 13.72 m).

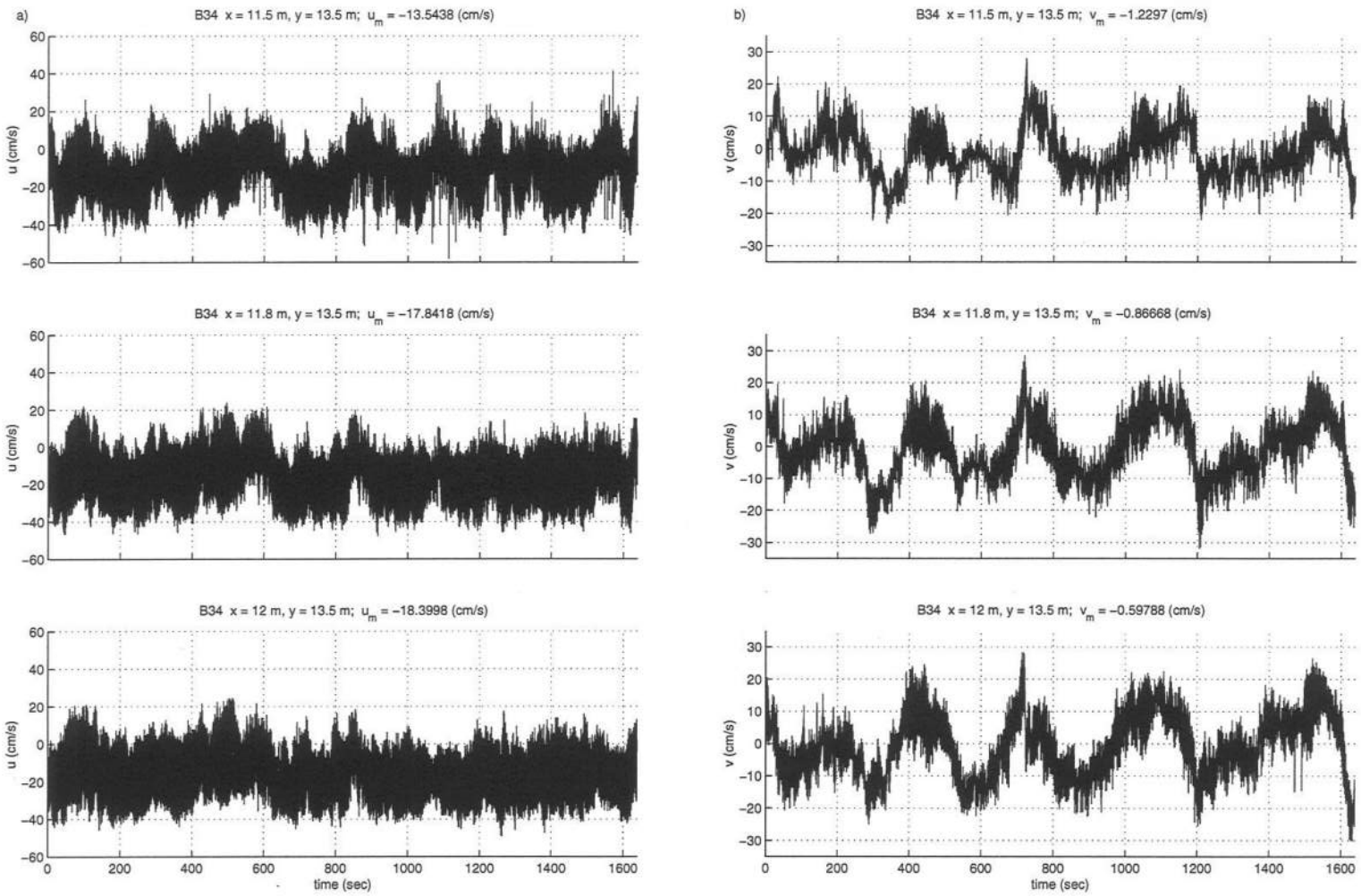

Figure 4.3: Time series of (*a*) cross-shore velocity (u) (*b*) longshore velocity (v) measured near the rip neck (B34; x=11.5 m,11.8 m,12.0 m; y= 13.5 m).

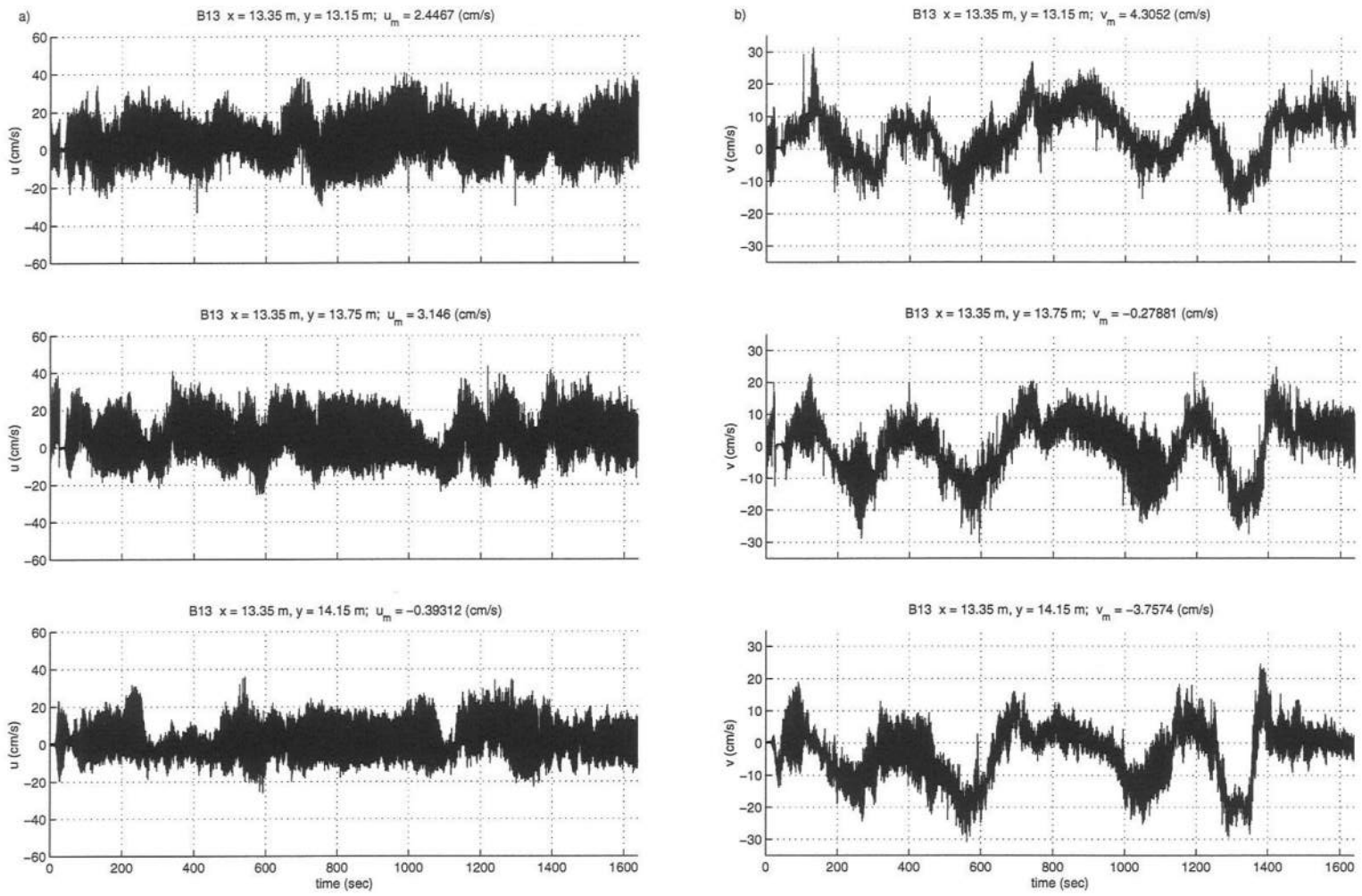

Figure 4.4: Time series of (*a*) cross-shore velocity (u) (*b*) longshore velocity (v) measured near the convergence of the feeder currents (B13; x=13.35 m; y= 13.15 m, 13.75 m, 14.15 m).

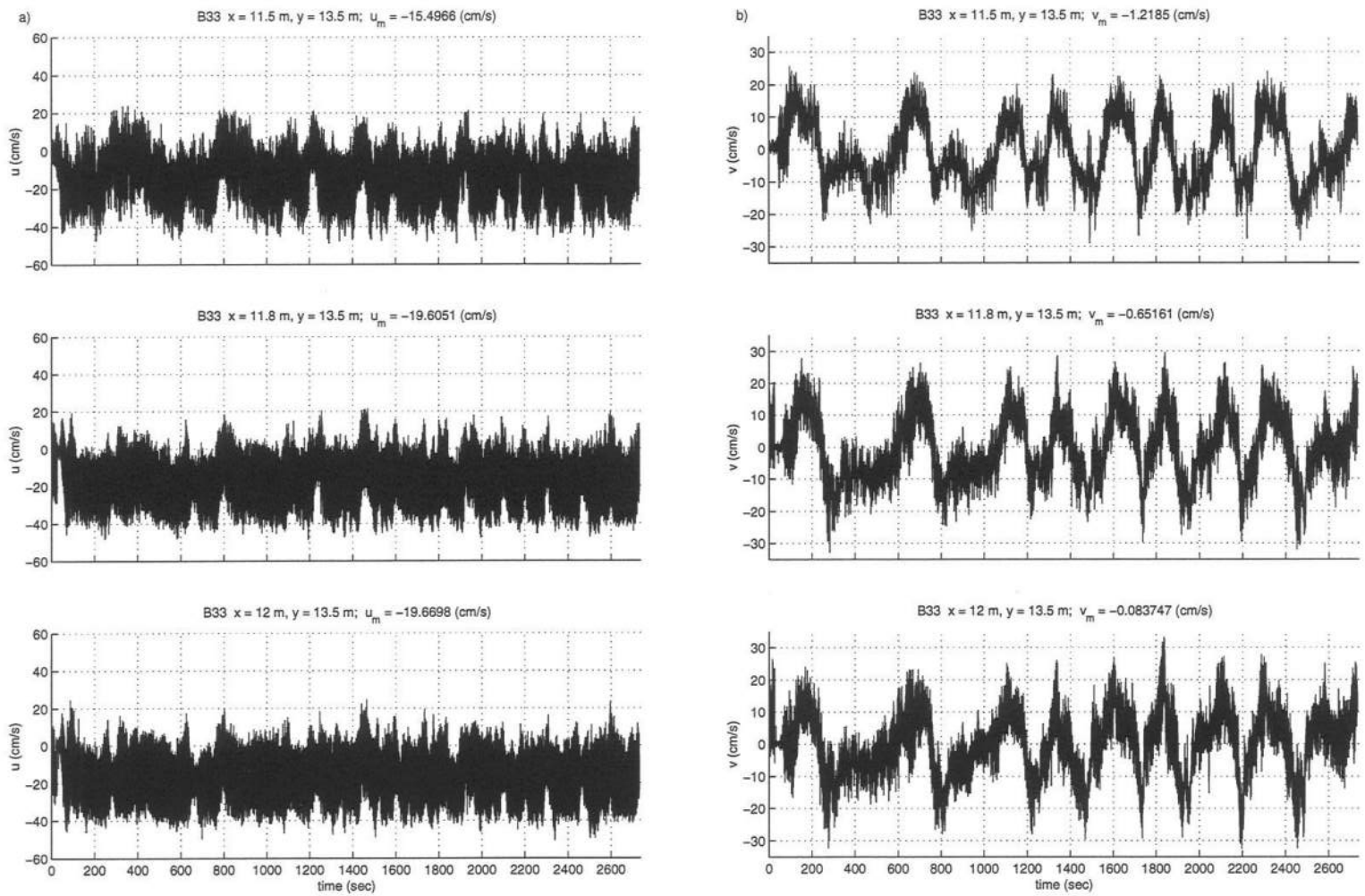

Figure 4.5: Extra long time series of (*a*) cross-shore velocity (u) (*b*) longshore velocity (v) measured near the rip neck (B33; x=11.5 m,11.8 m,12.0 m; y= 13.5 m).

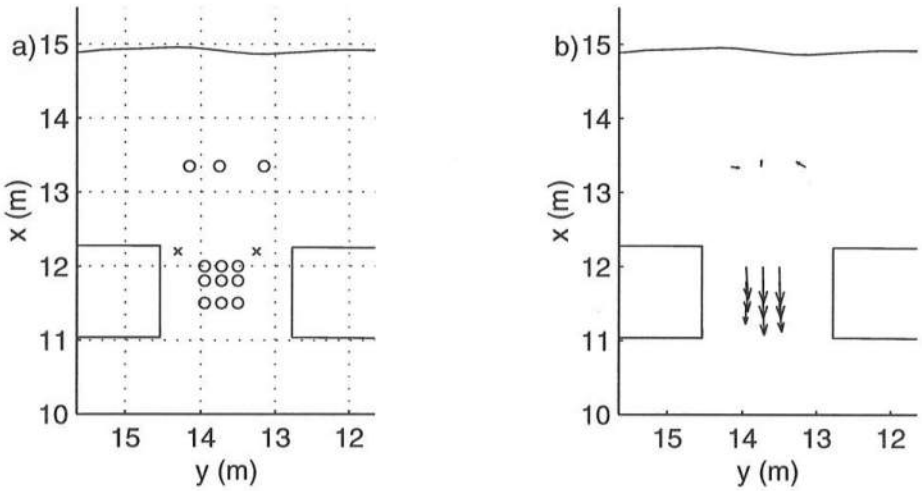

Figure 4.6: (*a*) Location of ADV's (o) and wave gauges (x) for time series shown in Figures 4.1-4.4 and 4.8, (*b*) mean current vectors corresponding to time series shown in Figures 4.1-4.4.

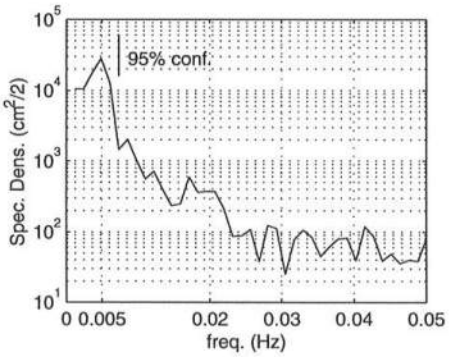

Figure 4.7: Average energy spectrum of longshore velocities measured near the rip neck (B33; 275.2<t<2732.7 s; x=11.5 m,11.8 m,12.0 m; y= 13.5 m), Δf=0.0012, d.o.f.=18.

currents measured near the channel centerline and the cross-channel water surface displacement ($\Delta\eta$) computed from the lowpass filtered water surface records measured during the same run by a pair of wave gages near the channel sides (see Figure 4.6a). Since the location of the rip current represents a local depression in the water level, the back and forth migration of the rip current is directly related to the mean water level gradients present in (or near) the rip channel. Visual inspection of the time series shows that the large oscillations about zero seen in the longshore component of the rip current are well correlated with the direction of the cross-channel water surface gradient. For example, at t=1400 s the water surface elevations indicate a positive cross-channel gradient ($\Delta\eta/\Delta y \approx 0.005$), while simultaneously the three ADV's located between the wave gages register a strong negative longshore flow towards the depression. Also, the zero-crossings of the longshore current record tend to occur simultaneously with zero-crossings of cross-channel surface displacement, indicating that, at the rip channel centerline, there is no longshore flow. This indicates that these very low frequency oscillations are directly related to the migration of the entire rip current structure back and forth in the channel.

It is also interesting to note that these low frequency rip migrations appear to have similar character from run to run. Figure 4.9 shows the filtered longshore records from runs B33-B36. The records indicate that the oscillations begin very early in each run, this suggests that the initiation of these migrations in a given experimental run is not a random phenomenon.

Near the exit of the rip channel the measured time series indicate the presence of low frequency oscillations with a different character. Figure 4.10 shows time series of cross- and longshore velocities measured just offshore of the rip channel during run B1. It is evident, especially in the longshore records, that at this location the longshore records are dominated by motions at shorter time scales than those present in the rip neck. These shorter scale oscillations are more readily seen in the

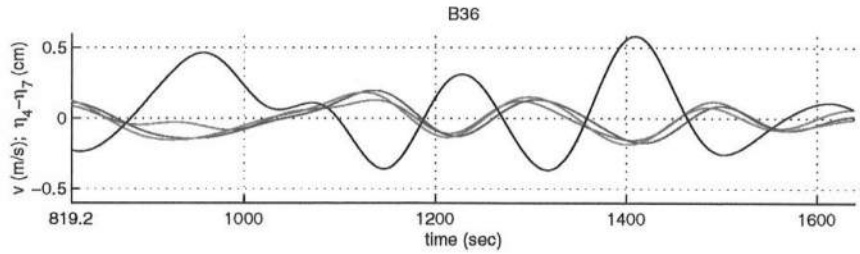

Figure 4.8: Lowpass filtered (f <0.01 Hz) time series of longshore velocities measured at x,y= (11.5 m, 13.95 m) - red, (11.8 m, 13.95 m) - blue, (12.0 m, 13.95 m) - green, and the cross-channel water surface gradient ($\eta_4 - \eta_7$) - solid black, computed from S7 measured at x,y=12.2 m,13.25 m, and S4 measured at x,y=12.2 m,14.3 m. Colors are defined in Figure 3.6.

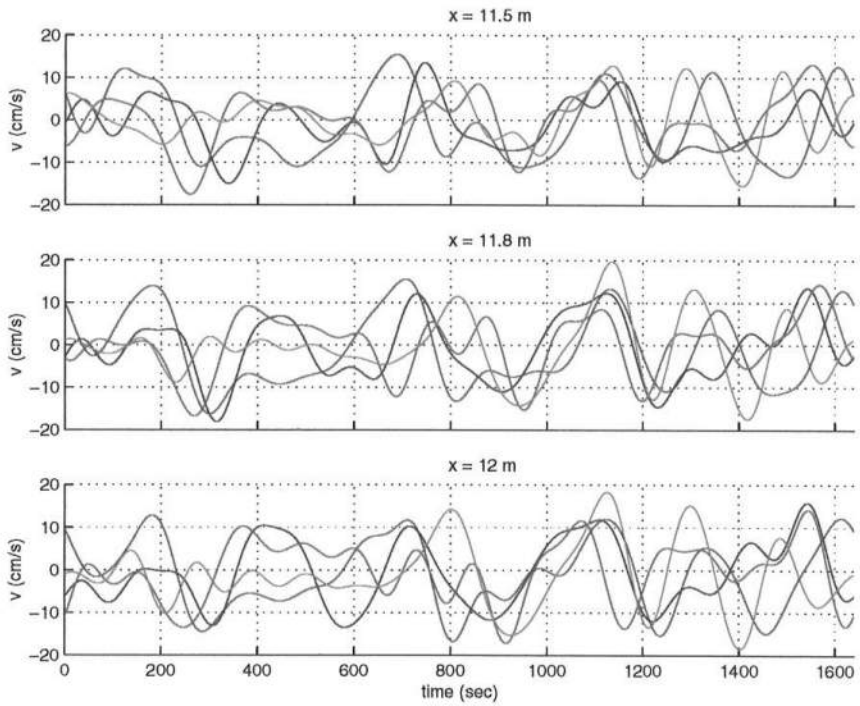

Figure 4.9: Lowpass filtered (f < 0.01 Hz) time series of longshore velocities measured during run B33, y=13.5 m, red; B34, y=13.5 m, blue; B35, y=13.72 m, green; and B36, y=13.95 m, cyan. Colors are defined in Figure 3.6.

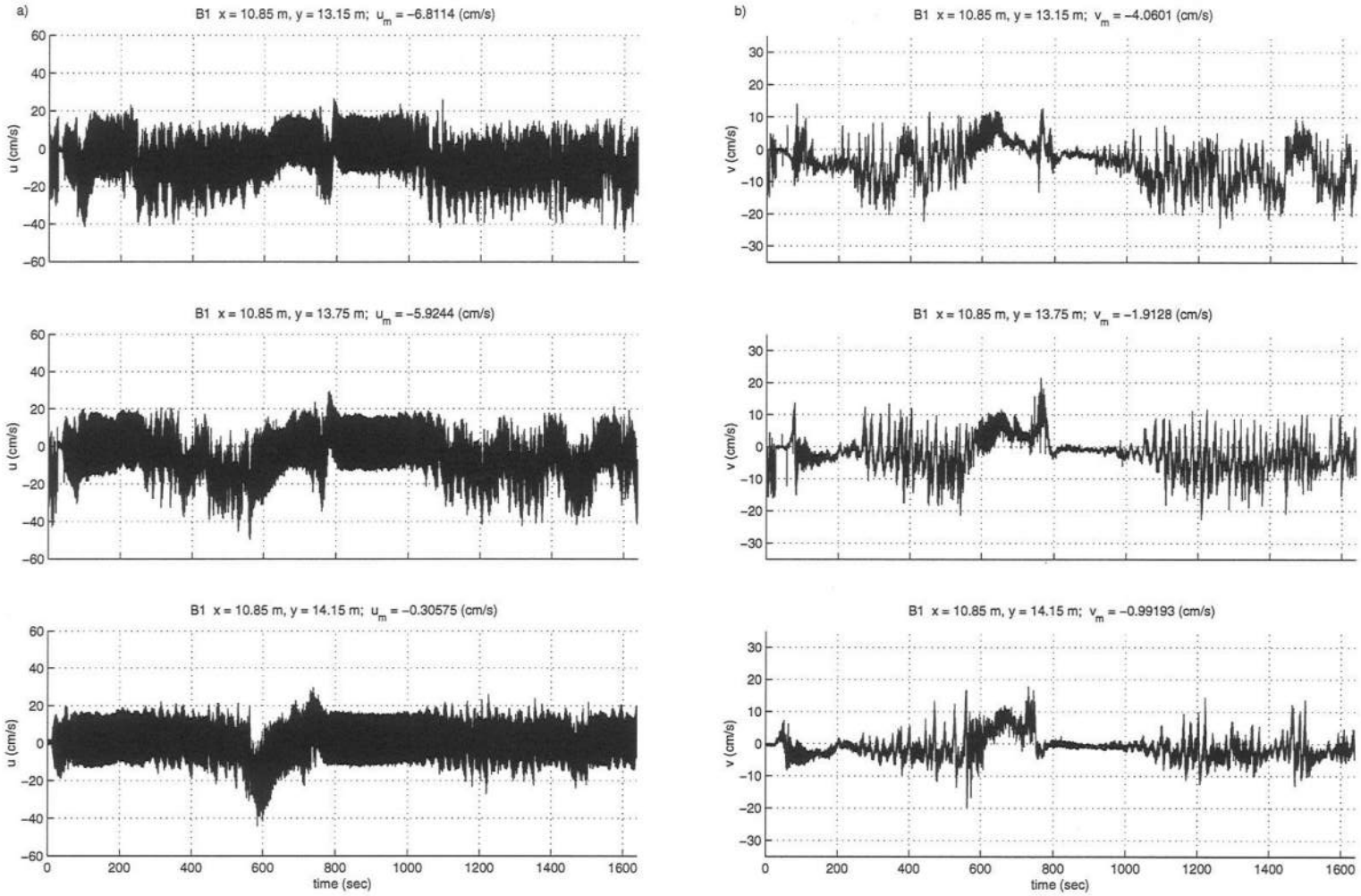

Figure 4.10: Time series of (*a*) cross-shore and (*b*) longshore velocities measured near the rip channel exit, (B1; x=10.85 m; y= 13.15 m, 13.75 m, 14.15 m).

longshore records, since they do not contain a significant incident wave signal, and are especially evident at 200<t<800 s and 1000<t<1400 s.

Another distinct feature of these particular records is the quiescent period between 800 s and 1000 s followed by the onset of the higher frequency oscillations. Notice that the strengthening of flow and the onset of oscillations occurs first at y=13.15 m and then at y=13.75 m and y=14.15 m at successively later times. The absence of offshore flow during the quiescent period and then the subsequent strengthening of the flow from one sensor to the next indicates that the rip current is initially located far from the sensors and then migrates towards the sensors in the positive y direction and this occurs at a slower time scale than the oscillations present within the rip itself.

Figure 4.11 shows the relationship between the lowpass filtered cross-shore velocity and the raw longshore current record from one sensor during run B1. It is clear from this figure that the onset of these oscillations corresponds to increasing offshore flow at the sensor. Additionally, there seems to be a correlation between the magnitude of the offshore flow and the amplitude of the oscillations. This strongly suggests that these oscillations are superimposed on the rip current and directly related to the strength of the offshore flow.

Figure 4.12 shows the decay of the short time scale oscillations in the offshore direction. The time series measured at x=10 m only shows limited oscillations and by x=9 m, the oscillations are almost nonexistent. The decay of the oscillations in the offshore direction is likely directly linked to the spreading of the jet-like rip current and the decay of the jet offshore of the channel. For reference, x=9 m is approximately 2 surf zone widths offshore of the still water line (x=14.9 m) during this test.

Figure 4.13 shows the averaged energy spectra of cross- and longshore velocities measured during run B1. In order to isolate the sections where the oscillations

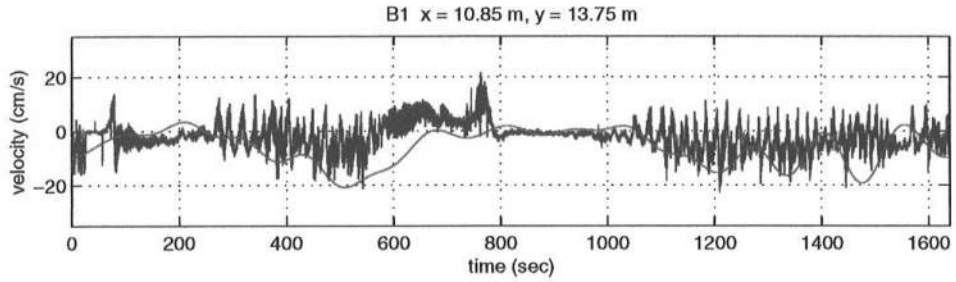

Figure 4.11: Raw time series of longshore velocites (blue) and lowpass filtered (f <0.01 Hz) cross-shore velocities (red) measured near the rip channel exit (B1; x=10.85 m; y=13.75 m). Colors are defined in Figure 3.6.

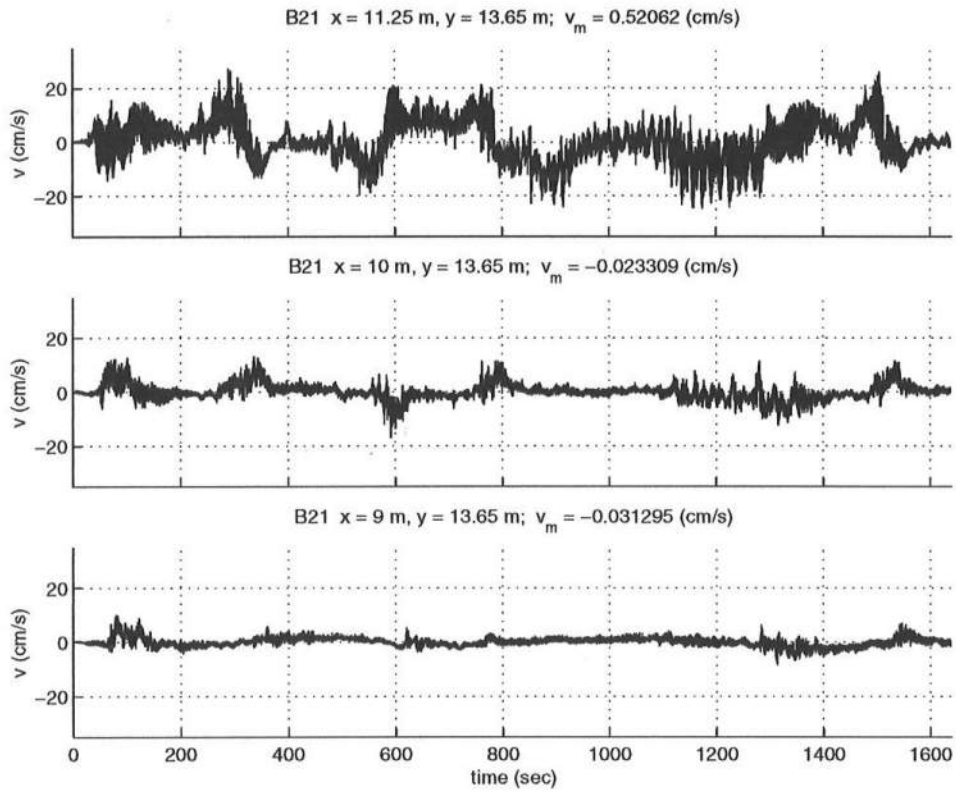

Figure 4.12: Time series of longshore velocities measured by a cross-shore array extending offshore from the rip channel exit (B21; x=11.25 m,10 m,9 m; y=13.65 m).

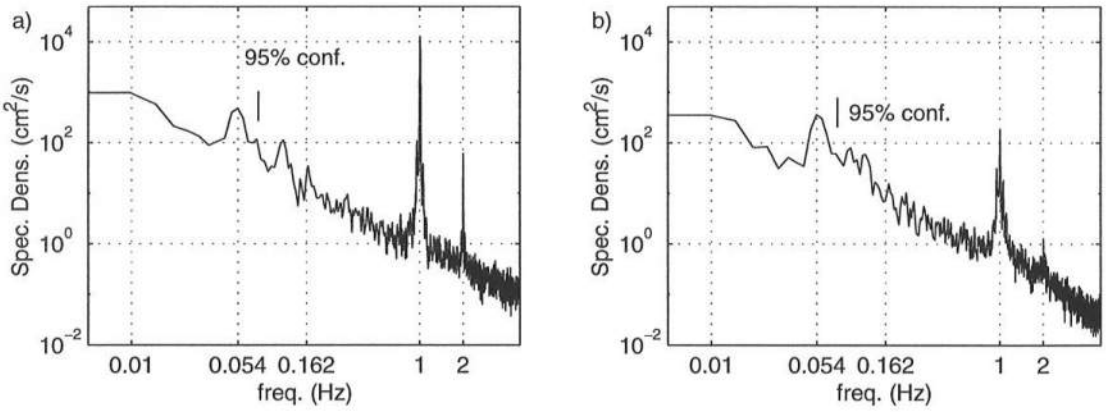

Figure 4.13: Energy spectra of (*a*) cross-shore and (*b*) longshore velocities measured near the rip channel exit (B1; 819.2<t<1638.4 s), Δf=0.0049 Hz, d.o.f.=24.

are most prevalent, only the last half of each time series (819.2<t<1638.4 s) was used in the spectral analysis. The spectra show distinct peaks near 0.054 Hz which corresponds to a period of approximately 18.5 s. In addition, there is some indication that higher harmonics of this 0.054 Hz oscillation are also present. The spectra from the cross-shore velocity record suggests energy is present at the first and second harmonics (0.108 Hz and 0.162 Hz, respectively).

It was difficult to visually observe these 18 s oscillations of the rip current. What was seen instead was the slower time meandering back and forth of the rip current in the channel. The strong correlation between the presence of a strong rip current and the detection of these short time scale oscillations suggests these oscillations are superimposed on the jet-like rip current. Since it is well known that jet-like flows are unstable and often turbulent, it is likely that rip current oscillations are generated by an instability mechanism driven by the shear in the rip current profile. The largest oscillations were those measured in the rip neck and caused the rip to migrate side-to-side. This rip migration also has consequences for the general circulation system, since the migrations cause the primary circulation cells to shrink

and stretch along with it. The oscillations observed offshore of the channel are of lesser magnitude and at significantly larger frequencies than those of the rip neck. However, though widely separated in frequency, the two oscillations may be related.

4.2 Test C

The experimental runs in Test C were undertaken after much of the analysis of Test B data had been performed. Since the rip current in Test B proved to be quite intermittent in character due to its large scale migrations, in Test C the intent was to further constrain the rip current in the rip channel so that the disturbances superimposed on the rip could be more thoroughly analyzed. To this end, the still water level in Test C was lowered by 2.06 cm such that the average depth at the bar crest was 2.67 cm, and the wave height was increased slightly (see Table 3.1).

Figures 4.14-4.15 show u and v time series measured in the rip channel during Test C. It is evident from the figures that the rip current is much less intermittent; regular fluctuations are present throughout the data records. In addition, the cross-shore records indicate that the rip current remains in the channel throughout the record. Figure 4.16 shows the averaged spectra of the cross-shore and longshore velocities for these time series computed using the last half of the records ($819.2<t<1638.4$). The longshore velocity spectrum clearly demonstrate a significant peak at 0.0146 Hz (T=68.5 s). The cross-shore velocity spectrum does not show a very distinct peak at this frequency, instead it shows a relatively broad range of low frequency energy extending from approximately 0.0037-0.02 Hz.

There is only very limited data from this test that indicate any intermittency of the rip current. Data measured at the edges of the rip channel do give some suggestion that the rip is migrating to a certain extent. It is evident from Figure 3.11b that the mean offshore flow was slightly biased towards the wall side of the channel. However, Figure 4.17 shows data measured at the opposite side of the channel (x=11.3 m, 11.5 m, 11.7m, y=12.8 m). The mean offshore flow is relatively

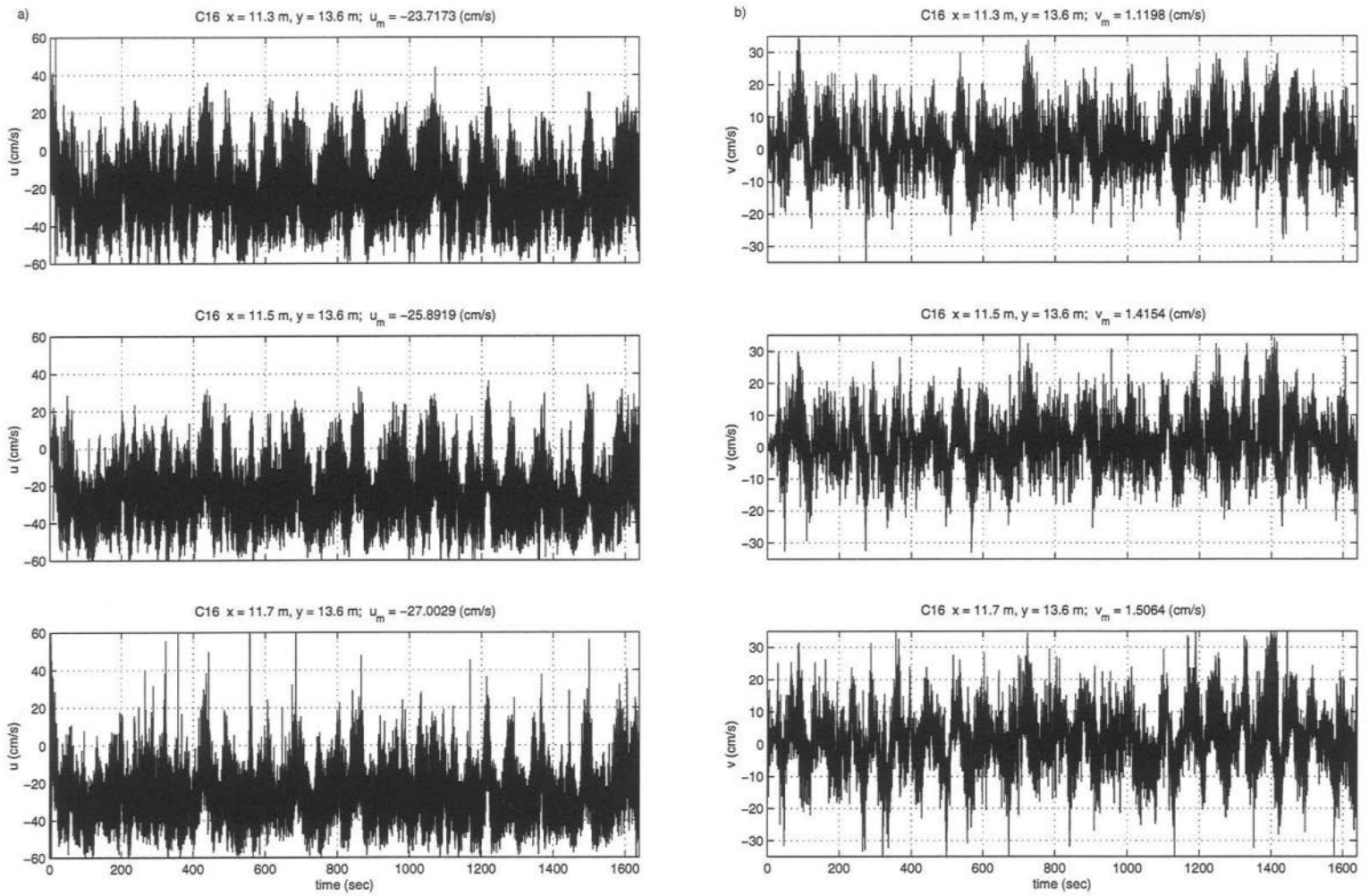

Figure 4.14: Time series of (*a*) cross-shore velocity (u) (*b*) longshore velocity (v) measured near the center of the rip channel (C16; x=11.3 m,11.5 m,11.7 m; y= 13.6 m).

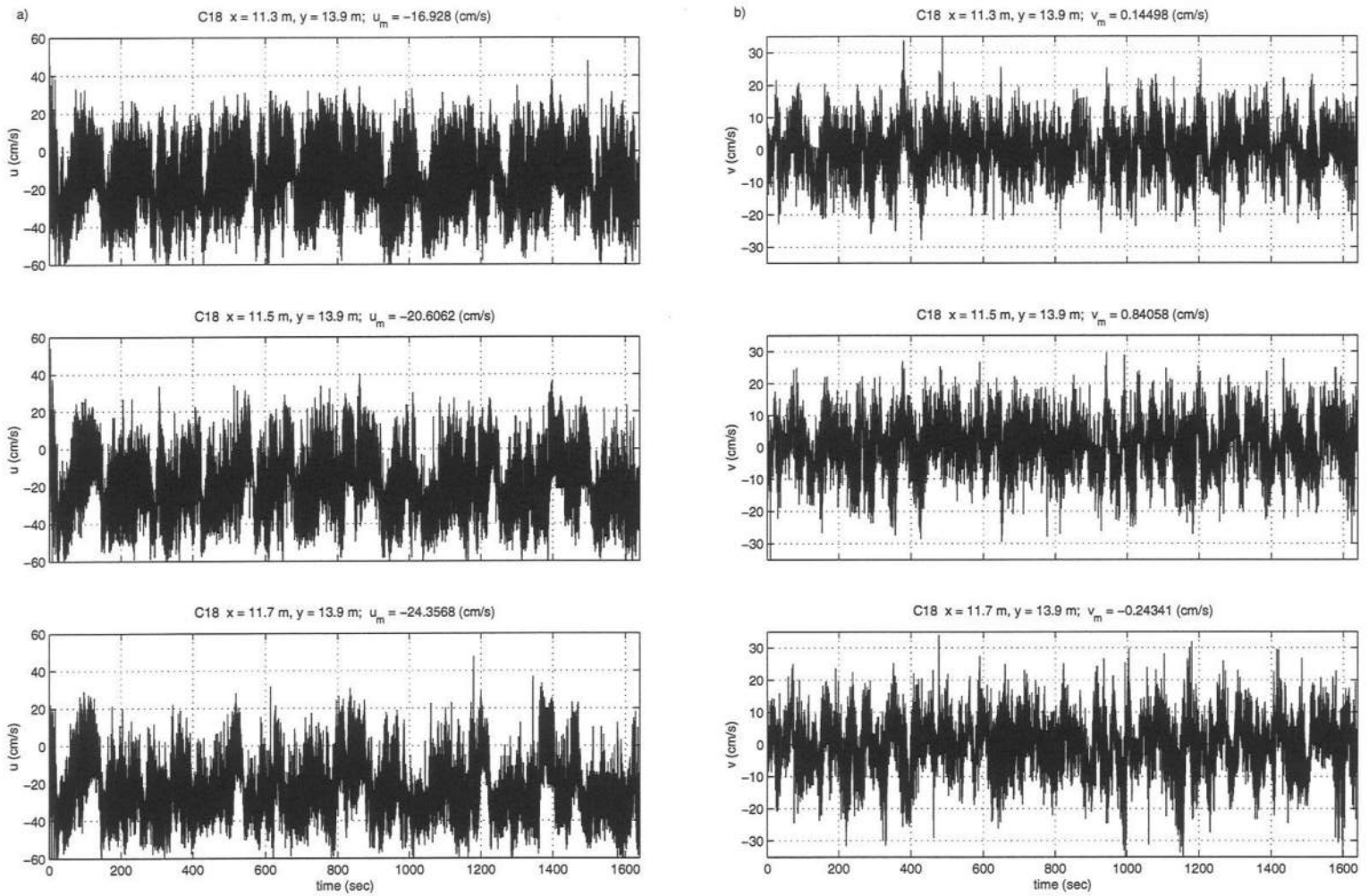

Figure 4.15: Time series of (left to right) (*a*)cross-shore velocity (u) (*b*)longshore velocity (v) measured near the rip neck (C18; x=11.3 m,11.5 m,11.7 m; y= 13.9 m).

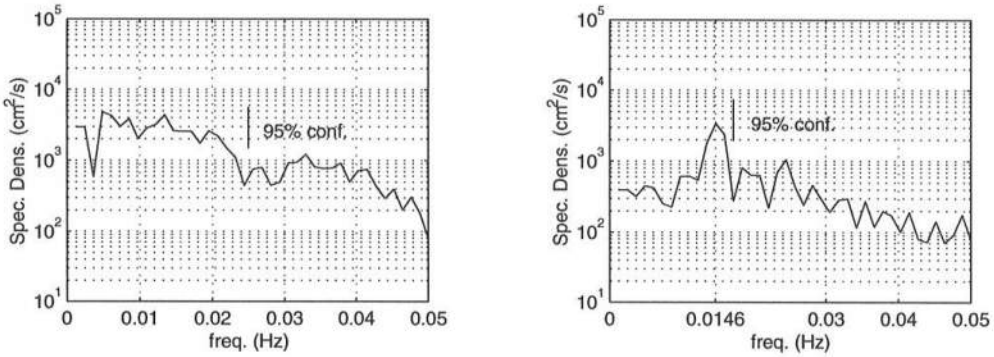

Figure 4.16: Averaged energy spectra of (*a*) cross-shore velocities and (*b*) longshore velocities measured at x=11.3 m, 11.5 m, and 11.7 m, y=13.6 m, 13.7 m, 13.9 m, (C16-18; 819.2<t<1638.4 s) Δf=0.0012 Hz, d.o.f.=18.

small at this location, but there is some indication that, at times, the offshore flow pulses (e.g. 800<t<1200 s). These pulses of current are likely the result of the side-to-side motion of the rip neck. Averaged spectra computed from the last half of these records are shown in Figure 4.18. Indeed, the longshore spectrum shows the presence of very low frequency energy near 0.005 Hz, along with a higher frequency peak near 0.0146 Hz.

The last experimental run during Test C was very long. The current meters were oriented in a cross-shore array very near the center of the rip channel and 6553.6 s (∼109 min.) of data were acquired. This run represents the ideal case for resolving the low frequency motions. The averaged spectra of u and v for this run are shown in Figure 4.19. The spectra clearly show energy peaks near 0.018 Hz in both the cross-shore and longshore velocities. However, the spectra also indicate a lower frequency peak at 0.01 Hz. Interestingly, the v spectrum also shows higher frequency peaks near 0.028, 0.036, and 0.044 Hz.

The spectra shown in Figure 4.19 presents a clearer picture of the low frequency oscillations in the rip current during this test. The somewhat noisier peaks

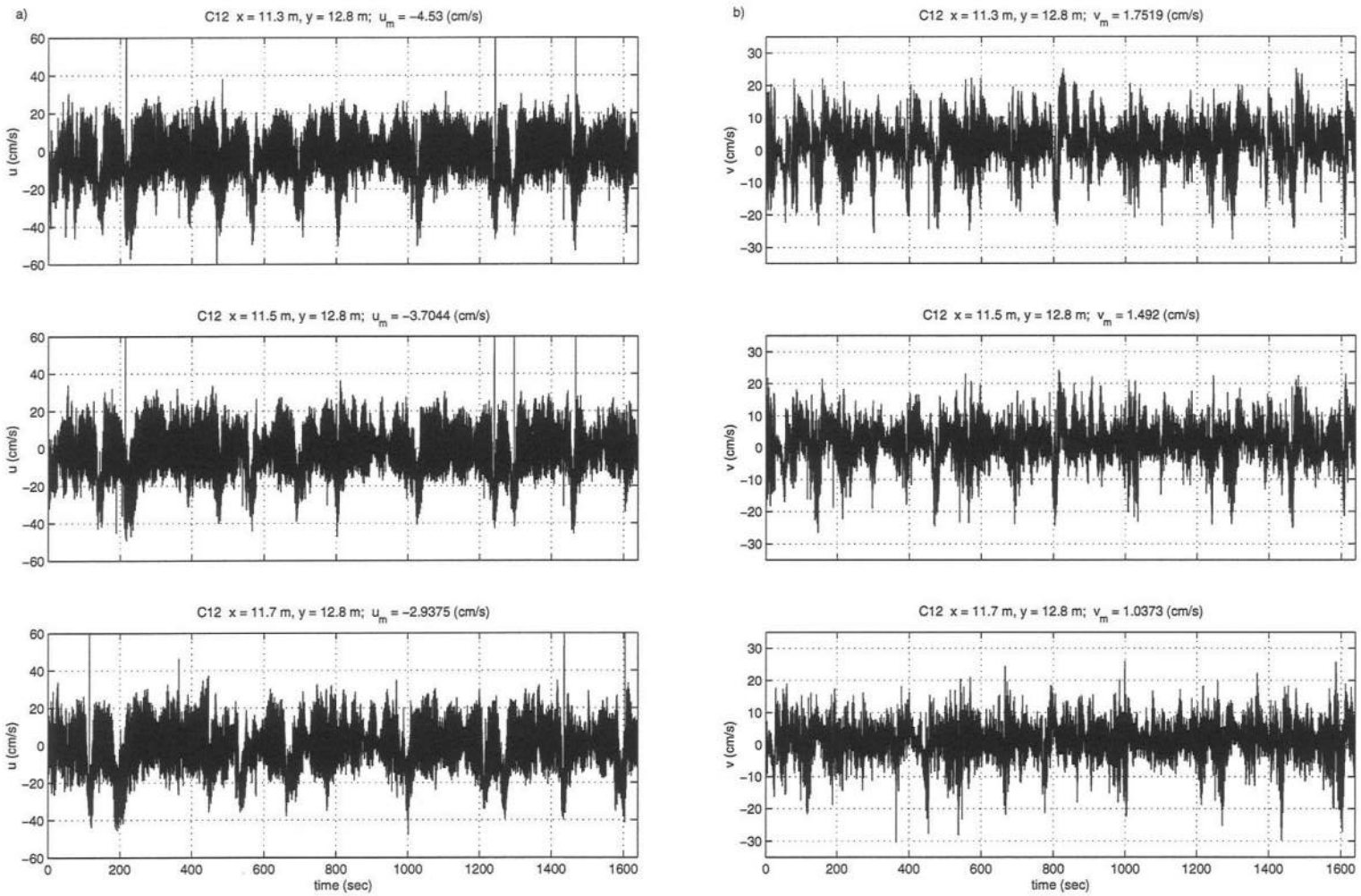

Figure 4.17: Time series of (*a*) cross-shore velocity (u) (*b*) longshore velocity (v) measured near the rip neck (C12; x=11.3 m,11.5 m,11.7 m; y= 12.8 m).

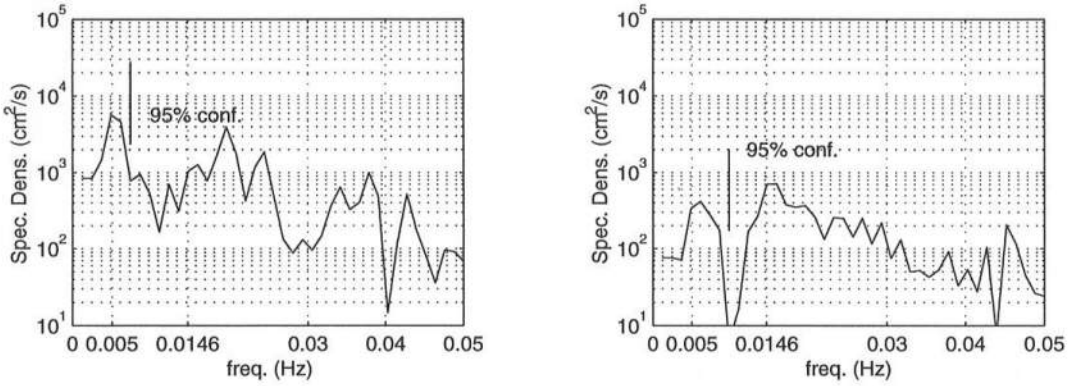

Figure 4.18: Averaged energy spectra of (a) cross-shore velocities and (b) longshore velocities measured at x=11.3 m, 11.5 m, and 11.7 m, y=12.8 m, (C12; 819.2< t <1638.4 s), Δf=0.0012 Hz, d.o.f.=6.

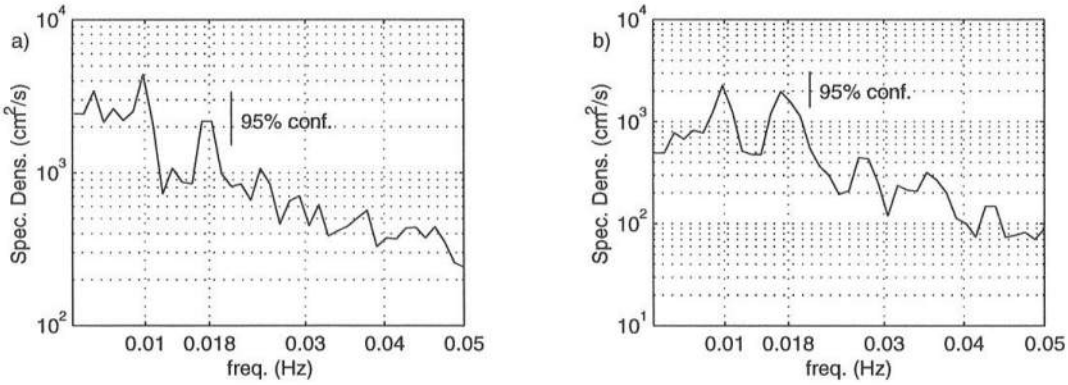

Figure 4.19: Averaged energy spectra of (a) cross-shore velocities and (b) longshore velocities from extra long time series measured at x=11.5 m, 11.7 m, and 12/0 m, y=13.6 m (C34; 0<t<6553.6 s), Δf=0.0012 Hz, d.o.f.=48.

seen in Figures 4.16 and 4.18 between 0.0146-0.02 Hz show up as a dominant peak centered on f_2=0.018 Hz in Figure 4.19. Also, the lower frequency energy of the previous spectra appear as another dominant peak centered on f_1=0.01 Hz. Furthermore, Figure 4.19 suggests that the two peaks are interacting nonlinearly, since the higher frequency peaks centered at 0.028 Hz and 0.036 Hz are a sum frequency $(f_1 + f_2)$ and a harmonic $(f_2 + f_2)$.

4.3 Tests D-G

Tests D through G were the last set of experiments. These tests were restricted in their measurement scope compared to the previous tests. Their purpose was to collect a limited set of measurements in order to characterize the mean circulation field under varying wave conditions. Rip current measurements were made along only three cross-shore lines in the rip channel. This allowed us to measure the strength and dominant location of the rip but did not provide as detailed a picture of the low frequency motions compared to the previous tests.

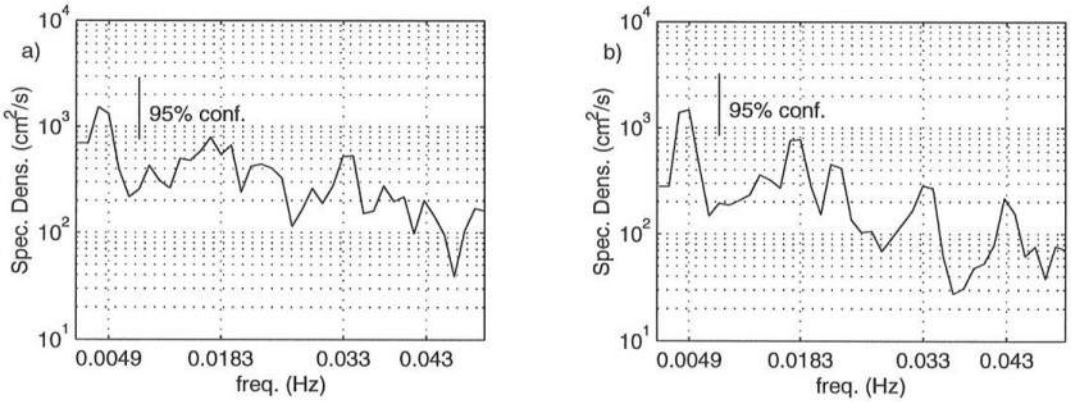

Figure 4.20: Averaged energy spectra of (a) cross-shore velocities and (b) longshore velocities measured at x=11.5 m, 11.7 m, and 12.0 m, and y=13.0 m, 13.6 m, and 14.2 m, (Test D, runs D1-3; 819.2<t<1638.4 s), Δf=0.0012 Hz, d.o.f.=18.

In order to characterize the low frequency rip current motions in Tests D-G, the data from the three runs when the ADV's were in the rip channel, (9 records) were used to compute the averaged rip current spectra for each test (Figures 4.20-4.23). As mentioned in the previous chapter, Test D had the highest wave height to bar crest depth ratio and, therefore, the strongest rip current. The spectra from Test D are shown in Figure 4.20. The longshore velocity spectrum shows numerous low frequency peaks, while in the cross-shore spectrum, the peaks are less distinct. The dominant longshore velocity peaks are at f_1=0.0049 Hz, f_2=0.0183 Hz, and f_3=0.033 Hz. Here, again, there appears to be interaction peaks at 0.013 Hz ($f_2 - f_1$) and 0.023 Hz ($f_2 + f_1$). However, it is difficult to determine more definitively whether these low frequency peaks are interacting nonlinearly. The multiple peaks might also indicate the presence of multiple linear modes existing independently.

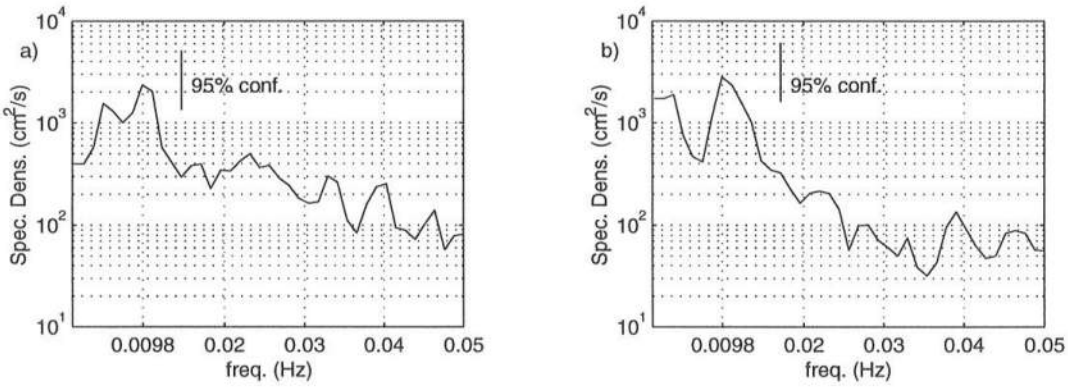

Figure 4.21: Averaged energy spectra of (a) cross-shore velocities and (b) longshore velocities measured at x=11.5 m, 11.7 m, and 12.0 m, and y=13.0 m, 13.6 m, and 14.2 m, (Test E, runs E1-3; 819.2<t<1638.4 s), Δf=0.0012 Hz, d.o.f.=18.

The rip current in Test E was similar in strength to Test B. In addition, it was noted during Test B that spectra taken from within the rip channel only demonstrated very low frequency (0.005 Hz) peaks. Similarily, spectra from Test E

(Figure 4.21) do not show numerous energetic peaks above 0.01 Hz. Instead, Test E shows very low frequency peaks near 0.005 Hz and 0.01 Hz in both cross-shore and longshore velocity spectra. In addition, unlike during Test B, simultaneous wave data were not recorded near enough to the rip channel to compare water surface elevations with the longshore velocities during Tests D-G.

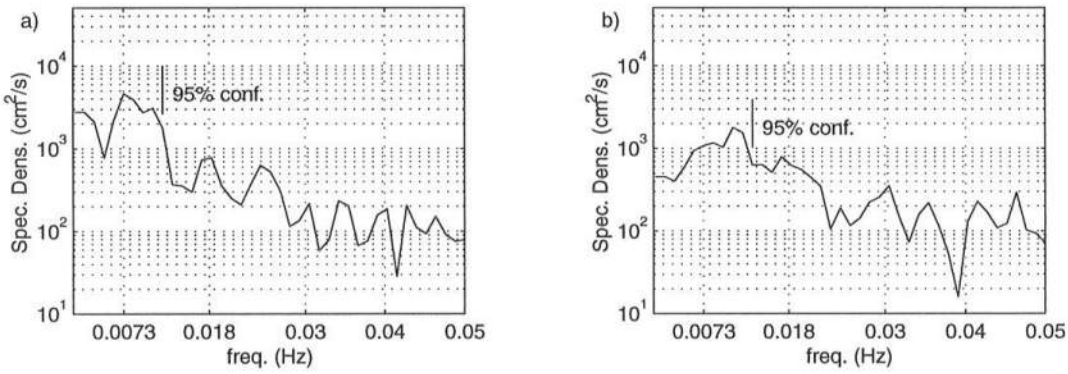

Figure 4.22: Averaged energy spectra of (*a*) cross-shore velocities and (*b*) longshore velocities measured at x=11.5 m, 11.7 m, and 12.0 m, and y=13.0 m, 13.6 m, and 14.2 m, (Test F, runs F1-3; 819.2<t<1638.4 s), Δf=0.0012 Hz, d.o.f.=18.

The experimental conditions used in Test F were chosen for the purpose of evaluating the effects of oblique incidence on the mean circulation system. The wave height to bar crest depth ratio was relatively small during Test F compared to the other tests; however, the additional longshore forcing due to oblique wave incidence led to a stronger rip current in the channel where the measurements were made. The oblique wave incidence presents certain problems in evaluating the low frequency rip current motion in terms of the presence of instabilities. In particular, near x=11 m, the incident plane wave began to reflect from the sidewall nearest the rip channel in which the velocity measurements were made. In addition, the rip current itself exited the rip channel obliquely towards the sidewall and, therefore, may have been affected by the presence of the sidewall at its downstream end.

Nevertheless, it is interesting to note in the averaged spectra shown in Figure 4.22, that low frequency peaks appear more distinct in the cross-shore velocity spectrum than in the longshore velocity spectrum, and the peaks again appear to be around 0.01 Hz and 0.018 Hz.

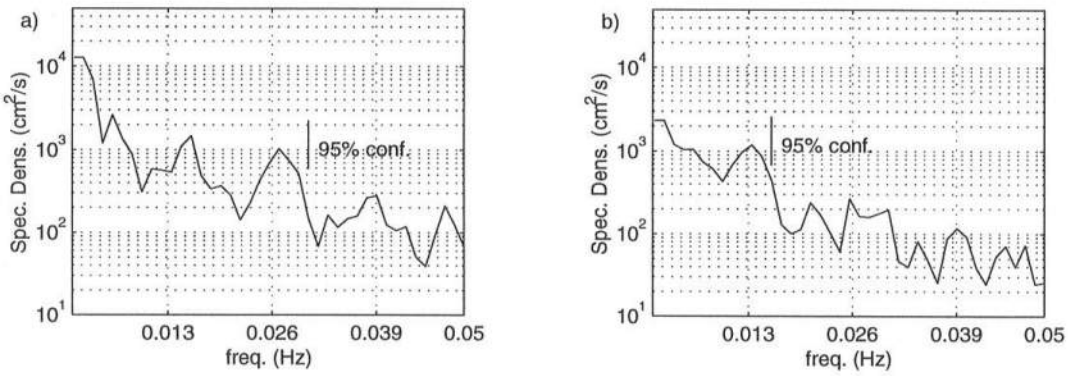

Figure 4.23: Averaged energy spectra of (a)cross-shore velocities and (b) longshore velocities measured at x=11.5 m, 11.7 m, and 12.0 m, and y=13.0 m, 13.6 m, and 14.2 m, (Test G, runs G1-3; 819.2< t <1638.4 s), Δf=0.0012 Hz, d.o.f.=18.

The still water level during the Test G was the highest of all the tests. This combined with the relatively smaller wave height to bar crest depth ratio allowed the rip current more freedom of movement around the channel. The low frequency spectra from Test G are shown in Figure 4.23. The longshore velocity spectrum suggests the presence of energy near 0.013 Hz and 0.026 Hz and 0.039 Hz, again suggesting harmonics are present.

The collection of low frequency spectra from all the tests indicates the presence of energetic low frequency motions during these experiments. Specific very low frequency (0.005 Hz) oscillations were shown to be consistent with the slow, side to side migration of the rip neck during Test B. It should be noted that while the effect of a rip current migrating to opposite sides of a given ADV appears as large shifts from positive to negative in the longshore velocities, this signal is perhaps

significantly modified for an ADV located near the sides of the rip channel. The ADV's located at the channel sides tend to measure only one side of the rip current and therefore do not necessarily have many zero crossings in their longshore records. This most likely leads to spreading of energy in the lowest frequencies during the spectral analysis.

4.4 Wave Basin Seiching

In the following section we will investigate wave basin seiching as a potential source for low frequency energy during the experiments. Any given basin, whether enclosed or open to an outside reservoir, will oscillate at its natural frequencies if it is excited by some type of forcing. These natural basin modes are termed seiche modes. Wave generation in an enclosed basin often causes basin seiching due to wave reflections or wave grouping effects that can transfer wave energy to low frequencies. In addition, since the basin is enclosed and energy cannot be radiated away, any continuous forcing will cause the seiche modes to grow until they reach an equilibrium state, where the forcing is matched by dissipation. It is important, therefore, to quantify any influence of seiching on these experiments, especially in regard to the interpretation of the low frequency rip current fluctuations.

In order to determine a solution for the basin seiche modes, we begin with the two-dimensional shallow water wave equation for variable depth given by

$$\eta_{tt} - (gh\eta_x)_x - (gh\eta_y)_y = 0, \tag{4.1}$$

where η is water surface elevation, h is water depth, and subscripts represent derivatives. We will assume that the seiche modes are periodic in the longshore direction and in time, and have some arbitrary distribution in the cross-shore direction such that η can be expressed as

$$\eta(x, y, t) = \zeta_m(x) \cos(\frac{n\pi y}{W}) \cos(\omega t), \tag{4.2}$$

Test C-F h_0=70.36 cm		Test B h_0=72.42 cm		Test G h_0=74.41 cm		
T (s)	T^{-1} (Hz)	T (s)	T^{-1} (Hz)	T (s)	T^{-1} (Hz)	n,m
27.8	.036	27.4	.036	27.2	.037	1,0
22.9	.044	22.7	.044	22.6	.044	0,1
19.7	.051	19.2	.052	18.9	.053	2,0
16.4	.061	16.1	.062	16.0	.063	1,1
16.0	.063	15.5	.065	15.3	.065	4,0

Table 4.1: Table of the first five (largest period) seiche modes for each water level, n is number of longshore zero crossings, m is number of cross-shore zero crossings.

where ζ_m is the eigenvector representing the cross-shore wave form, n is the longshore mode number, W is the width of the basin, and ω is the wave frequency. Substituting Eq. 4.2 into Eq. 4.1 and assuming a longshore uniform bathymetry ($h_y = 0$) we obtain the following governing equation for the seiche modes:

$$-gh\zeta_{m_{xx}} - gh_x\zeta_{m_x} + \frac{ghn^2\pi^2}{W^2}\zeta_m = \omega^2\zeta_m. \tag{4.3}$$

The boundary conditions for this problem are an impermeable wall at the wavemaker and finite wave amplitude at the shoreline. In order to implement the shoreline boundary condition it is convenient to make the following variable transformation $\xi = \zeta_m \cdot x$ and to orient the coordinate axis such that the still water shoreline is at $x = 0$ and the wavemaker is at $x = L$. Therefore the transformed governing equation is now

$$-gh\xi_{xx} + \left(\frac{2gh}{x} - gh_x\right)\xi_x + \left(\frac{gh_x}{x} - \frac{2gh}{x^2} + \frac{ghn^2\pi^2}{W^2}\right)\xi = \omega^2\xi. \tag{4.4}$$

with boundary conditions

$$\xi = 0 \qquad\qquad x = 0 \tag{4.5}$$

$$\zeta_x = \frac{\xi_x}{x} - \frac{\xi}{x^2} = 0 \qquad\qquad x = L. \tag{4.6}$$

Equation 4.4 is an eigenvalue problem for which nontrivial solutions (ξ) exist for only certain eigenvalues (ω^2). To solve this eigenvalue problem we use a finite difference method. The cross-shore depth profiles measured over the center bar section were discretized and Eq. 4.4 was written in matrix form using central differences ($O(\Delta x^2)$). The eigenvalues and eigenvectors are then solved for each longshore mode using a matrix eigenvalue solver. Table 4.1 lists the periods and mode numbers of the first five seiche modes for the three different water levels used in the experiments.

The table shows that the period of a given seiche mode does not change significantly for the range of water depths used in these experiments. It is expected that the lowest frequency modes will be the most energetic since they experience less frictional damping. The predicted spatial variations of the seiching variance (amplitude squared) for the water surface elevation and horizontal velocities are shown in Figures 4.24-4.28 for the first five seiche modes. Each mode is normalized such that the maximum water surface variance equals 1 cm^2 at the shoreline.

It is evident from these figures that while certain modes show a concentration of cross-shore variance near the bar crests, most of the variance in water surface and velocities is located close to the shoreline. However, it is interesting to note that the mode shown in Figure 4.26 has a concentration of longshore variance along the rip channel axes. Nonetheless, the calculated frequency for this mode is $\geq$0.051 Hz for all water depths, which is above almost all of the frequency peaks discussed in Sections 4.1-4.3.

It is useful to compare the predicted variation of the seiching variances with the measured values. Figures 4.29-4.31 show the measured variances (standard deviation squared) of the experimental data (Test B) in three frequency bands. The data were divided into a low frequency (0<f<0.01 Hz), mid-frequency (0.01<f<0.75 Hz), and incident frequency (0.75<f<5 Hz) bands and the variance in each band

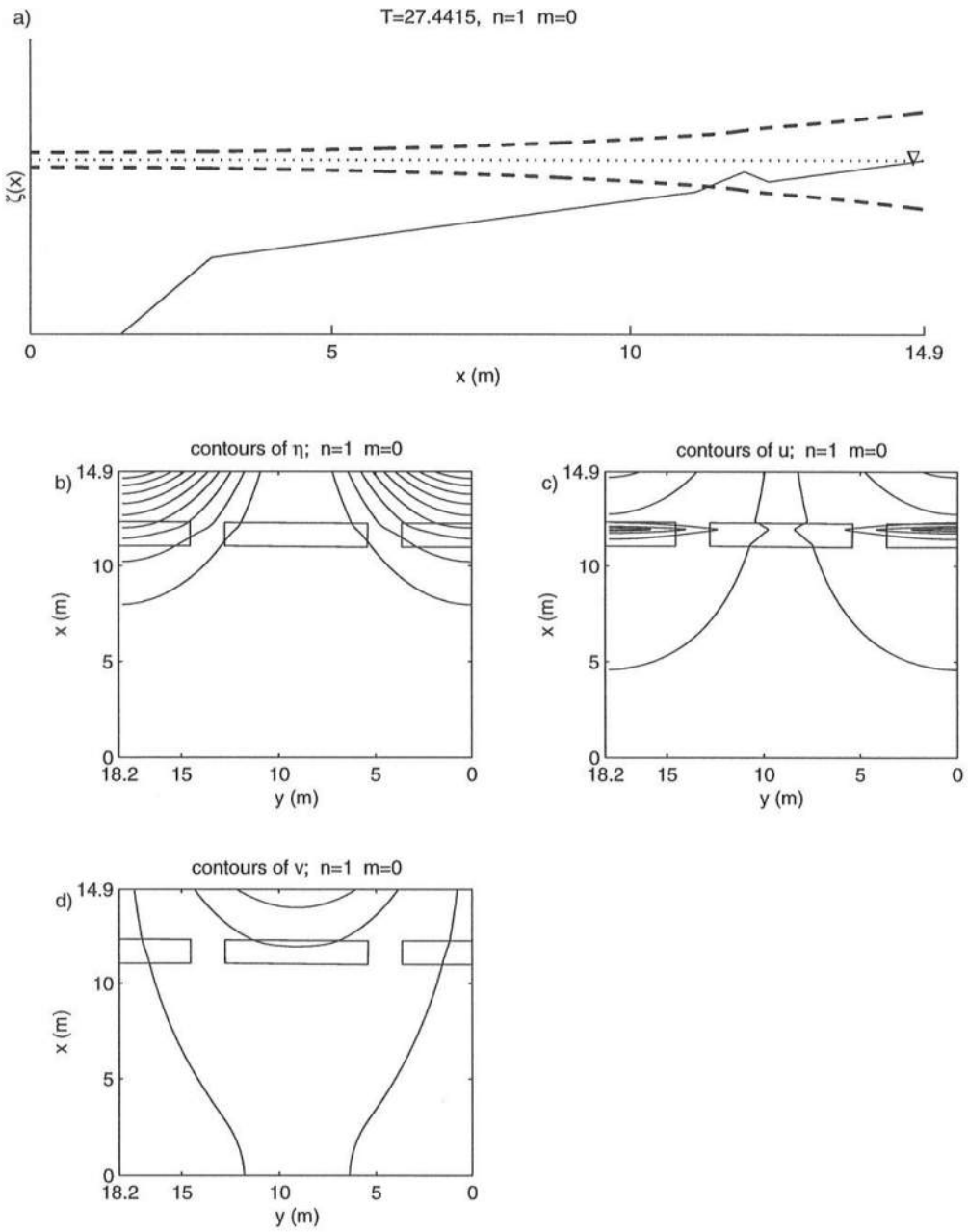

Figure 4.24: Calculated results of (*a*) cross-shore wave form ζ_0(x) (*b*) normalized variance of η (*c*) normalized variance of u and (*d*) normalized variance of v for T=27.4 s, Test B.

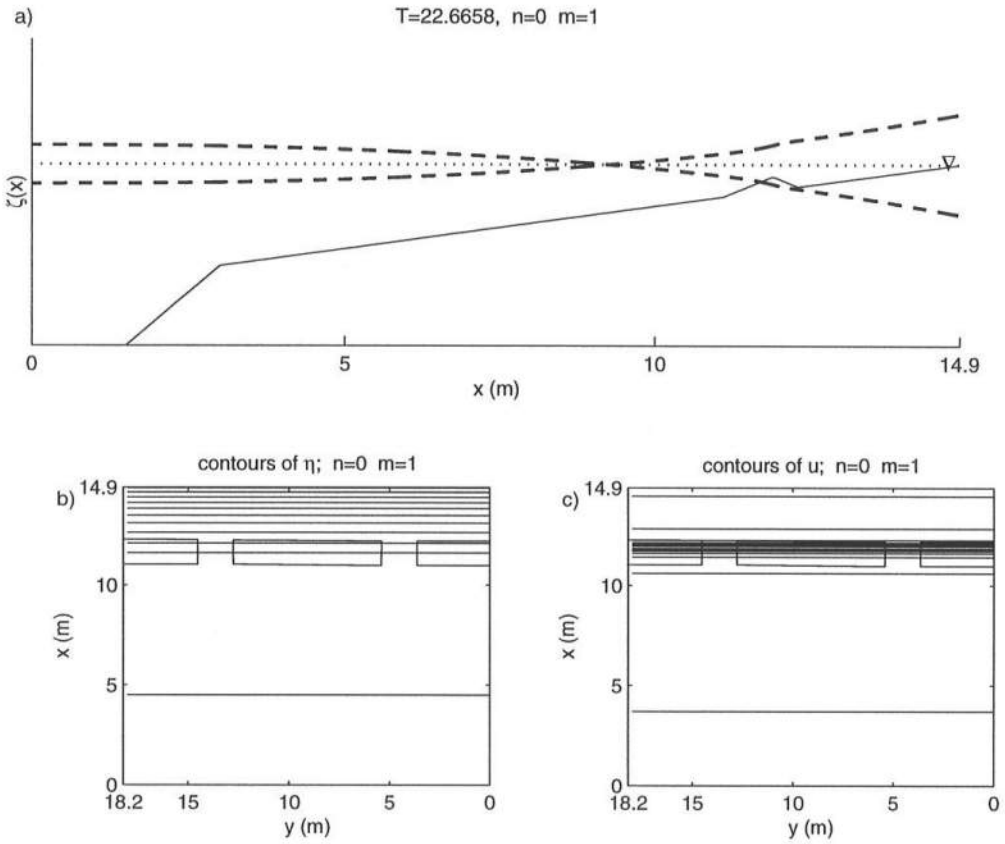

Figure 4.25: Calculated results of (a) cross-shore wave form ζ_1(x) (b) normalized variance of η and (c) normalized variance of u for T=22.7 s, Test B.

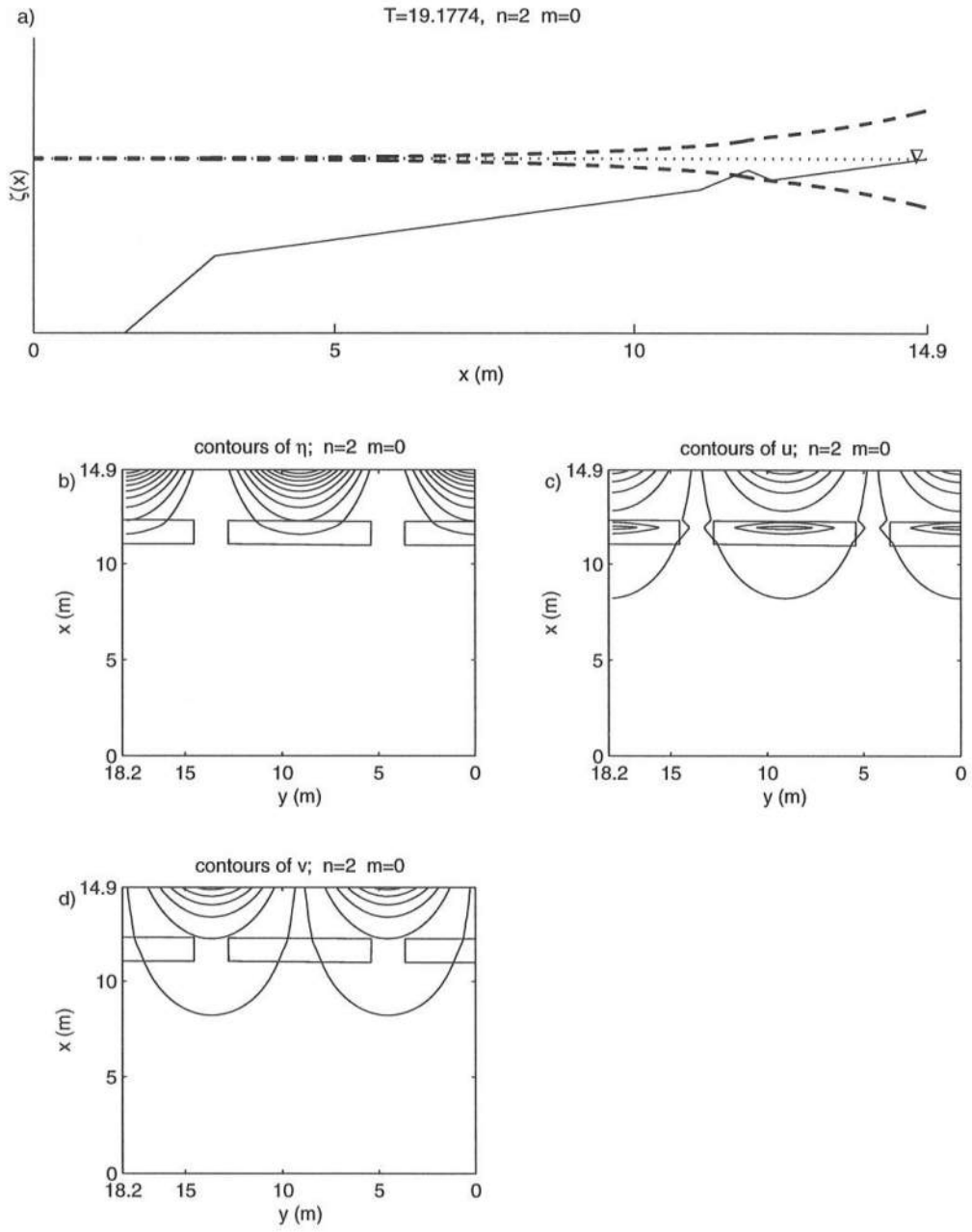

Figure 4.26: Calculated results of (a) cross-shore wave form ζ_0(x) (b) normalized variance of η (c) normalized variance of u and (d) normalized variance of v for T=19.2 s, Test B.

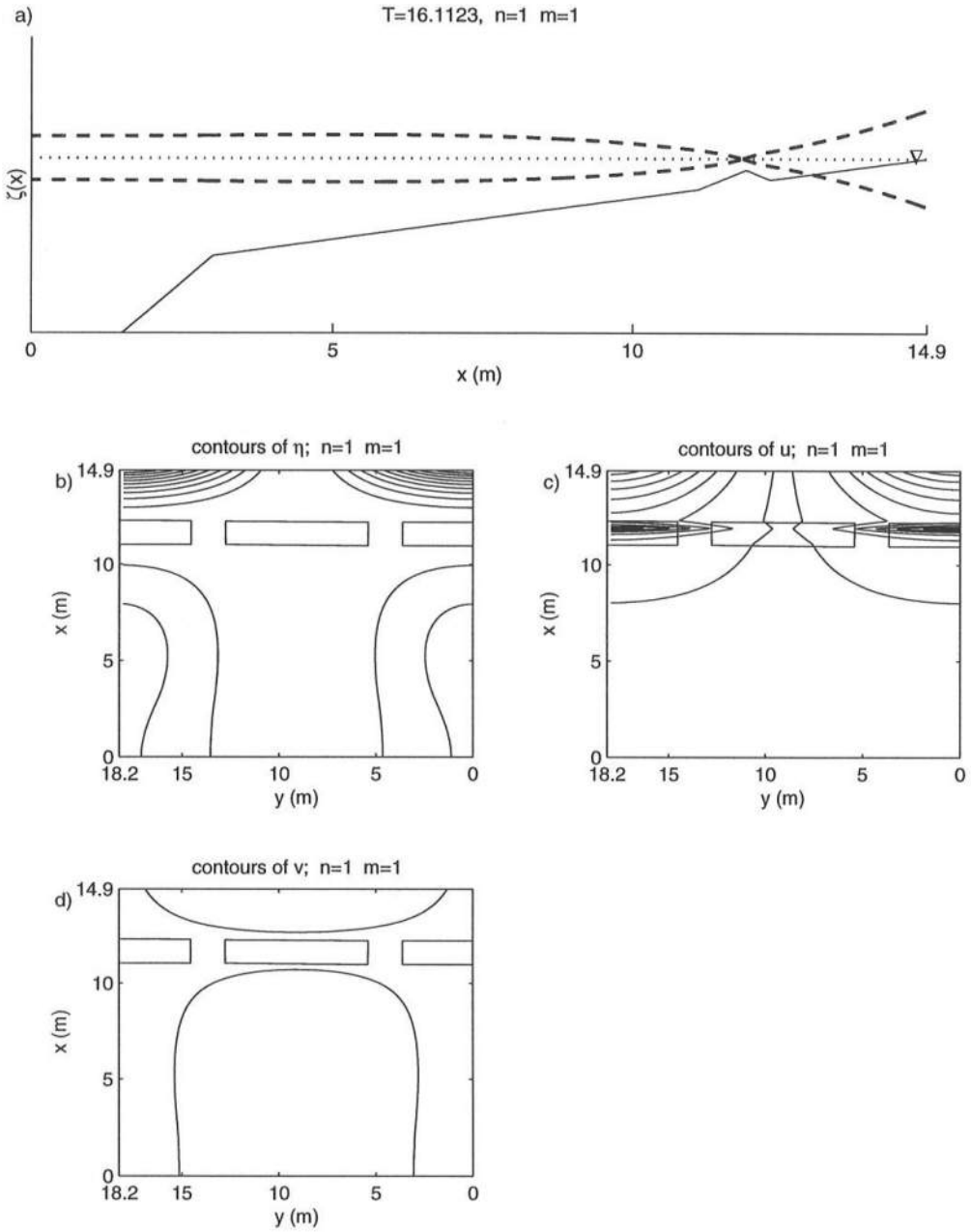

Figure 4.27: Calculated results of (*a*) cross-shore wave form ζ_1(x) (*b*) normalized variance of η (*c*) normalized variance of u and (*d*) normalized variance of v for T=16.1 s, Test B.

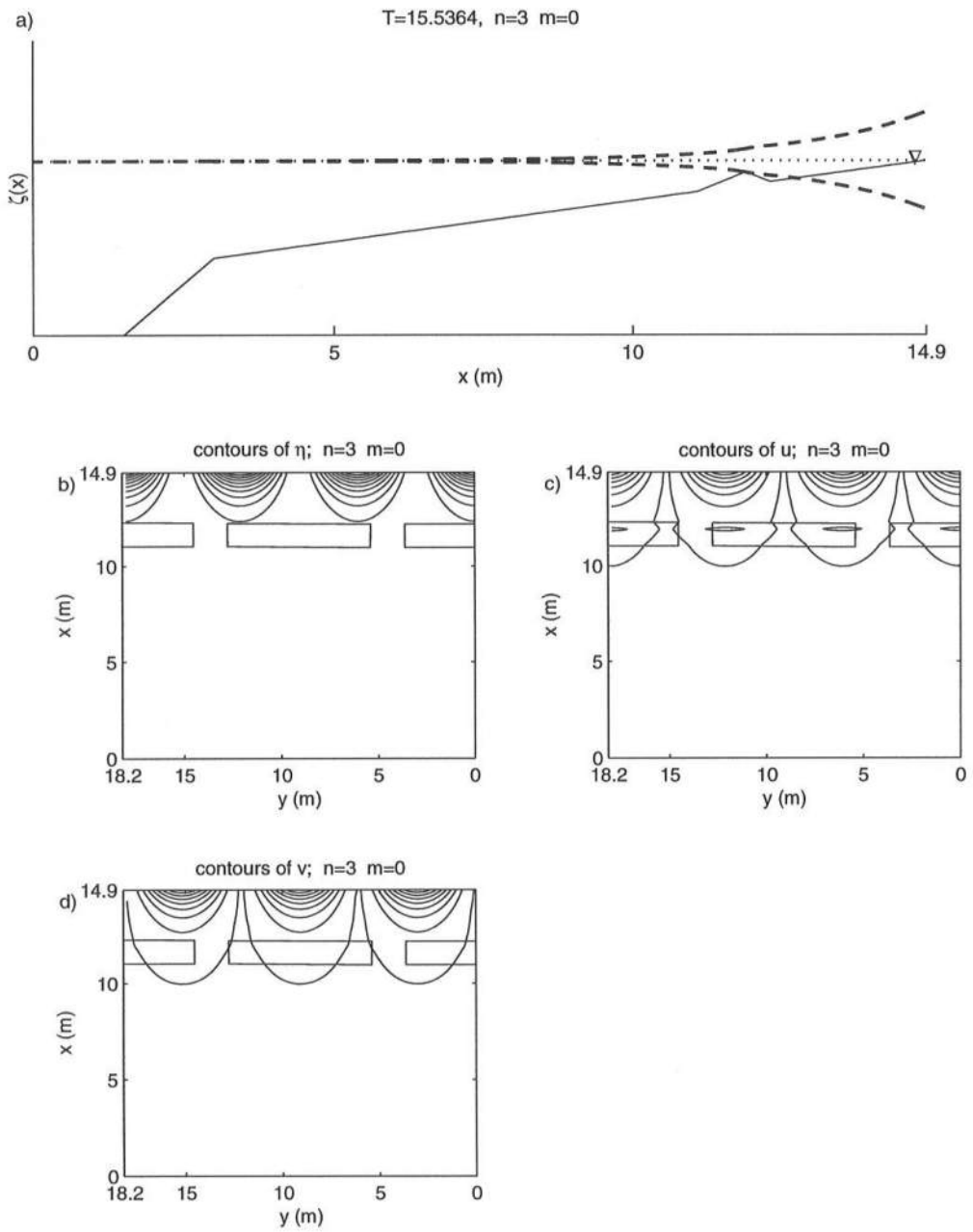

Figure 4.28: Calculated results of (a) cross-shore wave form $\zeta_0(\mathrm{x})$ (b) normalized variance of η (c) normalized variance of u and (d) normalized variance of v for T=15.5 s, Test B.

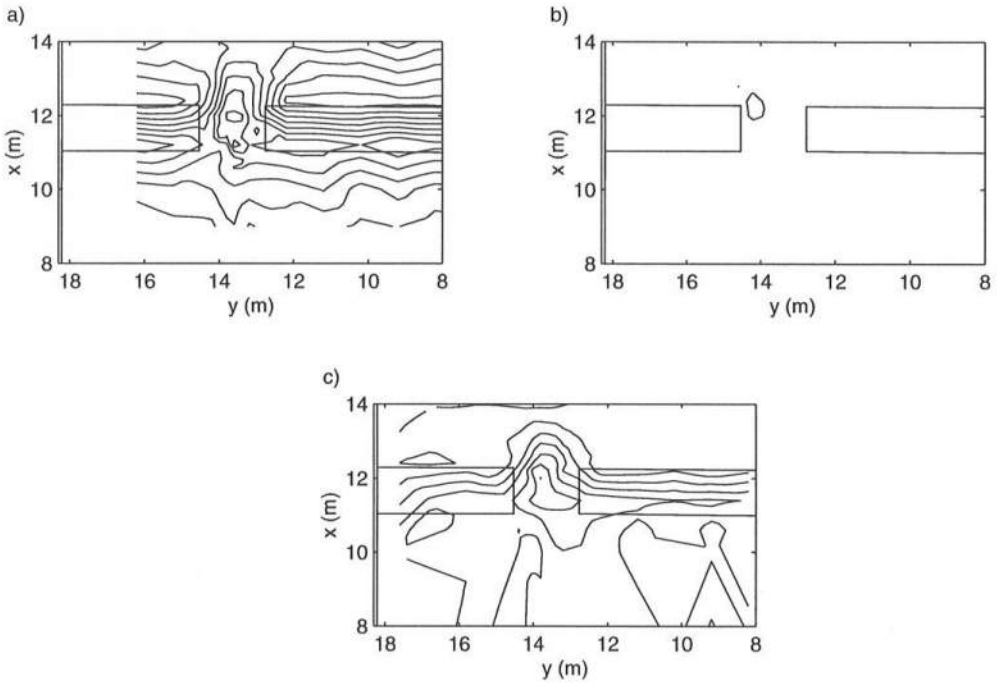

Figure 4.29: Contours of variance in the incident frequency band (0.75<f<5 Hz) for Test B (*a*) normalized cross-shore velocity, (*b*) normalized longshore velocity, and (*c*) measured water surface elevation. Contour interval for velocities is 0.1 (nondimensional), for water surface is 0.5 cm^2.

was computed. In addition, for each frequency band, the velocity variances were normalized by the maximum measured u variance in the same band, so that the relative magnitude of longshore variance to cross-shore variance could be compared.

Figure 4.29 gives a good description of the transformation of the incident waves. The cross-shore variance shows the decrease in amplitude of the waves as they break on the bar and the ridge of energy due to wave steepening in the channel. In addition, there is a small region of longshore variance near the channel due to the wave refraction/diffraction through the rip channel. Figure 4.30 shows a wider distribution of velocity variance for this mid-frequency band. The concentration of variances near the shoreline and near the bar crest suggest that seiche modes were present, however, the consistent concentration of low frequency variance in the rip

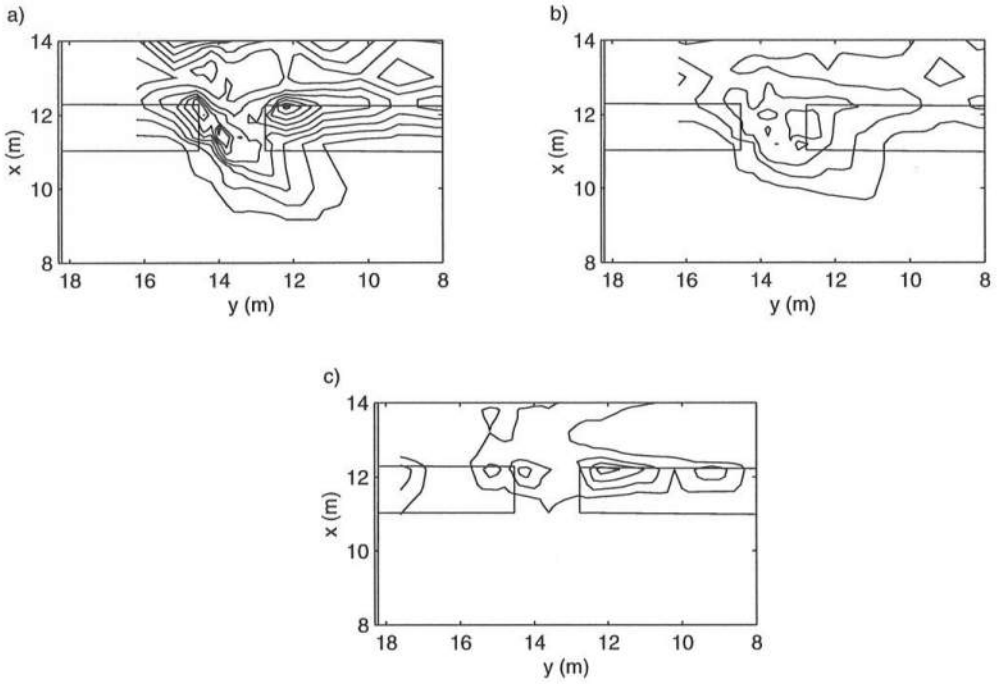

Figure 4.30: Contours of variance in the mid-frequency band (0.01<f<0.75 Hz) for Test B (*a*) normalized cross-shore velocity, (*b*) normalized longshore velocity, and (*c*) measured water surface elevation. Contour interval for velocities is 0.1 (nondimensional), for water surface is 0.0025 cm^2.

channel indicates that there is a significant local source of low frequency variance near the channel.

The lowest frequency band shown in Figure 4.31 contains motions much slower than any seiching mode. The concentration in variances in the rip channel is in agreement with the previous finding that these relatively slow motions are related to the rip migration in Test B.

4.5 Summary

In this chapter we described the existence of low frequency motions during the experiments. The denser sets of measurements made during Tests B and C and the few runs of extra long duration allowed us to analyze the characteristics of the

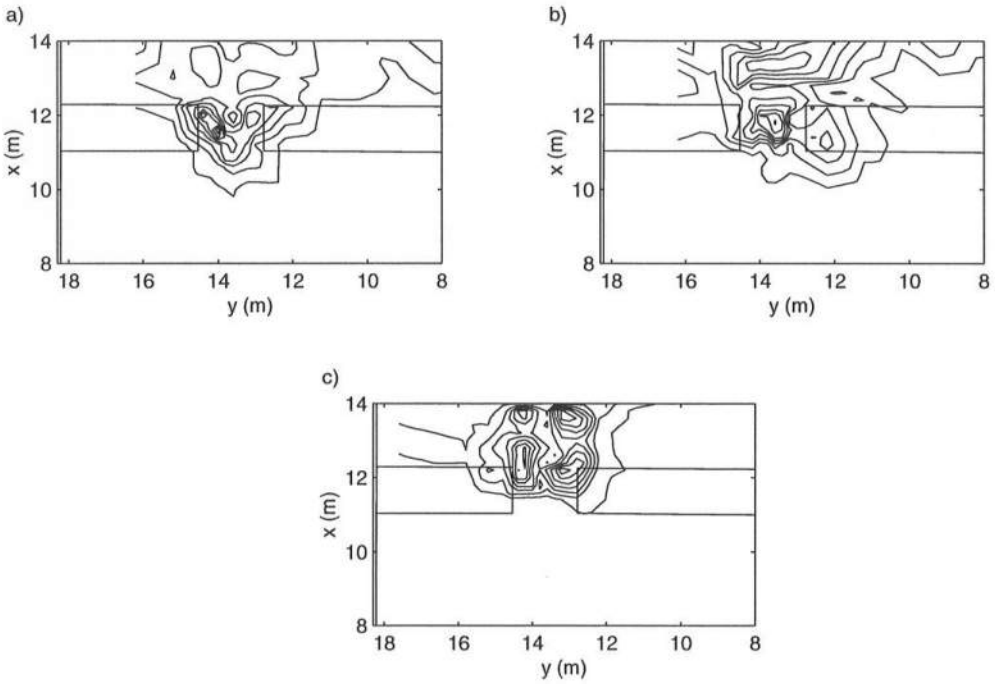

Figure 4.31: Contours of variance in the low frequency band (0<f<0.01 Hz) for Test B (*a*) normalized cross-shore velocity, (*b*) normalized longshore velocity, and (*c*) measured water surface elevation. Contour interval for velocities is 0.1 (nondimensional), for water surface is 0.0025 cm^2.

low frequency motions in detail for these tests. During Test B the rip current was shown to have a dominant oscillation involving a migration from side to side in the channel with a period of approximately 200 seconds, associated with this migration a fluctuation in the cross-channel water surface gradient was observed. Also during Test B, a higher frequency oscillation was, at times, observed near the exit of the rip channel which was directly associated with the simultaneous presence of a strong rip current. The intermittent character of the rip current measured at the rip channel exit is attributed to the large scale migration of the entire rip current.

Test C had a lower still water level than Test B and a slightly higher wave height. During this test the rip current was much less intermittent, suggesting the rip current remained in the rip channel during most of the experiment. There

was, however, some evidence from measurements made at the far sides of the rip channel, that the rip current was migrating to a limited extent. Energy spectra of the cross-shore and longshore currents during Test C suggest the presence of two dominant modes of low frequency energy along with energy at the sum of the dominant frequencies, and at a higher harmonic, implying that the two modes may be interacting nonlinearly. Evidence of low frequency motion was also found to varying degrees in Tests D-G. Tests D, F, and G also suggest that the dominant low frequency mode(s) may be interacting with each other (or itself).

In order to quantify the effects of basin seiching on the experiments, a numerical calculation of the shallow water seiche modes was performed. The five lowest frequency seiche modes for the three water depths used in the experiments were calculated and shown to be at higher frequencies than most of the observed low frequency motions. Analysis of the measured variances during Test B showed some evidence that seiching was present during the experiments; however, there was a significant concentration in variance near the rip channel that was unrelated to basin seiching.

Chapter 5

RIP CURRENT MODELING

In this chapter we investigate whether some or all of the unsteady rip current motions observed during the experiments can be explained by an instability mechanism. The characteristics of the rip currents generated in these experiments are similar to shallow water jets flowing into quiescent waters. Fluid jets have been studied extensively by hydrodynamicists for much of this century (e.g. Schlichting, 1933; Bickley, 1939) and a well known phenomena associated with these jets is their tendency towards hydrodynamic instability. Therefore we employ classical methods to model the experimental jets in order to determine if instability theory can describe the observed low frequency motions.

First, we derive the governing vorticity equation for the time-averaged rip current flow and then formulate an instability equation as a perturbation to the time-averaged equation. We seek instabilities as solutions that grow in time or space from an initial (small) perturbation. Neglecting viscous and nonparallel effects allows the instability equation to be reduced to the well-known Rayleigh stability equation. Previously known solutions to this equation for temporally growing modes arising from simplified velocity profiles are reviewed and the results are utilized to estimate the basic time and space scales associated with jet instabilities.

Next, we will formulate a set of self-similar solutions for the time-averaged flow in nearshore jets, including viscous and nonparallel effects. Using the method of multiple scales, the viscous and nonparallel effects of the steady flow are introduced

as a correction to the Rayleigh stability equation. The Rayleigh equation is solved for spatially growing disturbances and the correction terms then allow us to calculate the axial variations in the disturbance amplitude, wavenumber, and growth rate.

Finally, the self-similar jet solutions are compared to the experimental data and their stability characteristics examined. The results suggest that the time-averaged rip current flow is reasonably well described by the self-similar jet profiles. The jet profile is shown to be highly unstable and the predicted time and spatial scales compare well with the experimental data.

5.1 Governing equations

In order to model the rip current, we begin with the wave- and depth-averaged equations of motion.

$$\hat{u}_t^* + \hat{u}^*\hat{u}_x^* + \hat{v}^*\hat{u}_y^* = -g\hat{\eta}_x^* + \hat{R}_x^* + \hat{M}_x^* + \hat{\tau}_x^* \tag{5.1}$$

$$\hat{v}_t^* + \hat{u}^*\hat{v}_x^* + \hat{v}^*\hat{v}_y^* = -g\hat{\eta}_y^* + \hat{R}_y^* + \hat{M}_y^* + \hat{\tau}_y^* \tag{5.2}$$

$$(\hat{u}^*\hat{h}^*)_x + (\hat{v}^*\hat{h}^*)_y = -\hat{\eta}_t^*, \tag{5.3}$$

where $\hat{u}^*, \hat{v}^*, \hat{\eta}^*$, and $\hat{h}^*$ represent the dimensional cross-shore and longshore velocity, water suface elevation, and total water depth (including setdown/setup), respectively, and the subscripts indicate derivatives in x, y, and t. The forcing due to radiation stress gradients, $\hat{R}_{x,y}^*$ (where the subscripts indicate direction in which they act), are defined dimensionally as

$$\begin{aligned} \hat{R}_x^* &= -\frac{1}{\rho h}\left(\frac{\partial}{\partial x}\hat{S}_{xx}^* + \frac{\partial}{\partial y}\hat{S}_{yx}^*\right) \\ \hat{R}_y^* &= -\frac{1}{\rho h}\left(\frac{\partial}{\partial x}\hat{S}_{xy}^* + \frac{\partial}{\partial y}\hat{S}_{yy}^*\right), \end{aligned} \tag{5.4}$$

where $\hat{S}^*_{i,j}$ are the components of the traditional radiation stress tensor. The turbulent mixing terms, $\hat{M}^*_{x,y}$, are defined dimensionally as

$$\begin{aligned} \hat{M}^*_x &= -\frac{1}{\rho h}\left(\frac{\partial}{\partial x}\hat{F}^*_{xx} + \frac{\partial}{\partial y}\hat{F}^*_{yx}\right) \\ \hat{M}^*_y &= -\frac{1}{\rho h}\left(\frac{\partial}{\partial x}\hat{F}^*_{xy} + \frac{\partial}{\partial y}\hat{F}^*_{yy}\right), \end{aligned} \tag{5.5}$$

where $\hat{F}^*_{i,j}$ are the components of the Reynolds stress tensor. Finally, $\hat{\tau}^*_{x,y}$ represent the bottom friction components.

In order to proceed we will need to make certain simplifications. We will make the classical "rigid-lid" approximation, $\hat{\eta}^*_t \approx 0$, and also assume a longshore uniform coast ($\hat{h}^* = \hat{h}^*(x)$). The first approximation is commonly used in the study of nearshore vorticity motions, and the second is a reasonable starting point for the analysis of rip current dynamics and is not strictly violated within the rip current while it remains in the rip channel. This also implies that $\hat{\eta}^*_y \approx 0$.

Next we will assume that in the x direction the radiation stress forcing is balanced by the water surface gradient such that

$$g\hat{\eta}^*_x = \hat{R}^*_x. \tag{5.6}$$

Additionally we will neglect the radiation stress forcing in the y direction, $\hat{R}^*_y$. It is important to note that we are not directly modeling the forcing of the rip current itself. Instead, we consider the rip as being an ambient current within our domain. Therefore, by neglecting $\hat{R}^*_y$ we are neglecting the effects of wave refraction due to the opposing current. We do this so that we can obtain a reasonably simplified analytic solution, which allows us to isolate the basic physical mechanisms governing the rip dynamics.

Utilizing the above assumptions we cross-differentiate Eqs.5.1-5.2 and combine with Eq. 5.3 to obtain the dimensional, vorticity transport equation for a longshore uniform coast

$$\frac{D}{Dt}\left(\frac{\hat{u}_y^* - \hat{v}_x^*}{\hat{h}^*}\right) = -\frac{1}{\hat{h}^*}\nabla \times (\hat{M}^* + \hat{\tau}^*), \tag{5.7}$$

where the horizontal gradient operator is defined such that $\nabla \times \hat{M}^* = \frac{\partial}{\partial x}\hat{M}_y^* - \frac{\partial}{\partial y}\hat{M}_x^*$.

In order to non-dimensionalize the above equation, we introduce the basic scales

$$\begin{array}{lll} \hat{u}^*, \hat{v}^* \sim U_0 & \hat{h}^* \sim h_0 & \hat{M}^* \sim U_0^2/b_0 \\ x, y \sim b_0 & t \sim b_0/U_0 & \hat{\tau}^* \sim U_0^2/h_0, \end{array}$$

where U_0 is a velocity scale, b_0 is a length scale, and h_0 is a depth scale. Substitution of the scales leads us to the following non-dimensional vorticity transport equation:

$$\frac{D}{Dt}\left(\frac{\hat{u}_y - \hat{v}_x}{\hat{h}}\right) = -\frac{1}{\hat{h}}\nabla \times \hat{M} + \frac{b_0}{h_0}\left(-\frac{1}{\hat{h}}\nabla \times \hat{\tau}\right), \tag{5.8}$$

(x, y, t are now non-dimensional also). We next assume our basic state is a steady mean flow with superimposed small disturbances such that

$$\begin{aligned} \hat{u}(x,y,t) &= U(x,y) + u(x,y,t) \\ \hat{v}(x,y,t) &= V(x,y) + v(x,y,t) \\ \hat{M}(x,y,t) &= M^0(x,y) + \Delta M(x,y,t) \\ \hat{\tau}(x,y,t) &= \tau^0(x,y) + \Delta\tau(x,y,t) \end{aligned} \tag{5.9}$$

where U, V represent the steady mean flow, u, v are the disturbance velocities, and M^0 and τ^0 represent the turbulent mixing and bottom stress in the absence of disturbances.

Equation 5.8, in the absence of disturbances (i.e. $u = v = 0$), can now be written as

$$U\left(\frac{U_y - V_x}{h}\right)_x + V\left(\frac{U_y - V_x}{h}\right)_y = -\frac{1}{h}\nabla \times M^0 + \frac{b_0}{h_0}\left(-\frac{1}{h}\nabla \times \tau^0\right), \tag{5.10}$$

where $h = \hat{h}$ (nondimensional water depth). This equation represents the governing nondimensional vorticity transport equation for steady flow.

Subtracting Eq. 5.10 from Eq. 5.8 and linearizing in the disturbance velocities, we obtain

$$\left(\frac{\partial}{\partial t} + U\frac{\partial}{\partial x} + V\frac{\partial}{\partial y}\right)\left(\frac{u_y - v_x}{h}\right) + \left(u\frac{\partial}{\partial x} + v\frac{\partial}{\partial y}\right)\left(\frac{U_y - V_x}{h}\right) =$$

$$-\frac{1}{h}\nabla\times\Delta M + \frac{b_0}{h_0}\left[-\frac{1}{h}\nabla\times\Delta\tau\right], \tag{5.11}$$

which represents the governing nondimensional vorticity transport equation for the disturbed flow. Next we will examine solutions to these equations by first specifying the form of the steady flow and then searching for growing solutions (instabilities) to the disturbance equation.

5.2 Inviscid, flat bottom jets

As the simplest case we consider an unbounded, inviscid parallel flow where $U = U(y)$, $V = 0$, and $h = h_0$. For this case Eq. 5.10 allows an arbitrary variation in the velocity profile $U(y)$; however, an inflexion point ($U_{yy} = 0$) is required for instability according to Rayleigh's inflexion point theorem. Utilizing Eq. 5.3 we can introduce a stream function $\psi(x, y, t)$ for the disturbances, such that

$$\begin{aligned} \psi_y &= uh \\ -\psi_x &= vh. \end{aligned} \tag{5.12}$$

We then consider a normal-mode analysis of Eq. 5.11 and assume a harmonic dependence on x and t, so the stream function takes the form

$$\psi(x, y, t) = \phi(y)e^{i(kx-\omega t)}, \tag{5.13}$$

and the eigenfunction ϕ contains the transverse structure of the instability. Substituting Eq. 5.13 into the inviscid and parallel flow version of Eq. 5.11 leads us to the Rayleigh stability equation:

$$(U - c)(\phi_{yy} - k^2\phi) - U_{yy}\phi = 0. \tag{5.14}$$

where $c \equiv \omega/k$.

At this point there are two ways to approach the instability eigenvalue problem. The first approach is to seek unstable modes that grow in time from disturbances at a given wavenumber. This temporal instability approach assumes that the wavenumber, k, is real and the eigenvalue, ω, is in general complex with the real part, ω_r, being the physical frequency and the imaginary part, ω_i, being the growth rate. From inspection of Eq. 5.13 it is evident that a given mode is linearly unstable if $\omega_i > 0$, since the mode will then grow in time. Of course, in practice, neglected nonlinear effects will restrict growth at some finite value.

The second approach seeks unstable modes that grow spatially with propagation distance from an initial disturbance at a given frequency. Conversely, the spatial instability approach presumes ω to be purely real and the eigenvalue k is, in general, complex with k_r representing the physical wavenumber and k_i the growth rate. A given mode is linearly unstable when $k_i < 0$ and will grow as it propagates downstream with the mean current U.

It appears logical that the spatial theory would be a better representation of the physical experiments previously described, since the disturbances must be initiated locally at the upstream end of the current, and grow downstream. Also, the temporal theory assumes an initial disturbance that is uniform in the cross-shore direction, which seems less relevant here since the mean flow is spatially varying in the cross-shore direction. However, the temporal theory has been applied to jets by e.g. Ling and Reynolds (1973) and Drazin and Howard (1966), with varying degrees of success. Perhaps the strongest reason for using the temporal theory is that it is

almost always more mathematically tractable than the spatial theory. In addition, the work of Gaster (1962) has shown that the eigenvalues from the temporal theory can be related to those of the spatial theory for instabilities with small growth rates. Furthermore, Reed *et al.* (1996) has shown that Gaster's relations can be applied to instabilities with moderately large growth rates also.

Initially we will proceed by reviewing previous solutions for instabilities to simplified jet velocity profiles that utilize the temporal theory, since they represent the simplest first approach. In a later section we will develop a model for the jet velocity profile that compares favorably to the rip current measurements and we will analyze the spatial stability characteristics of the rip current profile.

5.2.1 Top-hat jet

The simplest possible jet profile is the "top-hat" jet given by $U = 1$ for $|y| < 1$ and $U = 0$ for $|y| > 1$ and studied previously by Rayleigh (1894, pp.380-381). Since the velocity profile is piecewise linear (i.e. $U_{yy} = 0$), Eq. 5.14 can be further simplified. Solutions take the form of exponential or hyperbolic functions and the solutions within the flow and outside are matched across the interface by requiring continuity of pressure and of the normal velocity across the flow discontinuities (see Drazin and Reid, 1981, pp.144-145). The final solutions then fall into two categories, *sinuous* or *varicose*, depending on whether ψ is an even or odd function of y (i.e. $\psi_y(0) = 0$ or $\psi(0) = 0$), respectively.

The final solution is given by the following eigenvalue relations:

$$\text{sinuous mode:} \qquad c^2 + (1-c)^2 \tanh k = 0$$

$$\text{varicose mode:} \qquad c^2 + (1-c)^2 \coth k = 0,$$

where k is presumed to be positive and real, and $c = \omega/k$ is the complex phase speed. Figure 5.1a shows the growth rate as a function of wavenumber for both the sinuous and varicose modes. The figure indicates that for this simplified jet profile the flow is unstable at all wavenumbers and the growth rate increase linearly

with wavenumber for all modes. Figure 5.1b shows the dispersion relation for both the sinuous and varicose modes. The dispersion relations are approximately linear except at small wavenumbers. It is interesting to note that at low wavenumbers the varicose modes travel much faster than the sinuous modes (see Fig.5.1c). At higher wavenumbers the phase speeds for all modes converge to a value of 50% of the jet velocity.

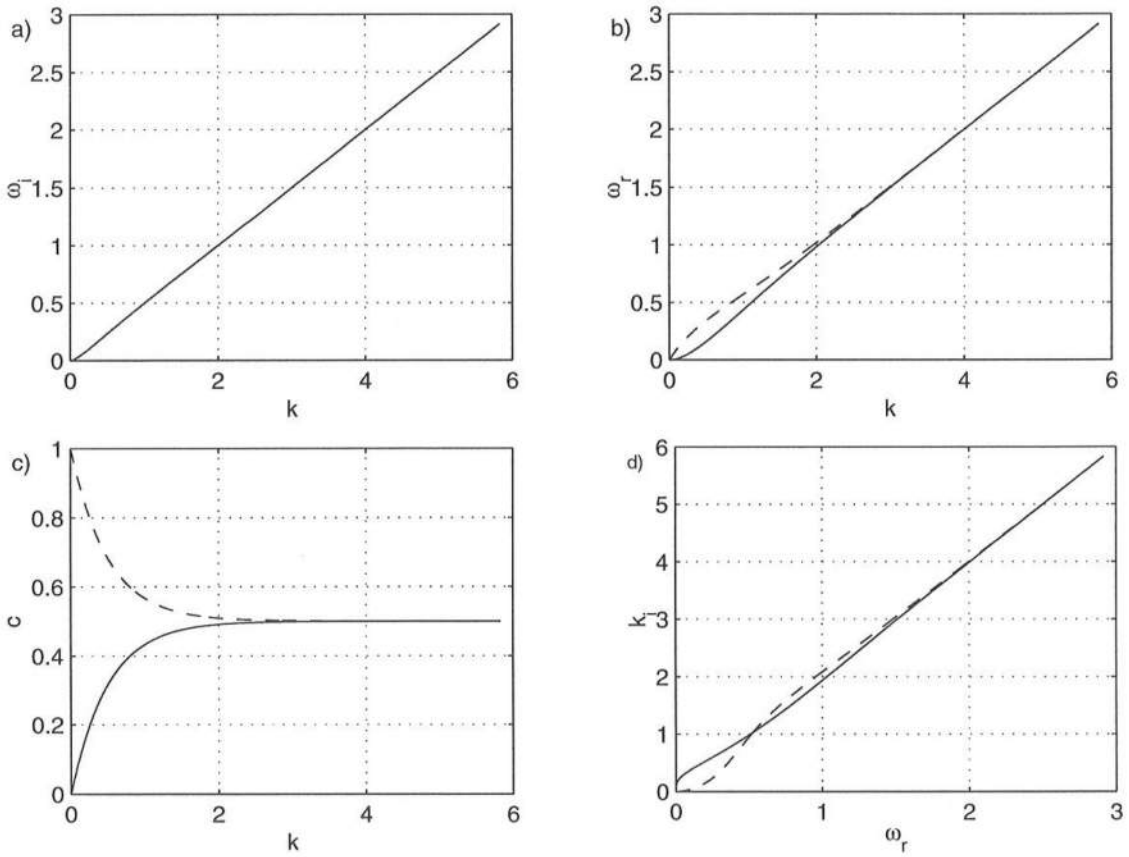

Figure 5.1: (*a*) Growth rate vs. wavenumber (*b*) frequency vs. wavenumber (*c*) phase speed vs. wavenumber for the top-hat jet temporal instability theory; (*d*) spatial growth rate vs. frequency (sinuous modes - solid line, varicose modes - dashed line). All variables are nondimensional.

Using Gaster's relations we may relate these stability results from the temporal theory to those for spatially growing disturbances. Gaster's relations are given

by the following:

$$\frac{\partial \omega_r}{\partial k_r} = -\frac{\omega_i}{k_i}, \tag{5.15}$$

and

$$\begin{aligned} \omega_r(\text{spatial}) &= \omega_r(\text{temporal}) \\ k_r(\text{spatial}) &= k_r(\text{temporal}). \end{aligned} \tag{5.16}$$

These relations apply as long as growth rates are small, in some sense, and no singularities exist in the region of complex $\omega - k$ space of interest. Using Eqs. 5.15-5.16 we can calculate the spatial growth rate k_i from the temporal results. The spatial growth rates for the top-hat jet calculated from these relations are shown in Figure 5.1d for all modes. The spatial stability results are similar to those from the temporal theory as both modes are unstable at all wavenumbers and growth rates increase approximately linearly with frequency. There are, however, specific ranges of frequencies where the varicose modes are slightly more unstable then the sinuous modes and vice versa for the spatially growing disturbances.

5.2.2 Triangle jet

A better approximation to the jet profile is the triangle jet given by $U(y) = 1 - |y|$ for $|y| < 1$ and $U(y) = 0$ for $|y| > 1$. By a similar solution method as the top-hat jet, the eigenvalue relations for this profile are found to be (Drazin and Reid, 1981, p.246; Rayleigh, 1894, p.395)

$$\begin{aligned} &\text{sinuous mode:} && 2k^2c^2 + kc(1 - 2k - e^{-2k}) - [1 - k - (1 + k)e^{-2k}] = 0 \\ &\text{varicose mode:} && c - \frac{1}{2k}(1 - e^{-2k}) = 0. \end{aligned}$$

It is evident from the second relation, since k is real, that the varicose modes are always neutrally stable (i.e. $\omega_i = 0$) for this jet. The sinuous modes, however, are unstable for a range of k values.

The temporal growth rates as a function of wavenumber for the triangle jet are shown in Figure 5.2a. The figure shows that this jet is unstable for $k < 1.83$. The dispersion relation for the sinuous modes is shown in Figure 5.2b and it is nearly linear except at small wavenumbers. Also, in contrast to the top-hat jet, the phase speed of the fastest growing temporal mode ($k = 1.23$) is only approximately 31% of the maximum current speed.

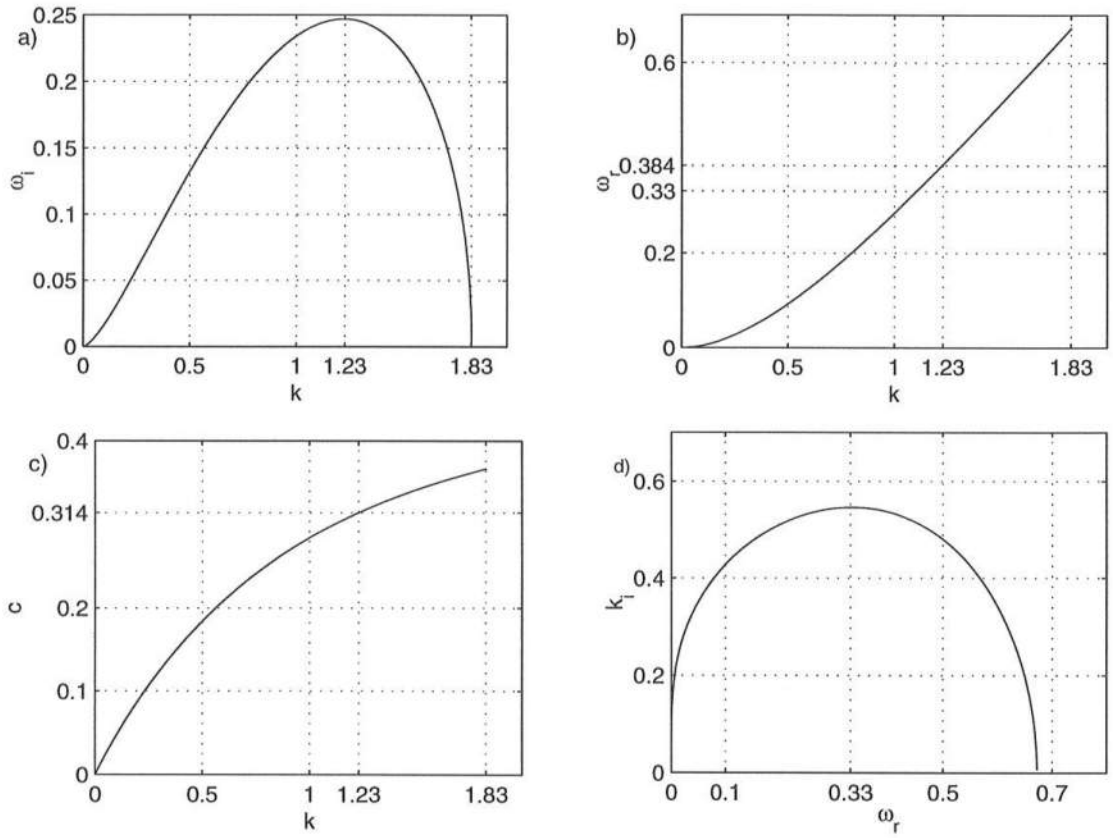

Figure 5.2: (*a*) Growth rate vs. wavenumber (*b*) frequency vs. wavenumber (*c*) phase speed vs. wavenumber for the triangle jet temporal instability theory; (*d*) spatial growth rate vs. frequency (sinuous modes only). All variables are nondimensional.

The spatial growth rates calculated using Eqs. 5.15-5.16 are shown in Figure 5.2d. It is interesting to note that the fastest growing spatial mode is at slightly

lower frequency ($\omega_r = 0.33$) and wavenumber ($k = 1.11$) then the fastest growing temporal mode.

The experimental results shown in Chapter 3 (see Figure 3.13) indicate that the use of piecewise linear velocity profiles is, at best, a rough approximation of the measured experimental conditions. However, these profiles allow us to make analytic estimates of the time and space scales of jet instabilities. A simple comparison based on the results from the triangle jet indicates that a jet with a maximum current of 30 cm/s and half-width of 100 cm (see Test C) would have a fastest growing spatial mode with period ~63 s and wavelength ~570 cm. These scales (especially the time scale) appear to be in the right range for many of the low frequency motions observed during the experiment (note: we will discuss experimental estimates of instability length scales in a later section). This suggests that the jet instability mechanism may be useful in describing at least some of the low frequency rip current motions. In the next section we will describe a more realistic model for the time-averaged rip current flow and examine the stability characteristics of viscous jet flows in the presence of depth variations and bottom friction.

5.3 Viscous turbulent jets

5.3.1 Rip current mean flows

Previous researchers have used simplified forms of Eq. 5.10 to model the mean flows in rip currents. For example, Arthur (1950) developed an analytic model that satisfied the inviscid form of Eq. 5.10 and matched the general characteristics of a rip current quite well. His model produced an initially long and narrow rip, supplied by nearshore feeder currents, which decayed in magnitude and spread laterally as it extended offshore. However, the rip current spreading was given by an empirical formulation without justification, and viscous effects were not considered. Tam (1973) determined a similarity solution to the rip current flow in a transformed coordinate system based on a boundary layer analogy and investigated the dynamics of the

steady flow in the absence of bottom friction. We will use a similar approach here, however, our approach is simpler as our coordinate system is more straightforward. Also, we will include the effects of bottom friction, and further analyze the stability characteristics of the rip current. Our approach to the steady flow problem will most resemble the approach of Joshi (1982), who analyzed the hydromechanics of tidal jets. In contrast to Joshi, we will approach the problem in terms of the nearshore vorticity balance and we will present a simplified relationship for determining the empirical mixing and bottom friction coefficients from the experimental data.

In order to proceed in the analysis of Eq. 5.10 we will restrict ourselves to flows which are slightly nonparallel such that they are slowly varying in the cross-shore direction. Therefore we introduce a scaled cross-shore coordinate x_1 such that

$$x_1 = \epsilon x, \tag{5.17}$$

where ϵ is a small dimensionless parameter that represents the slow variation of the flow. Thus the steady flow components are given by

$$U = U(x_1, y) \tag{5.18}$$

$$V = \epsilon V(x_1, y), \tag{5.19}$$

and the cross-shore derivative transforms as

$$\frac{\partial}{\partial x} = \epsilon \frac{\partial}{\partial x_1}. \tag{5.20}$$

After substituting in the scaled coordinate, the left-hand side of Eq. 5.10 becomes

$$L.H.S. = \epsilon U \left(\frac{U_y - \epsilon^2 V_{x_1}}{h} \right)_{x_1} + \epsilon V \left(\frac{U_y - \epsilon^2 V_{x_1}}{h} \right)_y. \tag{5.21}$$

Next we need to parameterize the turbulent mixing and bottom friction terms. It is common to neglect the normal Reynolds stress terms ($\hat{F}^*_{xx}$, $\hat{F}^*_{yy}$) since

they are generally small. We will parameterize the remaining terms utilizing Prandtl's mixing length hypothesis and a turbulent eddy viscosity, ν_T, such that the nondimensional turbulent mixing takes the following forms

$$\begin{aligned} \hat{M}_x &= \frac{1}{\hat{h}}\frac{\partial}{\partial y}(\hat{h}\,\hat{\nu}_T\,\hat{u}_y) \\ \hat{M}_y &= \frac{1}{\hat{h}}\frac{\partial}{\partial x}(\hat{h}\,\hat{\nu}_T\,\hat{u}_y). \end{aligned} \tag{5.22}$$

After introducing the scaled coordinate, the mixing in the absence of disturbances takes the forms

$$\begin{aligned} M^0_{x_1} &= \frac{1}{R_t}\frac{\partial}{\partial y}(U_m \ell\, U_y) \\ M^0_y &= \frac{\epsilon}{R_t}\frac{1}{h}\frac{\partial}{\partial x_1}(h\,U_m \ell\, U_y), \end{aligned} \tag{5.23}$$

where R_t is a non-dimensional turbulent Reynolds number defined as $R_T \equiv U_m \ell/\nu_T$, ℓ is a mixing length, and U_m represents the velocity at the rip current centerline and varies in the cross-shore direction.

For the bottom friction we will utilize the following nonlinear formulations

$$\begin{aligned} \hat{\tau}_x &= -\frac{f_d}{8\hat{h}}\,\hat{u}\,|\hat{\vec{u}}| \\ \hat{\tau}_y &= -\frac{f_d}{8\hat{h}}\,\hat{v}\,|\hat{\vec{u}}|, \end{aligned} \tag{5.24}$$

where f_d is a Darcy-Weisbach friction factor. In the absence of disturbances, the scaled variables for the bottom friction terms become

$$\begin{aligned} \tau^0_{x_1} &= -\frac{f_d}{8\,h}U(U^2 + \epsilon^2\,V^2)^{1/2} \\ \tau^0_{y_1} &= -\frac{\epsilon\,f_d}{8\,h}V(U^2 + \epsilon^2\,V^2)^{1/2}. \end{aligned} \tag{5.25}$$

It is evident, since the terms in Eq. 5.21 are $O(\epsilon)$ or smaller, that the parameter $1/R_t$ in Eq. 5.23 must be at least as large as $O(\epsilon)$ in order to retain the effects of turbulent mixing on the time-averaged flow. Therefore we will retain $M^0_{x_1}$ and neglect the smaller term $M^0_{y_1}$. Likewise, we take the nondimensional frictional

parameter $f_t \equiv f_d b_0/8h_0$ to be $O(\epsilon)$ and therefore retain $\tau^0_{x_1}$ and neglect $\tau^0_{y_1}$. The governing equation for the time-averaged rip current flow can then be written as

$$UU_{yx_1} - UU_y\frac{h_{x_1}}{h} + VU_{yy} = \frac{1}{R_t}\left(U_m \ell\, U_{yyy}\right) - f_t\left(\frac{2UU_y}{h}\right). \tag{5.26}$$

We will treat the rip current as a self-preserving turbulent jet. The self-preservation of the jet implies that the evolution of the flow is governed by local scales of length and velocity (Tennekes and Lumley, 1972). We will take the local length scale to be $\ell = b(x_1)$, the half-width of the jet, and the velocity scale, U_m, to be the local velocity at the jet centerline. In addition, if the jet is self-preserving, the dimensionless velocity profiles U/U_m at all x_1 locations will be identical when plotted against the dimensionless coordinate y/b. Therefore we introduce a similarity variable

$$\eta = \frac{y}{b(x_1)} \tag{5.27}$$

and we assume that

$$\frac{U(x_1, y)}{U_m(x_1)} = f(\eta) \text{ only.} \tag{5.28}$$

Accordingly, the derivatives transform as

$$\begin{aligned} \frac{\partial}{\partial y} &= \frac{\partial \eta}{\partial y}\frac{\partial}{\partial \eta} = \frac{1}{b(x_1)}\frac{\partial}{\partial \eta} \\ \frac{\partial}{\partial x_1} &= \frac{\partial \eta}{\partial x_1}\frac{\partial}{\partial \eta} = -\eta\frac{b_{x_1}}{b}\frac{\partial}{\partial \eta} \end{aligned} \tag{5.29}$$

It is important to note here that y was previously non-dimensionalized by the constant b_0 which we have taken to be the jet width at the origin. The jet width $b(x_1)$ has also been non-dimensionalized by b_0, and therefore $b(0) = 1$. Similarily, the velocities have been non-dimensionalized by U_0 which we have taken to be the the maximum velocity at the origin, therefore $U_m(0) = 1$.

In order to write Eq. 5.26 in terms of similarity variables, we first need to obtain an expression for $V(x_1, \eta)$. We do this by integrating the non-dimensional form of the continuity equation (Eq. 5.3), using the condition of zero transverse flow at the jet centerline ($V(x_1, \eta = 0) = 0$), to obtain

$$V = U_m b_{x_1} \eta f - \left(U_{m_{x_1}} b + U_m \frac{h_{x_1}}{h} b + U_m b_{x_1} \right) \int_0^\eta f d\eta'. \tag{5.30}$$

For the mixing term we will assume self-preservation of the Reynolds stress such that we can express the mixing as

$$\frac{1}{R_t} U_m \, \ell \, U_y = U_m^2 \, g(\eta) \tag{5.31}$$

where $g(\eta)$ is an as yet unspecified similarity function.

Substitution of the similarity forms of the velocities and Reynolds stress into Eq. 5.26 and simplifying leads us to the following

$$\left(\frac{b \, U_{m_{x_1}}}{U_m} - b_{x_1} - \frac{b \, h_{x_1}}{h} + 2 \frac{f_t \, b}{h} \right) f f_\eta - \left(\frac{b \, U_{m_{x_1}}}{U_m} + \frac{b \, h_{x_1}}{h} + b_{x_1} \right) f_{\eta\eta} \int_0^\eta f d\eta' = g_{\eta\eta}, \tag{5.32}$$

where subscripts η and x_1 represent derivatives. Note that f and g do not depend explicitly on x_1, whereas the coefficients on the left-hand side of Eq. 5.32 are generally functions of x_1. Therefore, for this equation to hold throughout the region of study, the coefficients must be independent of x_1 and the following relations must hold

$$b \frac{U_{m_{x_1}}}{U_m} - b_{x_1} - b \frac{h_{x_1}}{h} + 2 f_t \frac{b}{h} = \text{constant} \tag{5.33}$$

$$b \frac{U_{m_{x_1}}}{U_m} + b \frac{h_{x_1}}{h} + b_{x_1} = \text{constant}. \tag{5.34}$$

If we alternately add and subtract these two relations we obtain the following equations governing the length and velocity scales

$$b_{x_1} + \left(\frac{h_{x_1}}{h} - \frac{f_t}{h} \right) b = C \tag{5.35}$$

$$U_{m_{x_1}} + \left(\frac{f_t}{h} - \frac{C_1}{b} \right) U_m = 0. \tag{5.36}$$

where C and C_1 are true constants. These equations can be solved by the method of variation of parameters (see e.g. Greenberg, 1988, pp.907-909) giving the following general solutions for the width and velocity scales of the jet

$$b(x_1) = \frac{1}{h(x_1)} e^{f_t \int_0^{x_1} h^{-1} d\xi} \left[1 + C \int_0^{x_1} h(\xi_1) e^{-f_t \int_0^{\xi_1} h^{-1} d\zeta} d\xi_1 \right] \tag{5.37}$$

$$U_m(x_1) = C_3 e^{-f_t \int_0^{x_1} h^{-1} d\xi_1} \left[1 + C \int_0^{x_1} h(\xi) e^{-f_t \int_0^{\xi_1} h^{-1} d\zeta} d\xi_1 \right]^{C_1/C}, \tag{5.38}$$

where the lower limit of integration has been chosen to be $x_1 = 0$, also the nondimensional depth at the origin has been specified as $h(0) = 1$; thus, C, C_1, and C_3 are the three constants we are left to evaluate.

The constants C and C_1 are not independent and can be related utilizing the x_1-momentum equation,

$$UU_{x_1} + VU_y = [U_m^2 g(\eta)] - f_t \frac{U^2}{h}, \tag{5.39}$$

which, if integrated across the jet and applying the boundary conditions

$$U(x_1, \pm\infty) = 0 \tag{5.40}$$

$$g(x_1, \pm\infty) = 0, \tag{5.41}$$

gives us the governing equation for the axial jet momentum flux,

$$\left(h\, U_m^2\, b\right)_{x_1} = -f_t\, {U_m}^2\, b. \tag{5.42}$$

This equation shows that the axial (x_1) jet momentum decays due to the retarding effect of bottom friction. This is in contrast to the classical jet solution (flat bottom, $f_t = 0$), which conserves jet momentum flux in the axial direction. Substituting Eqs. 5.35-5.36 into Eq. 5.42 and rearranging yields the following relation

$$\frac{C}{C_1} = -2, \tag{5.43}$$

and evaluating Eq. 5.36 at $x_1 = 0$ yields $C_3 = 1$. Finally, we are left evaluating either C or C_1 experimentally. We do this by evaluating Eq. 5.36 at $x_1 = 0$ (where $h = h_0 = 1$), this gives the following relation

$$C = -2\left(U_{m_{x_1}}(0) + f_t\right), \tag{5.44}$$

which can be evaluated using the measured data.

We still have not yet specified $f(\eta)$ and $g(\eta)$. We can relate these two functions by returning to Eq. 5.31 and substituting $\ell = b$ and $U_y = U_m f_\eta / b$ to obtain

$$g = \frac{f_\eta}{R_t}. \tag{5.45}$$

Substituting the above relation into Eq. 5.32 gives us the general equation for f as

$$f_{3\eta} + \frac{3}{2} R_t C f f_\eta + \frac{C}{2} R_t f_{\eta\eta} \int_0^\eta f d\eta' = 0. \tag{5.46}$$

It can be verified by direct substitution that the solution to Eq. 5.46, subject to the boundary conditions $f(0) = 1$ and $f_\eta(0) = 0$, is

$$f = \operatorname{sech}^2\left(\frac{\sqrt{CR_t}}{2}\eta\right). \tag{5.47}$$

As the last consideration, we formally define the width scale $b(x_1)$ in relation to the velocity profile as

$$\frac{U(x_1, b)}{U_m(x_1)} = \operatorname{sech}^2(1) \approx 0.42, \tag{5.48}$$

so that b is defined as the distance from the jet axis where the axial velocity equals approximately 42% of the centerline velocity. By combining Eqs. 5.47-5.48, we can relate the turbulent Reynolds number to the experimental parameter C

$$R_t = \frac{4}{C}, \tag{5.49}$$

and the similarity function can be written simply as $f = \operatorname{sech}^2\eta$.

5.3.2 Rip current profiles on simplified topographies

The rip current model derived in the previous section allows an arbitrary depth variation in the cross-shore direction; however, it is interesting to examine the solutions on certain simplified topographies. The equations for the width scale and centerline velocity (Eqs. 5.37-5.38) reduce to the following equations for a constant bottom and a planar beach,

1. Flat bottom $\rightarrow h = 1$

   (a) without friction $\rightarrow f_t = 0$

$$b(x_1) = 1 + Cx_1 \tag{5.50}$$

$$U_m = (1 + Cx_1)^{-1/2} \tag{5.51}$$

   (b) with friction $\rightarrow f_t \neq 0$

$$b(x_1) = \left(1 + \frac{C}{f_t}\right) e^{f_t x_1} - \frac{C}{f_t} \tag{5.52}$$

$$U_m = e^{-f_t x_1} \left[1 + \frac{C}{f_t} - \frac{C}{f_t} e^{-f_t x_1}\right]^{-1/2} \tag{5.53}$$

2. Planar beach $\rightarrow h_x = \epsilon \cdot m_1$

   (a) without friction $\rightarrow f_t = 0$

$$b(x_1) = \frac{1}{h} + Cx_1 \left(1 - \frac{m_1 x_1}{2h}\right) \tag{5.54}$$

$$U_m = \left[1 + Cx_1(1 + \frac{m_1 x_1}{2})\right]^{-1/2} \tag{5.55}$$

   (b) with friction $\rightarrow f_t \neq 0$

$$b(x_1) = \left[1 - \frac{C}{2m_1 - f_t}\right] h^{\frac{f_t}{m_1} - 1} + \frac{Ch}{2m_1 - f_t} \tag{5.56}$$

$$U_m = h^{-\frac{f_t}{m_1}} \left[1 + \frac{C}{2m_1 - f_t} \left(h^{-\frac{f_t}{m_1} + 2} - 1\right)\right]^{-1/2} \tag{5.57}$$

It is evident that for a frictionless, flat bottom, the equations collapse to the classical plane jet solution whereby the width scale grows linearly along the jet axis and the centerline velocity decays with $x^{-1/2}$. Figure 5.3 shows the variation of the width scale and the centerline velocity in the offshore direction for specific parameter values. It can be seen from the figure that friction increases the jet spreading and causes the centerline velocity to decay more rapidly. In contrast, the jet spreading is reduced by increasing depth in the offshore direction due to vortex stretching (Arthur, 1962). In addition, if the frictional spreading effects are balanced by the narrowing due to vortex stretching ($f_t = m_1$), then the jet spreads linearly at the same rate as the classical plane jet. Similar results were found by Joshi (1982).

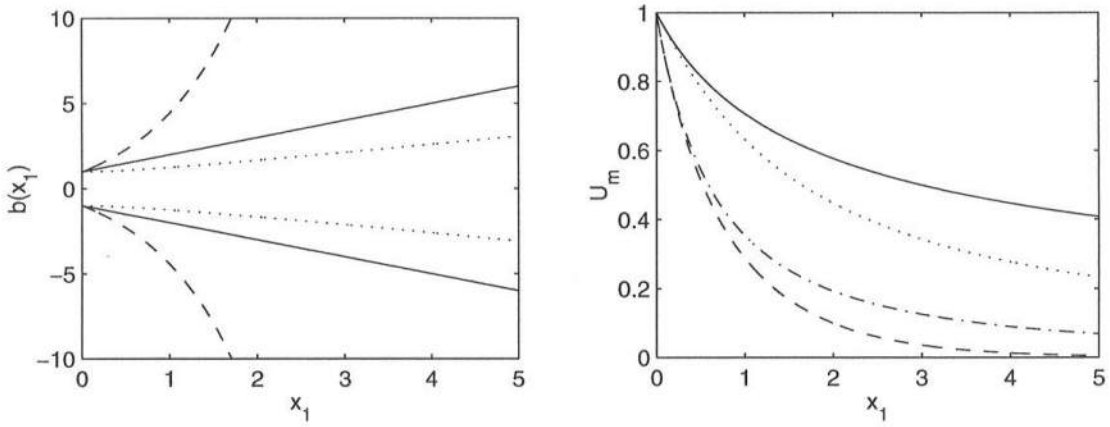

Figure 5.3: Cross-shore variation of the rip current scales (a) jet width vs. cross-shore distance (b) centerline velocity vs. cross-shore distance for classical plane jet (solid), flat bottom w/friction ($f_t = 1$) (dashed), planar beach ($m_1 = 1, f_t = 0$) (dotted), frictional planar beach ($m_1 = f_t = 1$) (dash-dot) (dash-dot is on top of solid line in (a)).

5.3.3 Stability equations for viscous turbulent jets

In the following section we will derive a linear stability model for the viscous turbulent jet formulated in the previous section. Returning to the governing

equation for the disturbed flow (Eq. 5.11) and substituting the mixing parameterization (Eq. 5.23) we have the following expressions for the mixing in the presence of disturbances:

$$\begin{aligned} \Delta M_x &= \frac{1}{R_t}\frac{\partial}{\partial y}(U_m\, b\, u_y) \\ \Delta M_y &= \frac{1}{hR_t}\frac{\partial}{\partial x}(h\, U_m\, b\, u_y). \end{aligned} \tag{5.58}$$

Likewise, using the bottom friction parameterization (Eq. 5.25) the bottom stress terms in the presence of disturbances become

$$\begin{aligned} \Delta\tau_x &= -\frac{f_d}{8\,h}(U+u)|\vec{U}+\vec{u}| + \frac{f_d}{8\,h}U|\vec{U}| \\ \Delta\tau_y &= -\frac{f_d}{8\,h}(V+v)|\vec{U}+\vec{u}| + \frac{f_d}{8\,h}V|\vec{U}|. \end{aligned} \tag{5.59}$$

Now in terms of the scaled variable x_1, we will use the method of multiple scales in a similar fashion to Nayfeh *et al.* (1974) who applied it to boundary layer flows. Assuming ϵ to be small, we expand the disturbance stream function ψ in the following form

$$\psi(x_1, y, t) = [\phi_0(x_1, y) + \epsilon\phi_1(x_1, y)]e^{i\theta} \tag{5.60}$$

where

$$\frac{\partial\theta}{\partial x} = k_0(x_1), \qquad \frac{\partial\theta}{\partial t} = -\omega, \tag{5.61}$$

with the real part of k_0 being the nondimensional wavenumber and the imaginary part being the growth rate. The nondimensional frequency ω is assumed to be real and we are, therefore, looking for spatially growing instabilities.

In terms of x_1 and θ the spatial and temporal derivatives transform according to

$$\frac{\partial}{\partial x} = k(x_1)\frac{\partial}{\partial\theta} + \epsilon\frac{\partial}{\partial x_1} \tag{5.62}$$

$$\frac{\partial}{\partial t} = -\omega \frac{\partial}{\partial \theta}, \tag{5.63}$$

therefore, the fast scale describes the axial variation of the traveling-wave disturbances and the slow scale is used to describe the relatively slow variation of the wavenumber, growth rate, and disturbance amplitude.

Substituting the assumed stream function and the mixing and bottom stress parameterizations into the governing equation we then separate the terms by order in ϵ. The governing equation at order ϵ^0 is given by

$$\begin{aligned} \left(U - \frac{\omega}{k}\right)\left(\phi_{0_{yy}} - k^2\phi_0\right) - \phi_0 U_{yy} = 0 \\ \text{or} \qquad \mathcal{L}(\phi_0) = 0, \end{aligned} \tag{5.64}$$

which is again the Rayleigh stability equation.

The nonparallel effects appear in the $O(\epsilon)$ equation which is given by

$$\begin{aligned} &\mathcal{L}(\phi_1) = d_1\phi_{0_{x_1}} + d_2\phi_{0_{x_1yy}} + d_3\phi_{0_y} + d_4\phi_{0_{3y}} + d_5\phi_0 + d_6\phi_{0_{yy}} + d_7\phi_{0_{4y}} \\ \text{or} \qquad &\mathcal{L}(\phi_1) = D, \end{aligned} \tag{5.65}$$

where the coefficients are defined as

$$\begin{aligned} d_1 =& 2i\omega - 3ikU - i\frac{U_{yy}}{k} \\ d_2 =& \frac{iU}{k} \\ d_3 =& -ikV - \frac{iV_{yy}}{k} - \frac{2ih_{x_1}}{kh}U_y + \frac{2if_t}{kh}U_y \\ d_4 =& \frac{iV}{k} \\ d_5 =& k_{x_1}\left(\frac{i\omega}{k} - 3iU\right) + \frac{h_{x_1}}{h}(-i\omega + 3ikU) - f_t\frac{ikU}{h} \\ d_6 =& -\frac{2ih_{x_1}}{kh}U - \frac{ikU_m b}{R_t} + 2i\frac{f_t U}{kh} \\ d_7 =& -\frac{iU_m b}{kR_t}. \end{aligned} \tag{5.66}$$

The eigenvalue problem defined by Eq. 5.64 (with U given by Eq. 5.26) can be solved numerically to determine the eigenvalue k_0 for a given ω and $U(x_1, y)$. In order to

solve the inhomogeneous second-order problem we first need to determine k_{x_1} and $\phi_{0_{x_1}}$. We can derive an expression for $\phi_{0_{x_1}}$ by differentiating Eq. 5.64 with respect to x_1, and we obtain after simplification

$$\mathcal{L}(\phi_{0_{x_1}}) = A_1 + k_{x_1} A_2, \tag{5.67}$$

where the coefficients are given by

$$\begin{aligned} A_1 =& (U_{yyx_1} + k_0^2 U_{x_1})\phi_0 - U_{x_1}\phi_{0_{yy}} \\ A_2 =& (2k_0 U - \omega)\phi_0 - \frac{\omega}{k_0^2}\phi_{0_{yy}}. \end{aligned}$$

The inhomogeneous equation governing $\phi_{0_{x_1}}$ has a solution if, and only if, the inhomogeneous terms are orthogonal to every solution of the adjoint homogeneous problem. This constraint is expressed as

$$\int_{-\infty}^{\infty} (A_1 + k_{0_{x_1}} A_2)\, \phi_0^*\, dy = 0, \tag{5.68}$$

where ϕ_0^* is the eigenfunction from the adjoint eigenproblem given by

$$(U - c)\phi_{0_{yy}}^* + 2U_y \phi_{0_y}^* - k^2 (U - c)\phi_0^* = 0. \tag{5.69}$$

Equation 5.68 can be rearranged to give the following expression for the derivative of the wavenumber

$$k_{0_{x_1}} = -\frac{\int_{\infty}^{\infty} A_1\, \phi_0^*\, dy}{\int_{-\infty}^{\infty} A_2\, \phi_0^*\, dy}. \tag{5.70}$$

Once $k_{0_{x_1}}$ is known, Eq. 5.67 can be integrated to obtain $\phi_{0_{x_1}}$.

The solvability condition for Eq. 5.65 can be written as

$$\int_{\infty}^{\infty} D\, \zeta^*\, dy = 0, \tag{5.71}$$

where we have substituted the following expression for the eigenfunction

$$\phi_0 = A(x_1)\zeta(y; x_1), \tag{5.72}$$

where $A(x_1)$ is the amplitude of the disturbance and varies in the axial direction. Direct substitution for D from Eq. 5.66 into Eq. 5.71 gives

$$\int_{\infty}^{\infty} [d_1(A_{x_1}\zeta + A\zeta_{x_1}) + d_2(A_{x_1}\zeta_{yy} + A\zeta_{x_1yy}) + d_3A\zeta_y + d_4A\zeta_{yyy}]\phi_0^* + \int_{\infty}^{\infty} [d_5A\zeta + d_6A\zeta_{yy} + d_7A\zeta_{yyyy}]\phi_0^* = 0, \tag{5.73}$$

and this can be rearranged to obtain the following evolution equation for $A(x_1)$,

$$A_{x_1} = ik_1(x_1)A \tag{5.74}$$

where

$$k_1 = \frac{i\int_{-\infty}^{\infty}(d_1\zeta_{x_1} + d_2\zeta_{x_1yy} + d_3\zeta_y + d_4\zeta_{3y} + d_5\zeta + d_6\zeta_{yy} + d_7\zeta_{4y})\phi_0^* dy}{\int_{\infty}^{\infty}(d_1\zeta_+ d_2\zeta_{yy})\phi_0^* dy}, \tag{5.75}$$

and the d_n are defined by Eq. 5.66.

5.3.4 Numerical Method

The boundary conditions for the eigenvalue problem described by Eq. 5.64 are as follows:

$$\phi_0 = \phi_{0_y} \to 0 \quad \text{as} \quad y \to \pm\infty \tag{5.76}$$

$$\begin{aligned} \phi_{0_y} &= 0 \text{ at } y = 0 \to \text{sinuous mode} \\ \phi_0 &= 0 \text{ at } y = 0 \to \text{varicose mode.} \end{aligned} \tag{5.77}$$

In order to implement the boundary condition (5.76) at a finite value of y, we utilize the conditions $U, U_{yy} \to 0$ as $y \to \infty$ to obtain the asymptotic form of Eq. 5.64. Given an ω and an initial guess for k_0, the solution to the asymptotic equation ($\phi_0 = e^{-k_0 y}$) is applied at a sufficiently large y and then Eq. 5.64 is integrated (shooting method) using a fourth-order Runge-Kutta algorithm (Hoffman, 1992). At $y = 0$ the boundary condition Eq. 5.77 is evaluated, and k_0 is iterated using the secant method until the wavenumber is found which satisfies the boundary condition.

With k_0 known Eq. 5.69 is integrated using a similar procedure, however, only one iteration is necessary since the adjoint problem has the same eigenvalues as the original problem. The calculation of ϕ_0^* can then be used as a check on the accuracy of the computed eigenvalues. Equation 5.67 is also integrated using a similar procedure. The step size for the numerical integration procedure was generally $\Delta y = 0.0005 \cdot b(x_1)$, and, therefore, varied in the axial direction. The distance from the jet axis where Eq. 5.76 was implemented was $y = 6 \cdot b(x_1)$.

Finally, the complex wavenumber including nonparallel effects is given (to order ϵ) by

$$\alpha \equiv (k_0 + \epsilon k_1) \tag{5.78}$$

where α_i is the local growth rate and α_r is the local (physical) wavenumber. The small parameter ϵ is the ratio between the longshore and cross-shore velocitie scales or V_{max}/U_{max}, which for the viscous, turbulent jet becomes

$$\epsilon \equiv \frac{V_{max}}{U_{max}} = \frac{2}{R_t}. \tag{5.79}$$

5.3.5 Stability characteristics

A reasonable first estimate of the instability scales of the rip current are given by the zeroth order stability equation (Eq. 5.64), these results correspond to the results from a purely parallel flow theory. The spatial instability curve and dispersion relation for the rip current disturbances are shown in Figure 5.4 for both the sinuous and varicose modes. As a check on these results, the temporal stability curves were calculated from these spatial results, again using Gaster's relations (Eqs. 5.15-5.16). The temporal results, calculated in this manner, are in excellent agreement with the directly computed temporal results of Drazin and Howard (1966) who studied the Bickley Jet ($U = sech^2(y)$).

It is important to note that the scales of the fastest growing spatial mode are not necessarily equal to those of the fastest growing spatial mode, since they are

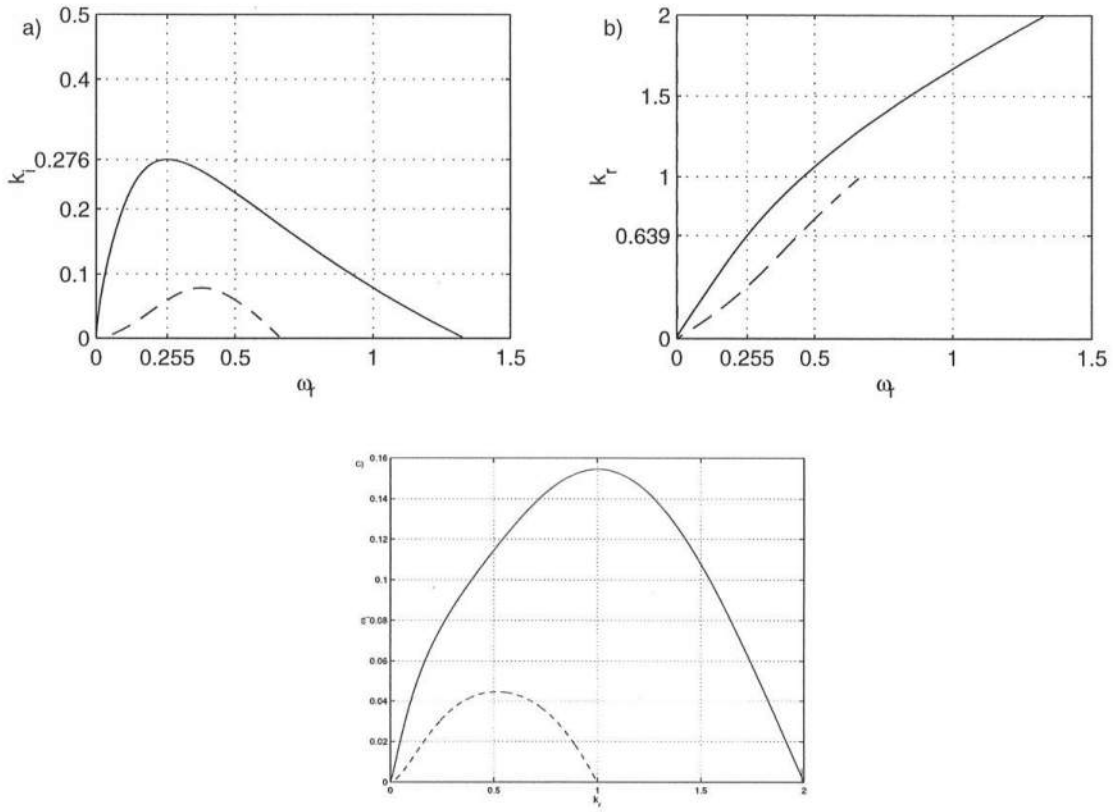

Figure 5.4: (a) Spatial growth rate vs. frequency (b) wavenumber vs. frequency, and (c) temporal growth rate vs. wavenumber for the parallel turbulent jet. Sinuous modes - (solid line) varicose modes - (dashed line) all variables are nondimensional.

distinct phenomena. The relations of Gaster simply indicate that, if growth rates are small, the results of one (spatial or temporal) calculation can be related to the other.

The spatial results, shown in Figure 5.4 a and b, indicate that the sinuous modes have the highest growth rates, and the fastest growing sinuous mode has nondimensional frequency $\omega = 0.255$, wavenumber $k_r = 0.639$, and phase speed that is nearly 40% of the maximum jet velocity. By comparing to the results of the triangle jet (Fig. 5.2d), we see that including a more realistic velocity profile has shifted the fastest growing mode (FGM) to a lower frequency and a smaller

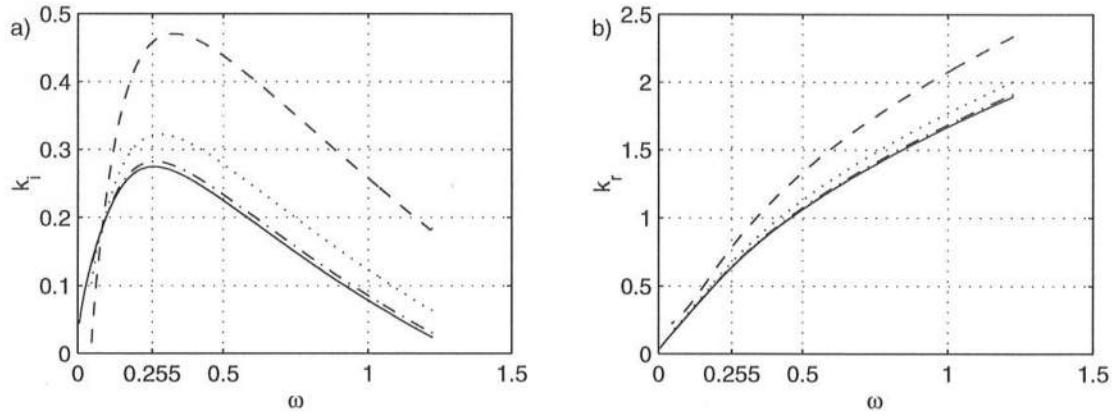

Figure 5.5: (a) Growth rate vs. frequency (b) wavenumber vs. frequency for different turbulent Reynolds numbers, $R_t = 5$ dashed line, $R_t = 10$ dotted line, $R_t = 25$ dash-dot line, parallel flow solid line, all variables are nondimensional and results are for flat bottom and $f_t = x_1$=0.

wavenumber. Perhaps most importantly, there is a large difference between the scales of the spatial FGM and the temporal FGM ($\omega_r = 0.46$, $k_r = 1.0$). Therefore, unlike many other instabilities (e.g. longshore current instabilities, see Dodd and Falques, 1996) the temporal theory cannot be assumed to apply for spatially growing disturbances. However, the spatial results can be calculated accurately from the temporal results using Gaster's relations at this level of approximation.

Since, at this level of approximation, the stability scales are not a function of R_t, h, or f_t we will have to move to the next order (Eq. 5.65) in order to investigate the nonparallel effects due to turbulent mixing, vortex stretching, and bottom friction, respectively. Figure 5.5 demonstrates the effect of turbulent mixing on the rip current jet instability. From this figure we can see that the initial growth rates increase inversely with R_t and the frequency of the fastest growing mode also increases slightly with lower R_t. In addition, the phase speeds vary directly with R_t, such that lower R_t causes slower phase speeds. These results are mostly explained by the fact that the magnitude of the nonparallel effects (i.e. ϵ) is proportional to

$1/R_t$. Physically, the increased growth rates are a direct result of the increased inflow (V) into the jet, the increased inflow also causes the disturbances to propagate at a slower speed. These results are consistent with those of Garg and Round (1978) who analyzed the effects of viscous stresses in laminar jet flows. It is also evident that at very high values of R_t the solutions collapse to the parallel flow values (solid lines).

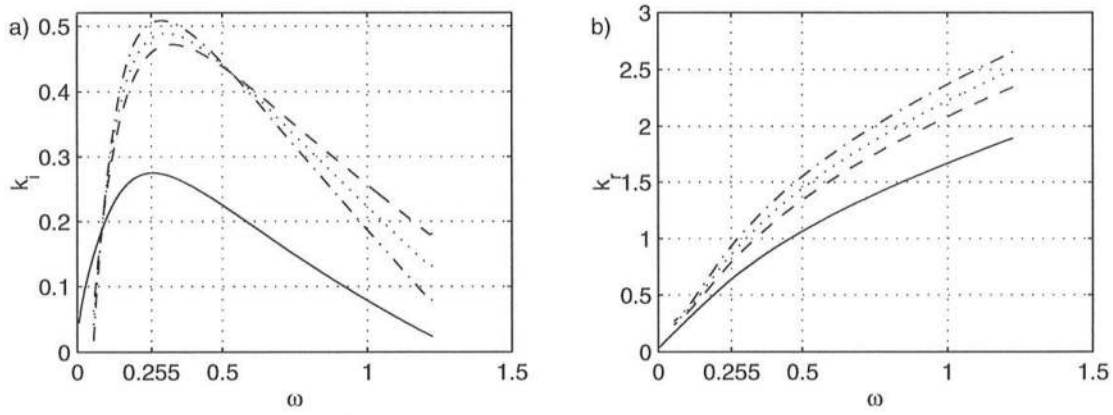

Figure 5.6: (a) Growth rate vs. frequency (b) wavenumber vs. frequency for different values of bottom friction, $f_t = 0.01$ dashed line, $f_t = 0.2$ dotted line, $f_t = 0.4$ dash-dot line, parallel flow solid line, all variables are nondimensional and results are for flat bottom, x_1=0, and $R_t = 5$.

Figure 5.6 shows the effect of bottom friction on the instabilities. Interestingly, the figure indicates that increased bottom frictional dissipation causes an increase in the initial growth rates and a decrease in the range of unstable frequencies. The increased growth rates are due to the effect of the decay of the centerline velocity. Essentially, since with increased bottom friction the jet initially spreads very quickly, the inflow is initially much stronger and therefore the jet is more unstable. Additionally, the increased bottom friction causes the disturbances to propagate more slowly, as can be seen by the dispersion curves. The results collapse to those for $f_t = 0$ and $R_t = 5$ (Fig. 5.5) for very low friction.

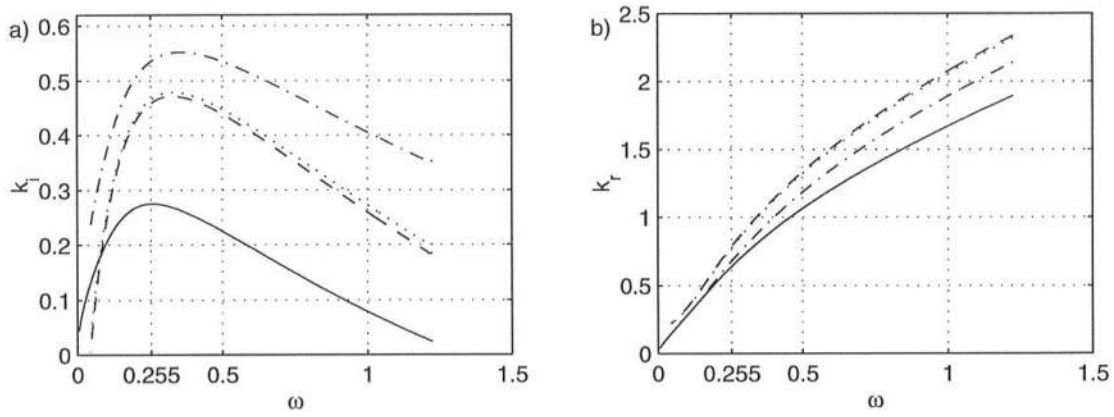

Figure 5.7: (*a*) Growth rate vs. frequency (*b*) wavenumber vs. frequency for different bottom slopes, $m_1 = 0.001$ dashed line, $m_1 = 0.01$ dotted line, $m_1 = 0.1$ dash-dot line, parallel flow solid line, all variables are nondimensional, $f_t = 0$ and $R_t = 5$.

Figure 5.7 shows the effects of different bottom slopes on the instabilities. The results indicate that increased bottom slope increases the initial growth rates. This is related to the effects of vortex stretching and of spatial deceleration of the rip current. Though the jet does not spread as quickly on a sloping beach compared to a flat bottom due to vortex stretching, the centerline velocity decays more quickly with increased beach slope due to continuity effects. This increased spatial deceleration causes the initial growth rates to increase. Also the phase speeds of the disturbances increases on the relatively narrower jets of planar beaches.

Figure 5.8 shows the variation of the scales of the fastest growing modes down the centerline of the jet. The results show that the frequency of the fastest growing mode decreases down the centerline, which suggests that different modes are excited at different locations along the jet axis. Correspondingly, the local wavenumber of the fastest growing mode also decreases. Additionally, the local growth rate of the fastest growing mode decreases as the jet spreads. The axial variation of the disturbance scales is most pronounced at lower values of R_t and is extremely small

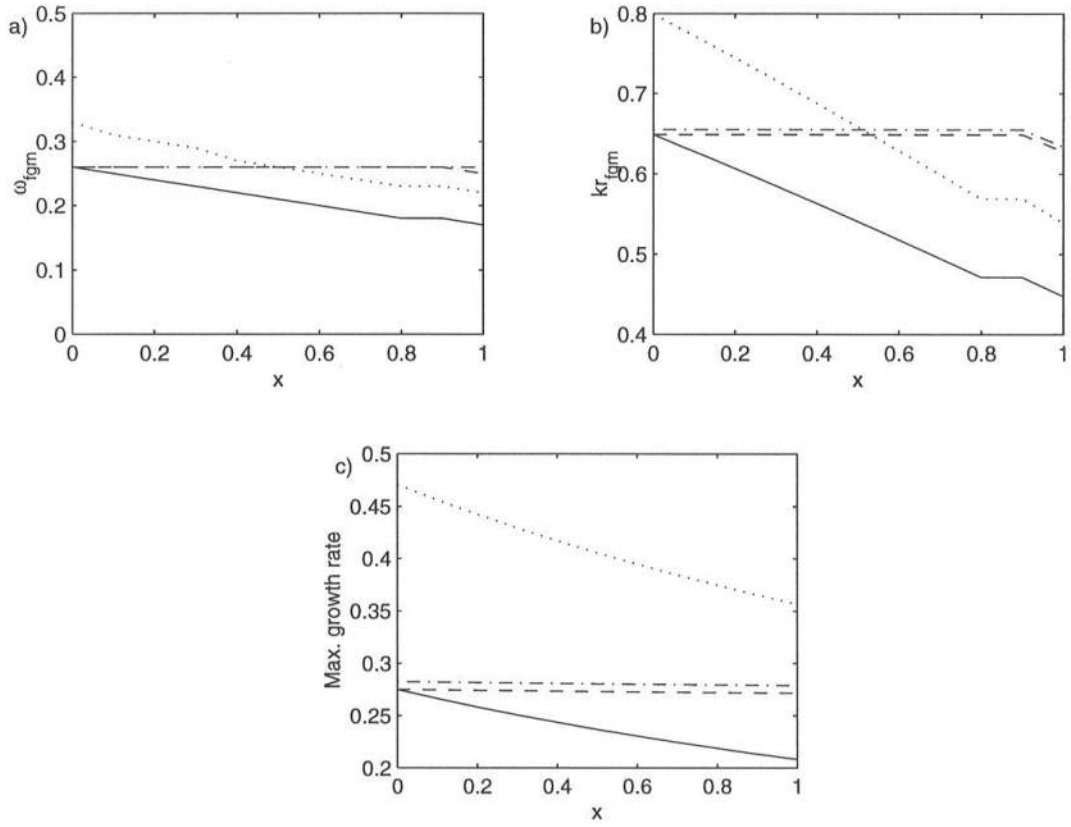

Figure 5.8: (a) Frequency vs. x (b) wavenumber vs. x (c) growth rate vs. x for the fastest growing modes, $R_t = 5$ parallel theory (solid), nonparallel theory (dotted); R_t=25 parallel theory (dashed) nonparallel theory (dash-dot); $m_1 = f_t$=0, all variables are nondimensional.

for values $R_t \geq 25$, since, for higher values of R_t, the flow is nearly parallel.

5.4 Model/Data Comparison

In the following section we will compare the results from our model for rip current mean flows with the measured velocity profiles from the experiments and evaluate whether the linear instability model can predict the scales of the observed low frequency motions. In order to compare the model/data rip current mean flows we adopt a new cross-shore coordinate axis $x^{'} = x_0 - x$ where x_0 is the cross-shore location (dimensional) of the base of the rip current during the experiments. The

location x_0 was determined as the experimental location where the rip begins to exhibit decay of its centerline velocity. The location of the rip current centerline, y_0, was determined by taking a weighted average of the peak rip current velocity at the jet origin (x_0). This is given by

$$y_0 = \frac{\int_{-\infty}^{\infty} U \cdot y \, dy}{\int_{-\infty}^{\infty} U \, dy}. \tag{5.80}$$

Once x_0 and y_0 were determined the choice of the dimensional velocity and width scales, U_0 and b_0, respectively, were made by a least squares fitting procedure performed using the initial rip profile (at $x' = 0$). The statistical parameter we use to determine the best fit of model to data is the index of agreement d_i that was proposed by Wilmott (1981) and is given by

$$d_i = 1 - \frac{\sum_{i=1}^{n}(y(i) - x(i))^2}{\sum_{i=1}^{n}(|y(i) - \overline{x}| + |x(i) - \overline{x}|)^2}, \tag{5.81}$$

where $x(i)$ and $y(i)$ are the measured and model data, respectively, and $\overline{x}$ is the measured data mean. This parameter varies between 0 and 1 with $d_i = 1$ representing complete agreement. In order to determine the initial jet scales the index of agreement was computed for a wide range of scales and the best fit was chosen from the maximum value of d_i. This fixed the initial length and velocity scales of the rip current with a resolution of $\Delta U_0 = 0.1 cm/s$ and $\Delta b_0 = 1 cm$.

The mixing and friction scales R_t and f_t were also determined by a similar procedure. It is evident from Equations 5.44 and 5.49 that the decay of the centerline velocity is directly related to the values of R_t and f_t. Therefore, these parameters were determined by fitting the decay of the centerline velocity between model and data results with a resolution of $R_t = 0.25$ and $f_t = 0.0093$. Since the experimental data points were never located at the exact centerline of the rip the model was fit to the data point located closest to the centerline.

The best fit modeled velocity profiles are shown in Figures 5.9-5.13. The dimensional scales and the index of agreement for each test are listed in Table 5.1.

Test	U_0 (cm/s)	b_0 (cm)	x_0 (m)	y_0 (m)	d_i	R_t	f_t	d_i'
B	19.7	73	12.0	13.68	.96	4.25	.48	.88
C	29.1	64	11.7	13.57	.94	4.75	.475	.90
D	49	62	11.5	13.74	.91	-	-	-
E	28.4	52	12.0	13.8	.94	2.5	.46	.94
G	23.4	71	12.0	13.68	.95	2.75	.44	.97

Table 5.1: Table of rip current scales determined by least-squares procedure, U_0 velocity scale, b_0 width scale, x_0 cross-shore location of rip current origin, y_0 longshore location of rip current centerline, d_i index of agreement for U_0 and b_0, R_t turbulent Reynolds number, f_t bottom friction parameter, d_i' index of agreement for R_t and f_t.

No estimate of R_t and f_t could be made for Test D since the decay of the rip current velocity is not captured by the measurements. The table also shows that the model did a reasonable job of fitting to the measured profiles since the index of agreement is at least 0.88 for all cases. However, it should be noted that for much of the least squares fitting there was only three data points for comparison which is a rather small amount.

Once the relevant scales of the rip currents are determined, we can now use the model to investigate the instability characteristics of the experimental rip currents. Figures 5.14-5.17 show the growth and dispersion relations for the sinuous modes of rip current instability at three different locations along the jet axis. It is immediately evident from these figures that the nonparallel effects strongly affect the growth rates and phase speeds of the disturbances. In addition, the predicted dimensional time scales of the fastest growing modes compare well with the measured spectra shown in Chapter 4. This is shown graphically in Figure 5.18. The figure shows the predicted frequency of the fastest growing mode at the base of the rip current with the nearest significant spectral peak shown in Figures 4.7,4.19, and 4.20-4.23. It is evident that the model does a very good job of predicting the presence of instabilities for Tests

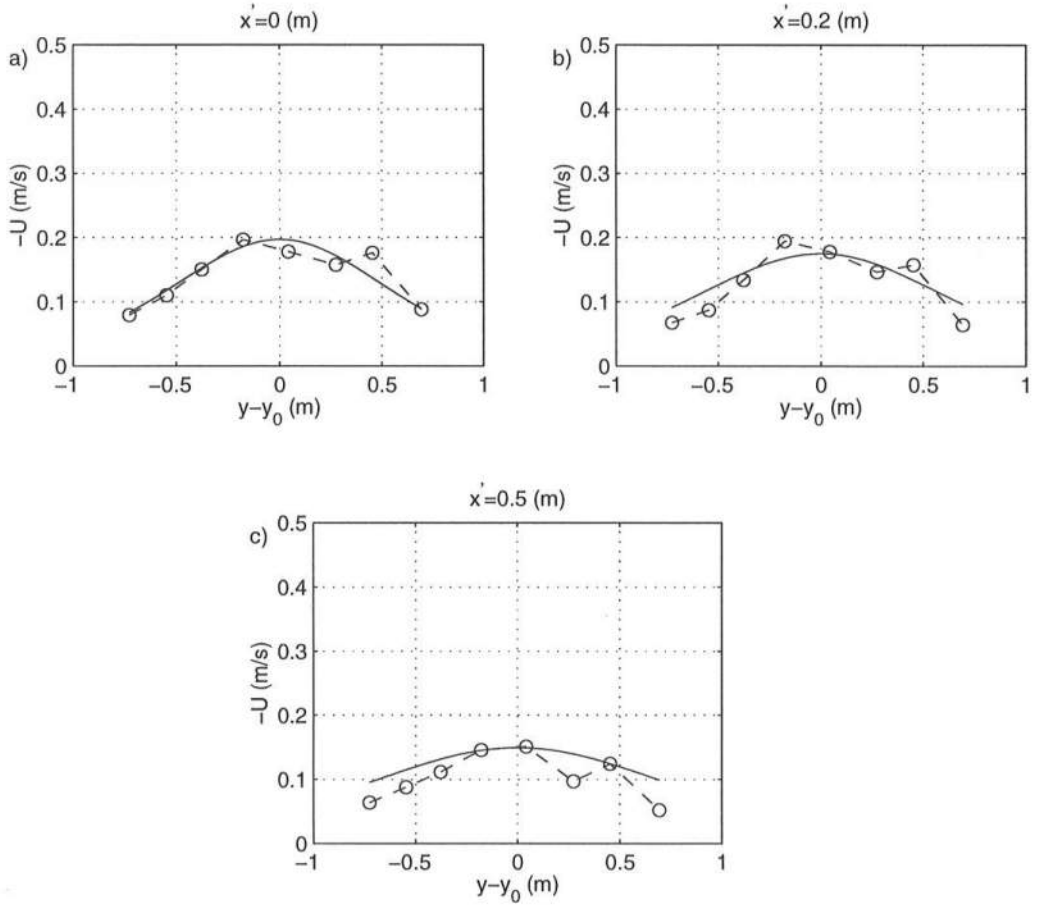

Figure 5.9: Comparison of best fit mean rip current velocity profile to experimental data for Test B (*a*) $x^{'}$=0 m (x=12 m) (*b*) $x^{'}$=0.2 m (x=11.8 m) and (*c*) $x^{'}$ =0.5 m (x=11.5 m).

C, D, and G at the frequencies of the fastest growing modes. The model does less well with Tests B and E.

In order to gain an estimate of the length scales of the disturbances measured during the experiments, the cross-spectra were computed from the longshore velocity data measured in the rip channel. Since we only had three ADVs in operation during the experiments and therefore only three sensor lags to compute cross-spectra, it was difficult to obtain statistically meaningful estimates of the disturbance wavelengths. However, Figures 5.19-5.20 show the phase and coherence as a function of cross-shore

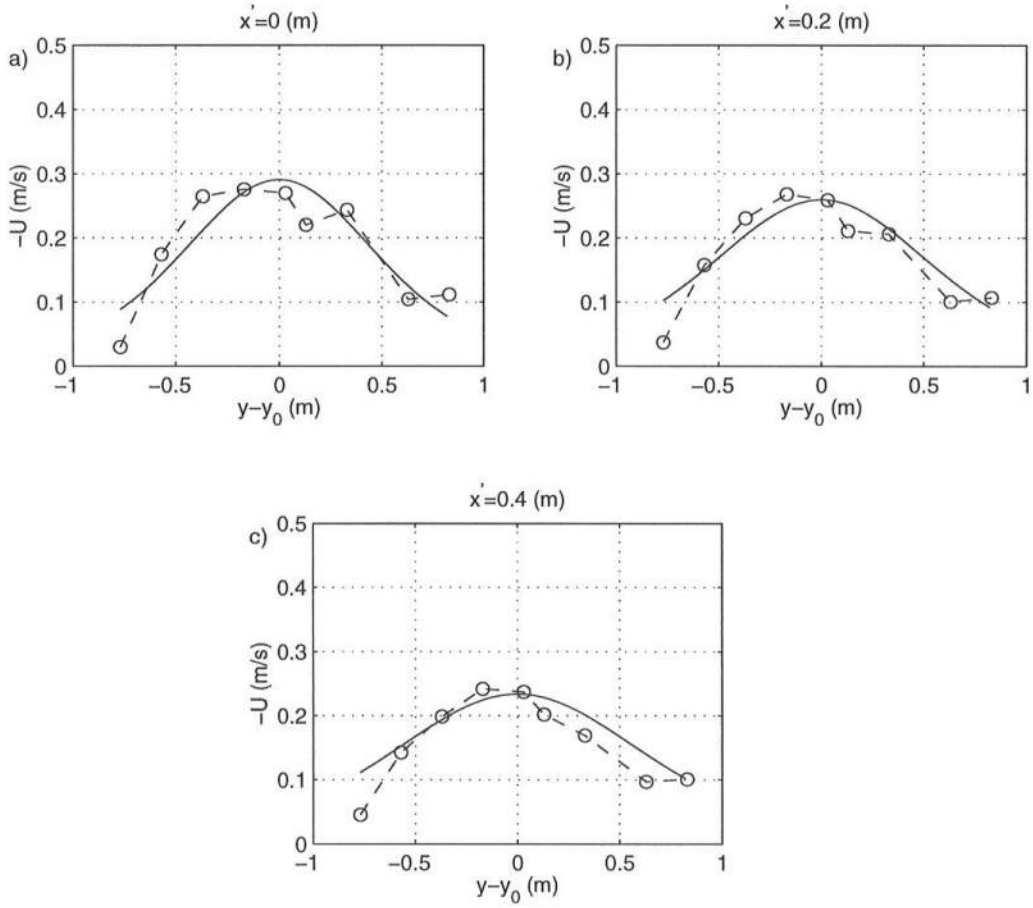

Figure 5.10: Comparison of best fit mean rip current velocity profile to experimental data for Test C (*a*) $x^{'}$=0 m (x=11.7 m) (*b*) $x^{'}$ = 0.2 m (x=11.5 m) and (*c*) $x^{'}$ =0.4 m (x=11.3 m).

lag for two frequency bins during Tests C and G. Using the average phase variation as a function of distance we can estimate the wavelength of the coherent motions at these frequencies. The experimental estimates of the nondimensional wavenumber at these frequencies are ω=0.25, k_r = 1.49 Test C, and ω=.23, k_r = 2.23. These estimates of the length scales at these frequencies are in fair agreement with the results shown in Figures 5.15-5.17.

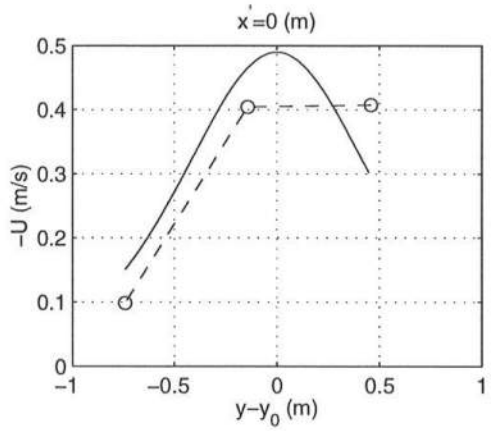

Figure 5.11: Comparison of best fit mean rip current velocity profile to experimental data for Test D, x'=0 m (x=11.5 m).

5.5 Summary

In this chapter we developed a model for the mean flows in rip currents based on the governing vorticity balance within these offshore directed flows. The model includes the effects of a variable cross-shore beach profile, turbulent mixing, and bottom friction. The model utilizes a multiple scales technique and is strictly valid for long narrow jet-like currents. The mean rip current profiles are self-similar and related to the well-known Bickley jet solution.

Previous analyses of temporal jet instabilities including the "top-hat" jet, the triangle jet, and the Bickley jet were reviewed and compared with the predictions of the present model for spatially growing instabilities. Our results show that the stability characteristics of the spatially growing rip current instabilities are very different from those of the previous analyses. Additionally, the influence of nonparallel effects is shown to be quite strong for the rip currents observed during these experiments. The nonparallel effects are shown to increase the growth rates of the instabilities and decrease their phase speeds.

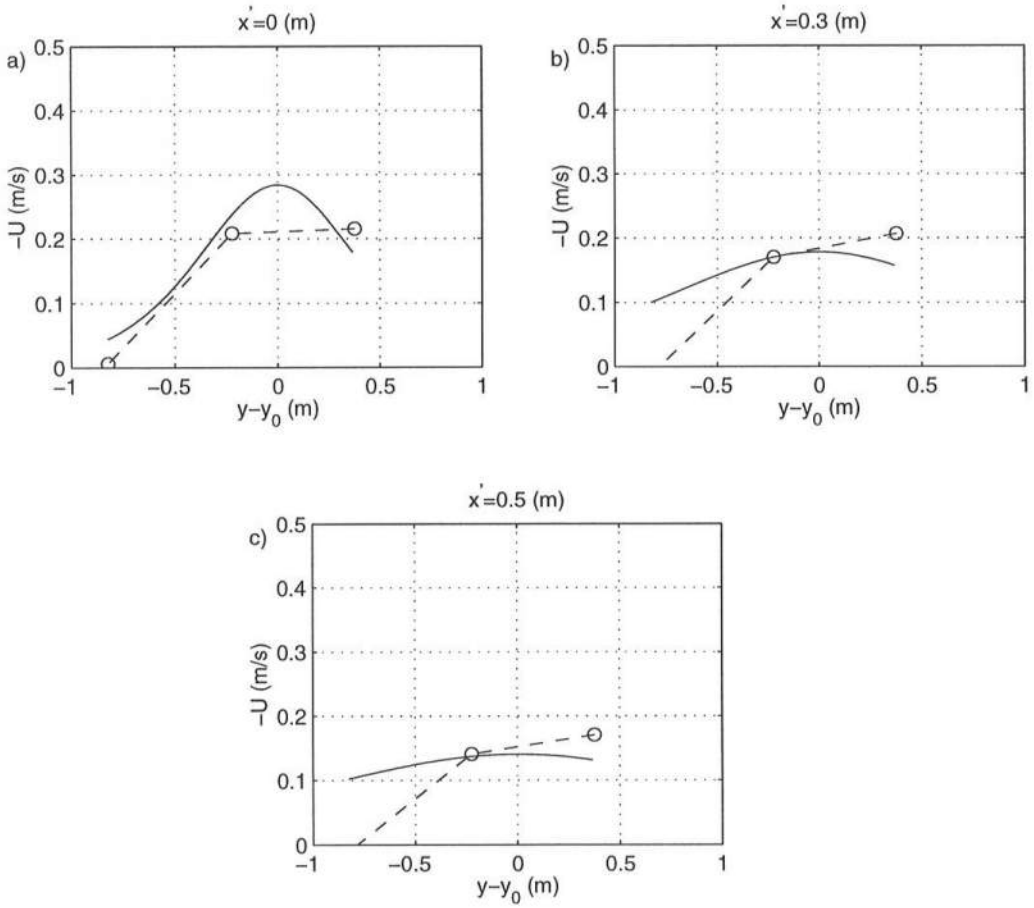

Figure 5.12: Comparison of best fit mean rip current velocity profile to experimental data for Test E (*a*) $x^{'}$=0 m (x=12.0 m) (*b*) $x^{'}$ = 0.3 m (x=11.7 m) and (*c*) $x^{'}$ =0.5 m (x=11.5 m).

Finally, the rip current stability characteristics predicted by the linear stability model are shown to compare quite well with the measured disturbances. The predictions for Tests C, D, and G are well within the range of experimental uncertainty, Tests B and E are predicted less well. The results strongly suggest that a rip current instability mechanism can explain much of the low frequency motions observed during the experiments.

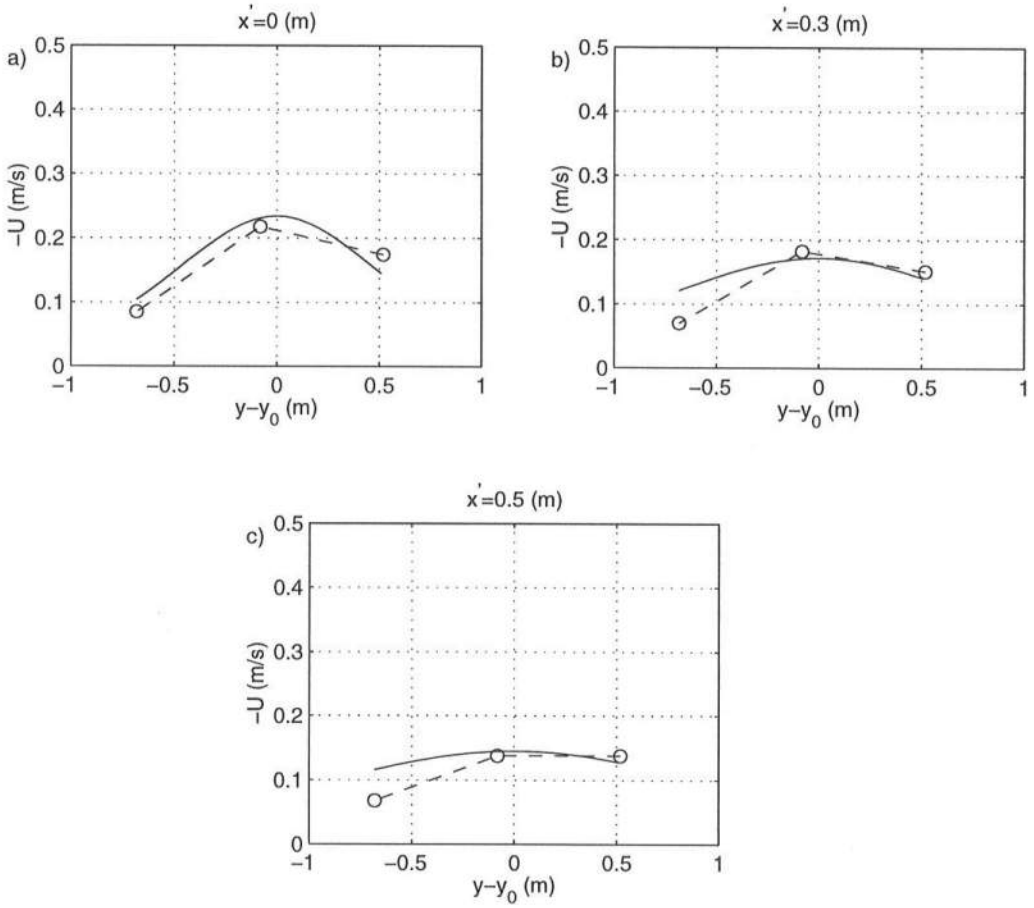

Figure 5.13: Comparison of best fit mean rip current velocity profile to experimental data for Test G (*a*) $x^{'}$=0 m (x=12.0 m) (*b*) $x^{'}$ = 0.3 m (x=11.7 m) and (*c*) $x^{'}$ =0.5 m (x=11.5 m).

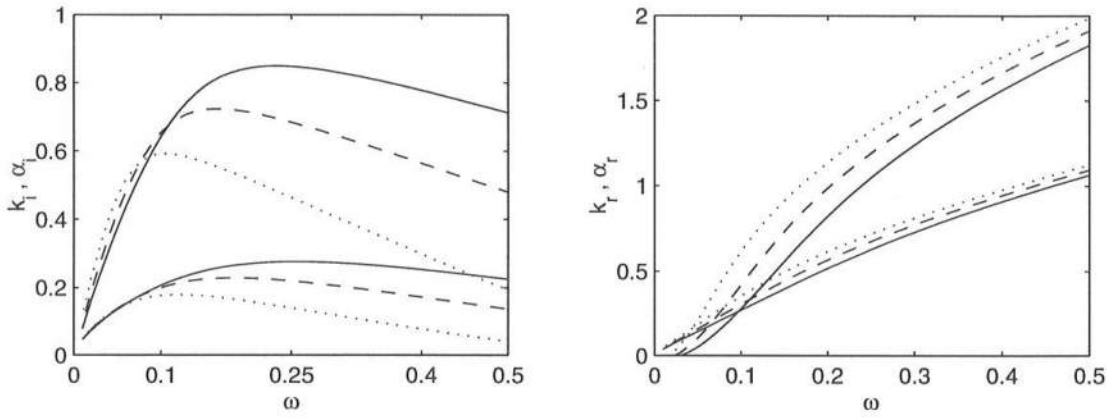

Figure 5.14: (a) Growth rate vs. frequency (b) wavenumber vs. frequency for Test B, all variables are nondimensional. $x^{'} = 0$ solid line, $x^{'} = 0.2$ dashed line, $x^{'} = 0.5m$, upper curves include nonparallel effects, lower curves are for parallel flow theory.

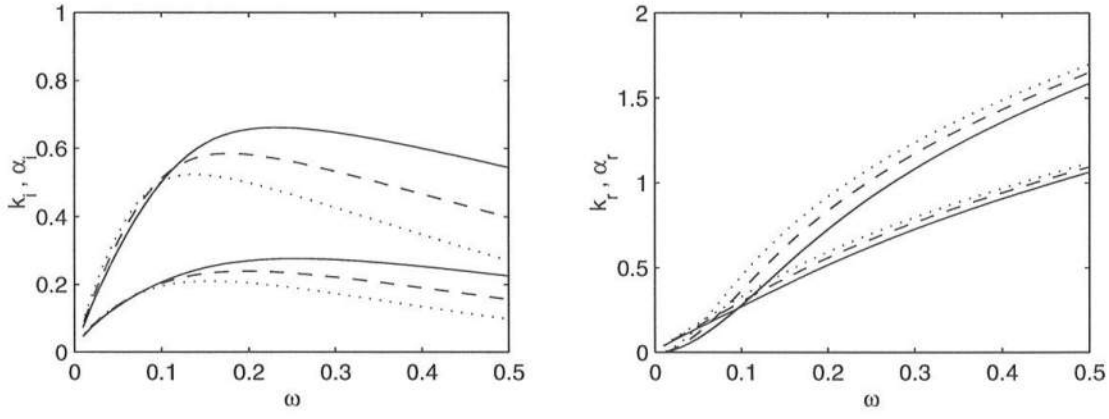

Figure 5.15: (a) Growth rate vs. frequency (b) wavenumber vs. frequency for Test C, all variables are nondimensional. $x^{'} = 0$ solid line, $x^{'} = 0.2m$ dashed line, $x^{'} = 0.4m$, upper curves include nonparallel effects, lower curves are for parallel flow theory.

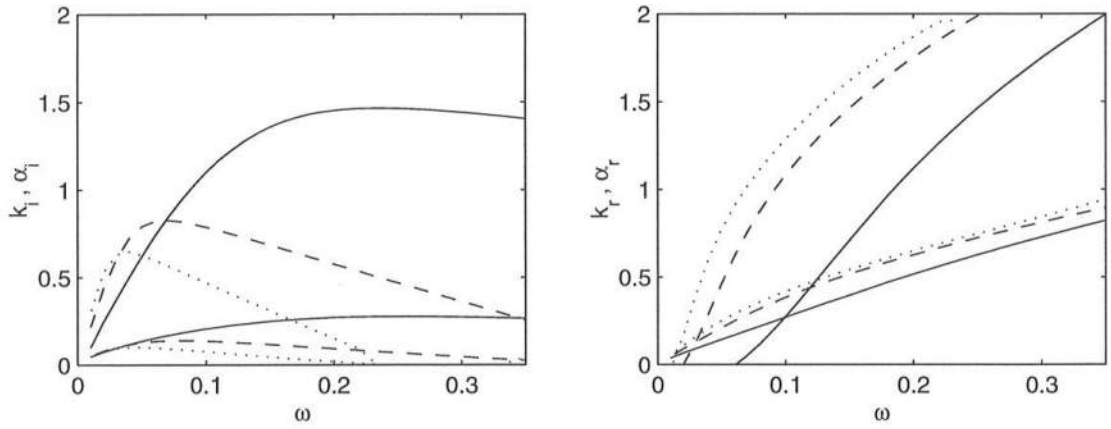

Figure 5.16: (a) Growth rate vs. frequency (b) wavenumber vs. frequency for Test E, all variables are nondimensional. $x^{'} = 0$ solid line, $x^{'} = 0.3m$ dashed line, $x^{'} = 0.5m$, upper curves include nonparallel effects, lower curves are for parallel flow theory.

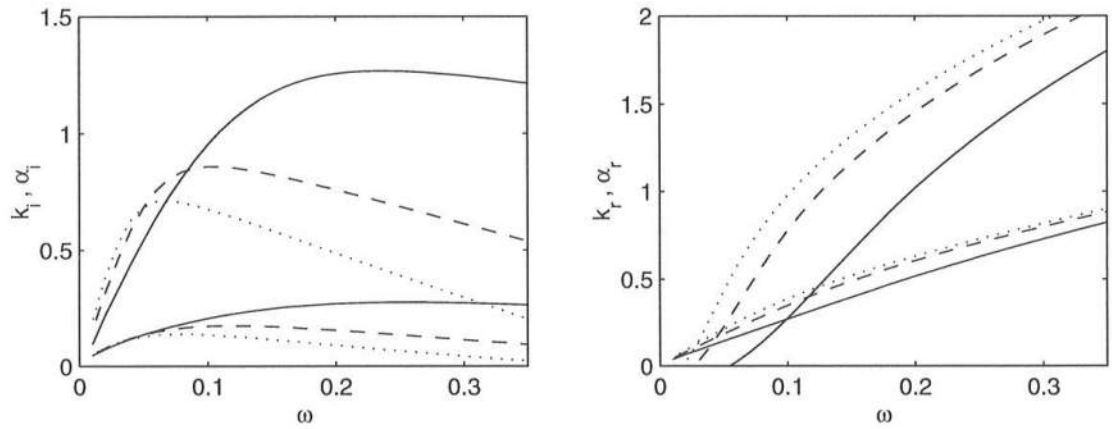

Figure 5.17: (a) Growth rate vs. frequency (b) wavenumber vs. frequency for Test G, all variables are nondimensional. $x^{'} = 0$ solid line, $x^{'} = 0.3m$ dashed line, $x^{'} = 0.5m$, upper curves include nonparallel effects, lower curves are for parallel flow theory.

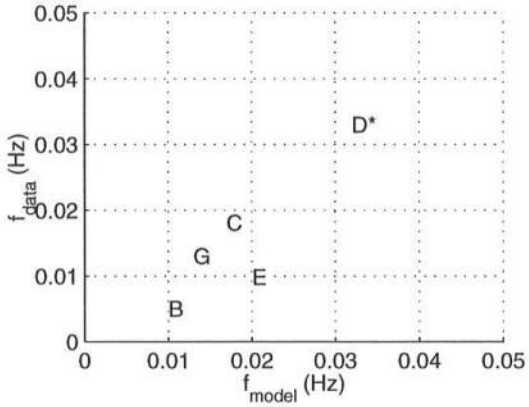

Figure 5.18: Comparison of predicted dimensional frequency of the spatial FGM vs. the nearest significant spectral peak in the measured longshore velocity spectrum of the experimental rip currents for each test. *Predicted frequencies include nonparallel effects except for Test D which only includes parallel effects.

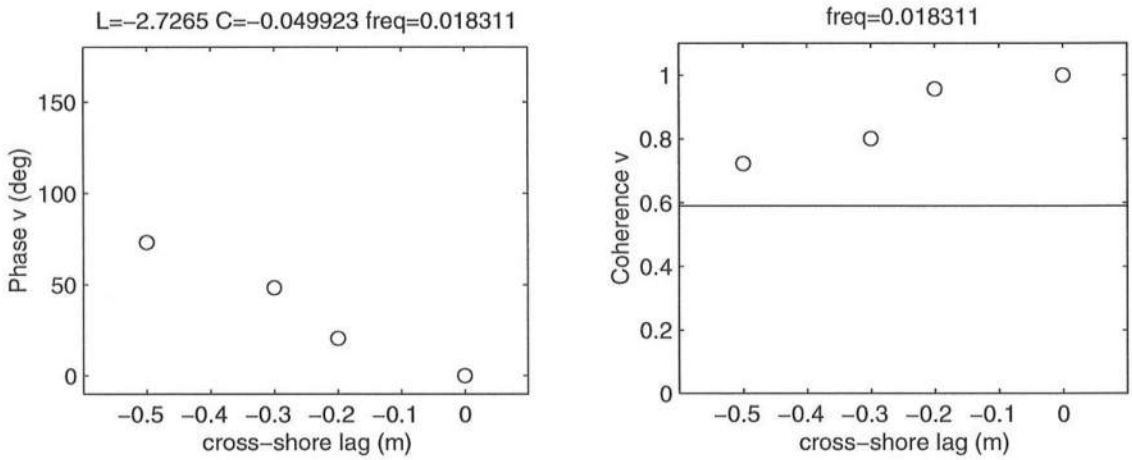

Figure 5.19: (*a*) Phase vs. cross-shore sensor separation (*b*) coherence vs. cross-shore sensor separation for Test C, run 34, Δf=0.0012 Hz, d.o.f.=16.

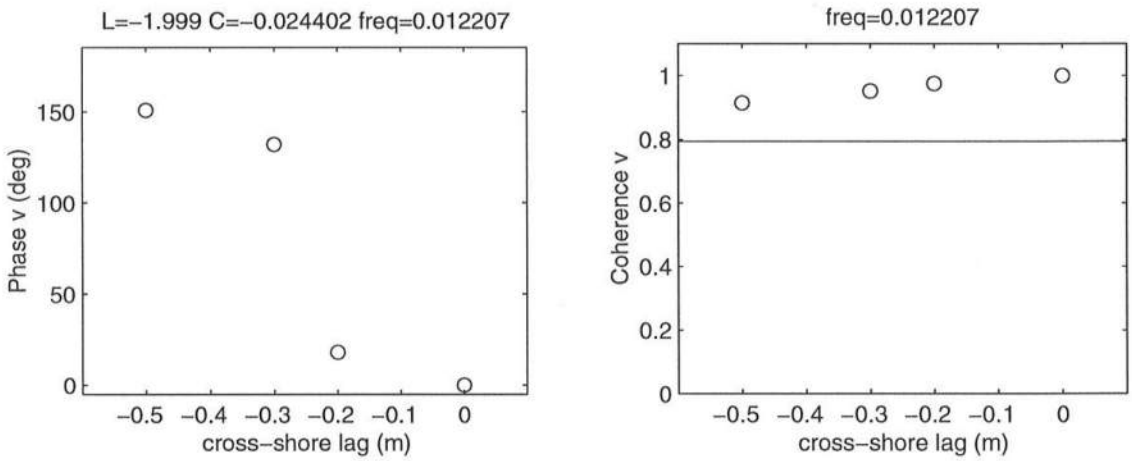

Figure 5.20: (*a*) Phase vs. cross-shore sensor separation (*b*) coherence vs. cross-shore sensor separation for Test G, run 3, Δf=0.0024 Hz, d.o.f.=8.

Chapter 6

CONCLUSIONS

The focus of this study was to make detailed observations of the effects of longshore varying bathymetry on nearshore circulation. For this purpose, a physical model of a barred beach including two rip channels was designed and built in a laboratory wave basin. The experiments examined in detail the modification of the incident wave field by the bars and the resulting variations in the mean water levels for monochromatic, normally incident waves. The effects of oblique incidence were not examined in detail.

The experimental results indicated that periodic gaps in longshore bars strongly modify the nearshore circulation field. Two circulation cells were shown to exist. The primary circulation cell consists of the shoreward flux over the bars that supplies longshore feeder currents which join at the base of the rip and then flow offshore in rip currents. The secondary circulation is driven shoreward of the rip channels where there is increased wave breaking. These breaking waves drive flow away from the rip channels along the shoreline. These secondary currents induce a strong shear in the longshore current and eventually become re-entrained in the primary feeder currents and return offshore in the rips. Detailed maps of the wave and current fields under varying wave conditions were obtained during these experiments. It is expected that this rich data set will provide a valuable resource for evaluating nearshore circulation models on longshore varying bathymetries.

The experiments also indicated the presence of unsteady rip current motions. A detailed analysis of the natural basin seiching modes indicates that the observed

low frequency motions cannot be explained by the presence of natural basin modes but instead are limited to a region very near the rip neck. An examination of simultaneous wave and current measurements demonstrated that these motions are associated with the cross-channel mean water level gradient and that as the rip current migrates back and forth in the channel the cross-channel surface gradient likewise oscillates. The signature of these rip current oscillations are most distinct in the longshore velocity records measured near the rip neck.

Spectral analysis of the rip current velocity records reveals distinct low frequency energy peaks. During most of the experiments multiple peaks are observed and the presence of peaks very near to sum and difference frequencies of the two dominant peaks suggests that the motions are interacting nonlinearly. The presence of strong shear in the mean rip velocity profile and the presence of low frequency disturbances superimposed on the rip flow strongly suggests a rip current instability mechanism.

In order to test the hypothesis that the low frequency rip current motions are derived from a fluid dynamic instability we developed a model for the rip current flow. A model based on the nearshore vorticity balance was developed for the mean flows in a rip current. The model incorporates the effects of variable bathymetry, bottom friction, and turbulent mixing. The velocity profiles are assumed to be of self-similar type. The model profiles compare reasonably well with the measured data.

The stability characteristics of jets were examined using both temporal and spatial linear stability theory and the results were shown to not be equivalent for the rip current velocity profile. The effects of nonparallelism were incorporated into the linear stability model using a multiple scales approach and the nonparallel effects enter the problem as a correction to the parallel flow results. Increased bottom friction was shown to increase the initial growth rates of the instabilities due to the

effect of spatial deceleration of the rip current flow. In addition, at low values of R_t local growth rates are significantly higher than those predicted by the parallel flow theory due to the destabilizing effects of nonparallel effects (e.g. transverse inflow). Also, phase speeds are decreased due to nonparallel effects.

Finally, the results from the linear stability model compare very well with the measured low frequency motions. The presence of significant energy peaks very near the frequencies of the fastest growing unstable modes in the linear stability model strongly suggests that fluid instabilities are a source of much of the observed low frequency motions.

It is noted that the modeling effort undertaken in this study is a linear approximation to the problem. The experimental results suggest that nonlinearity is an important factor in the rip current oscillations. Though the present model is heavily simplified, it does provide insight into the initial growth of rip current instabilities. However, it is a logical next step to analyze rip current vorticity dynamics through a nonlinear modeling effort. Topics of interest are the finite amplitude behavior of rip current instabilities including modal interactions and interactions with the incident wave field.

Another topic not well addressed by this study is the depth variation of the circulation systems. It is highly likely that the rip current contains significant variability with depth offshore of the rip channel. This topic would be better investigated with certain modifications to the existing equipment that would allow simultaneous measurements at various depths within the rip.

In conclusion, the collected data set is rich. The set has quantified significant aspects of the nearshore circulation system in further detail then pre-existing data sets. The results have led to further study of the previously unexamined phenomenon of rip current instabilities. It is expected that the data set will provide a valuable tool in the evaluation of present nearshore circulation models.

REFERENCES

Arthur, R.S. (1950). Refraction of shallow water waves: The combined effect of currents and underwater topography. *Eos Trans. AGU,* 31, 549-551.

Arthur, R.S. (1962). A note on the dynamics of rip currents. *J. Geophys. Res.,* 67, 2777-2779.

Bickley, W.G. (1939). The plane jet. *Phil. Mag. Ser.,* (7) 23, 727-731.

Bowen, A.J. (1970). Rip currents, I. Theoretical investigations. *J. Geophys. Res.,* 74, 5467-5478.

Bowen, A.J. and D.L. Inman (1970). Rip currents, II. Laboratory and field observations. *J. Geophys. Res.,* 74, 5479-5490.

Bowen, A.J. and R.A. Holman (1989). Shear instabilities of the mean longshore current. 1. Theory. *J. Geophys. Res.,* 94, 18023-18030.

Bowman, D., D. Arad, D.S. Rosen, E. Kit, R. Goldbery, and A. Slavicz (1988). Flow characteristics along the rip current system under low-energy conditions. *Marine Geology,* 82, 149-167.

Branner, J.C. (1900). The origin of beach cusps. *Jour. Geol.,* 8, 481-484.

Chen, Q., R.A. Dalrymple, J.T. Kirby, A.B. Kennedy, and M.C. Haller (1999). Boussinesq modeling of a rip current system. To appear in *J. Geophys. Res.*.

Cooke, D.O. (1970). The occurrence and geologic work of rip currents off southern California. *Mar. Geol.,* 32:231-250.

Dalrymple, R.A. (1975). A mechanism for rip current generation on an open coast. *J. Geophys. Res.,* 80, 3485-3487.

Dalrymple, R.A. and G.A. Lanan (1976). Beach cusps formed by intersecting waves. *Bull. Geol. Soc. Am.,* 87, 57-60.

Dalrymple, R.A., R.A. Eubanks, and W.A. Birkemeyer, (1977). Wave induced circulation in shallow basins. *J. Waterway, Port, and Coastal Engineering,* ASCE, Vol. 103, 117-135.

Dalrymple, R.A. (1978). Rip currents and their causes. *Proc.* 16^{th} *Intl. Conf. Coast. Engrg.,* vol.2, Hamburg, Germany, ASCE.

Dalrymple, R.A. and C.J. Lozano (1978). Wave-current interaction models for rip currents. *J. Geophys. Res.,* 83, 6063-6071.

Dette, H-H., K. Peters, and F. Spingat (1995). About rip currents at a mesotidal coast. In *Proc. of Coastal Dynamics'95*, Barcelona, Spain, 477-488, ASCE.

Dodd, N. and A. Falques (1996). A note on spatial modes in longshore current shear instabilities. *J. Geophys. Res.,* 101, 227150-22726.

Dolan, R. (1971). Coastal landforms: crescentic and rhythmic. *Geol. Soc. Am. Bull.,* 82:177-180.

Drazin, P.G. and L.N. Howard (1966). Hydrodynamic stability of parallel flow of inviscid fluid. In: *Advances in applied mechanics,* vol. 7, ed. G. Kuerti, pp. 1-89, New York, Academic Press.

Drazin, P.G. and W.H. Reid (1981). *Hydrodynamic stability.* p.246, Cambridge University Press, Cambridge, U.K..

Fowler, R.E. and R.A. Dalrymple (1990). Wave group forced nearshore circulation. *Proc.* 22^{nd} *Intl. Conf. Coast. Engrg.,* vol.1, Delft, The Netherlands, ASCE.

Garg, V.K. and Round G.F. (1978). Nonparallel effects on the stability of jet flows. *J. App. Mech.,* 45, 717-722.

Gourlay, M.R. (1976). Non-uniform alongshore currents. In: *Proc. of the 15th Coast. Eng. Conf.,* 701-720, ASCE.

Greenberg, M.D. (1988). *Advanced Engineering Mathematics,* Prentice-Hall, New Jersy.

Guza, R.T. and R.E. Davis (1974). Excitation of edge waves by waves incident on a beach. *J. Geophys. Res.,* 79, 1285-1291.

Haas, K.A., I.A. Svendsen, and M.C. Haller (1998). Numerical modeling of nearshore circulation on a barred beach with rip channels. In *Proceedings of the* 26^{th} *Intl. Conf. on Coast. Eng.* in press, Copenhagen, Denmark.

Haller, M.C., Dalrymple, R.A., and I.A. Svendsen (1996). Experimental investigation of nearshore circulation in the presence of rip channels. In *Transactions of the American Geophysical Union Fall Meeting, EOS suppl.*, p.394, San Francisco, California.

Haller, M.C., R.A. Dalrymple, and I.A. Svendsen, Rip channels and nearshore circulation. In *Proc. of Coastal Dynamics 1997*, pp.594-603, Plymouth, U.K..

Haller, M.C., R.A. Dalrymple, and I.A. Svendsen (1997). Experimental modeling of a rip current system. In *Proceedings of WAVES'97*, Virginia Beach, VA, 750-764, ASCE.

Haller, M.C. and R.A. Dalrymple (1998). Rip current instabilities. In *Transactions of the American Geophysical Union Fall Meeting, EOS suppl.*, p.401, San Francisco, California.

Hamm, L. (1992). Directional nearshore wave propagation over a rip channel: an experiment. In *Proc. of the* 23^{nd} *Intl. Conf. Coast. Engrg.,* 226-239.

Hammack, J., N. Scheffner, and H. Segur (1991). A note on the generation and narrowness of periodic rip currents. *J. Geophys. Res.,* 96, 4909-4914.

Harris, T.F.W. (1967). Field and model studies of nearshore circulation. Ph.D. Dissertation, University of Natal, 183 pp..

Hino, M. (1974). Theory on formation of rip current and cuspidal coast. *Proc. 13th Conf. Coastal Eng.,* 901-919.

Hoffman, J.D. (1992). *Numerical methods for engineers and scientists,* McGraw-Hill, New York.

Huntley, D.A., M.D. Hendry, J. Haines, and B. Greenidge (1988). Waves and rip currents on a Caribbean pocket beach. *J. Coast. Res.,* 4, 1, 69-79.

Huntley, D.A. and A.D. Short (1992). On the spacing between observed rip currents. *Coastal Eng.,* 17, 211-225.

Iwata, N. (1976). Rip current spacing. *J. Oceanogr. Soc. Jap.,* 32, 1-10.

Joshi, P.B. (1982). Hydromechanics of tidal jets, *J. Waterway, Port, Coast., and Ocean Eng.,* 239-253.

Keeley, J.R. and A.J. Bowen (1977). Longshore variations in the longshore current. *Can. J. Earth SCi.,* 14, 1897-1905.

Komar, P. D. (1971). Nearshore circulation and formation of giant cusps. *Geol. Soc. Am. Bull.,* 82:2643-2650.

LeBlond, P.H. and C.L. Tang (1974). On energy coupling between waves and rip currents. *J. Geophys. Res.,* 79, 811-816.

Longuet-Higgins, M.S. and R.W. Stewart (1970). Longshore currents generated by obliquely incident sea waves. Part 1 and 2. *J. Geophys. Res.,* 75, 6778-6789 and 6790-6801.

McKenzie, P. (1958). Rip current systems. *J. Geol.*, 66:103-113.

Mei, C.C. and P.L.-F. Liu (1977). Effects of topography on the circulation in and near the surf zone–Linearized theory. *J. Est. and Coastal Mar. Sci.,* 5, 25-37.

Miller, C. and A. Barcilon (1978). Hydrodynamic instability in the surf zone as a mechanism for the formation of horizontal gyres. *J. geophys. Res.,* 83, 4107-4116.

Mizuguchi, M. (1976). Eigenvalue problems for rip current spacing (in Japanese). *Trans. Jap. Soc. Civil Eng.,* 248, 83-88.

Nayfeh, A.H., W.S. Saric, and D.T. Mook (1974). Stability of non-parallel flows. *Archives of Mechanics,* Vol. 26, 401-406.

Noda, E.K. (1974). Wave-induced nearshore circulation. *J. Geophys. Res.,* 79, 4097-4106.

Putrevu U., J. Oltman-Shay, and I.A. Svendsen (1995). Effect of alongshore nonuniformities on longshore current predictions. *J. Geophys. Res., 100,* 16119-16130.

Rayleigh, Lord (1894). *The theory of sound.* 2nd ed., pp.. 380-1, London, Macmillan.

Reimintz, E., L.J. Toimil, F.P. Shepard, and M. Gutierrez-Estrana (1976). Possible rip current origin for bottom ripple zones to 30 m depth. *Geology,* 4:395-400.

Sancho, F.E.P., I.A. Svendsen, A.R. Van Dongeren, and U. Putrevu (1995). Longshore nonuniformities of nearshore currents. In *Proc. of Coastal Dynamics '95,* Gdansk, Poland, 425-436, ASCE.

Sasaki, T.O., H. Igarashi, and S. Harikai (1980). Nearshore currents on a partially rocky shore. In *Proc. 17th Conf. Coast. Engrg.,* 1071-1089, ASCE.

Schlichting, H. (1933). Laminare strahlenausbreitung. *ZAMM,* 13,260-263.

Shepard, F.P. (1936). Undertow, rip tides or rip currents. *Science*, Vol. 84, 181-182.

Shepard, F.P., K.O. Emery, and E.C. La Fond (1941). Rip currents: a process of geological importance. *J. Geol.,* 49:337:369.

Shepard, F.P. and D.L. Inman (1950). Nearshore water circulation related to bottom topography and wave refraction. *Trans. Am. Geophys. Union,* 31:196-212.

Shepard, F.P. and D.L. Inman (1951). Nearshore circulation. *Proc.* 1^{st} *Conf. Coast. Engrg.,* 50-59, ASCE.

Short, A.D. (1985). Rip-current type, spacing, and persistence, Narrabeen Beach, Australia. *Mar. Geol.,* 65:47-71.

Smith, J.A. and J.L. Largier (1995). Observations of nearshore circulation: rip currents. *J. Geophys. Res.,* 100, 10967-10975.

Sonu, C. J. (1972). Field observations of nearshore circulation and meandering currents. *J. Geophys. Res.,* 77, 3232-3247.

Sorensen, O.R., H.A. Schaffer, and P.A. Madsen (1998). Surf zone dynamics simulated by a Boussinesq type model. III. Wave-induced horizontal nearshore circulations. *Coastal Eng.,* 33, 155-176.

Svendsen, I.A. and K.A. Haas (1999). Interaction of undertow and rip currents. *COPEDEC 1999*, in press.

Tam, C.K.W. (1973). Dynamics of rip currents, *J. Geophys. Res.,* 78, 1937-1943.

Tang, E.C.-S., and R.A. Dalrymple (1989). Rip currents and wave groups. in *Nearshore Sediment Transport,* R. J. Seymour, Ed., Plenum Press, 205-230.

Tennekes, H. and J.L. Lumley (1972). *A first course in turbulence.* pp.113-114, MIT Press, Cambridge, MA.

Visser, P.J. (1984). Uniform longshore current measurements and calculations. In *Proc.* 19^{th} *Intl. Conf. Coast. Engrg.,* ASCE, vol.2, 2192-2208.

Wilmott, C.J. (1981). On the validation of models. *J. Phys. Oceanagr.,* 2(2), 219-232.

Wind, H.G. and C.B. Vreugdenhil (1986). Rip-current generation near structures. *J. Fluid Mech.,* 171, 459-476.

Wu, C.-S., E.B. Thornton, and R.T. Guza (1985). Waves and longshore currents: Comparison of a numerical model with field data. *J. Geophys. Res.,* 90, 4951-4958.

Zyserman, J., J. Fredsoe, and R. Deigaard (1990). Prediction of the dimensions of a rip current system on a coast with bars. In *Proc. 22nd Int. Conf. Coast. Eng.,* Delft, The Netherlands, 959-972, ASCE.

Appendix A

WAVE GAUGE LOCATIONS FOR ALL EXPERIMENTS

Table A.1: Location of wave gauges during Test B. Subscripts indicate gauge number; x,y are cross-shore and longshore distances in coordinate system defined in Chapter 2. All distances measured in meters.

run	x_1	y_1	x_{2-10}	y_2	y_3	y_4	y_5	y_6	y_7	y_8	y_9	y_{10}
1	4.0	13.2	11.0	16.7	15.7	14.7	13.65	12.7	11.2	10.2	9.2	8.2
2	4.0	13.2	11.0	16.7	15.7	14.7	13.65	12.7	11.2	10.2	9.2	8.2
3	4.0	13.2	11.0	16.7	15.7	14.7	13.65	12.7	11.2	10.2	9.2	8.2
4	4.0	13.2	11.0	16.7	15.7	14.7	13.65	12.7	11.2	10.2	9.2	8.2
5	4.0	13.2	11.0	16.7	15.7	14.7	13.65	12.7	11.2	10.2	9.2	8.2
6	4.0	13.2	11.0	16.7	15.7	14.7	13.65	12.7	11.2	10.2	9.2	8.2
7	4.0	13.2	11.0	16.7	15.7	14.7	13.65	12.7	11.2	10.2	9.2	8.2
8	4.0	13.2	11.0	16.7	15.7	14.7	13.65	12.7	11.2	10.2	9.2	8.2
9	4.0	13.2	11.0	16.7	15.7	14.7	13.65	12.7	11.2	10.2	9.2	8.2
10	4.0	13.2	11.0	16.7	15.7	14.7	13.65	12.7	11.2	10.2	9.2	8.2
11	4.0	13.2	12.4	16.7	15.7	14.7	13.65	12.7	11.2	10.2	9.2	8.2
12	4.0	13.2	13.0	16.7	15.7	14.7	13.65	12.7	11.2	10.2	9.2	8.2
13	4.0	13.2	13.5	16.7	15.7	14.7	13.65	12.7	11.2	10.2	9.2	8.2
14	4.0	13.2	14.0	16.7	15.7	14.7	13.65	12.7	11.2	10.2	9.2	8.2
15	4.0	13.2	11.4	16.7	15.7	14.7	13.65	12.7	11.2	10.2	9.2	8.2
16	4.0	13.2	11.4	16.7	15.7	14.7	13.65	12.7	11.2	10.2	9.2	8.2
17	4.0	13.2	11.4	16.7	15.7	14.7	13.65	12.7	11.2	10.2	9.2	8.2
18	4.0	13.2	11.4	16.7	15.7	14.7	13.65	12.7	11.2	10.2	9.2	8.2
19	4.0	13.2	11.4	16.7	15.7	14.7	13.65	12.7	11.2	10.2	9.2	8.2
20	4.0	13.2	11.4	16.7	15.7	14.7	13.65	12.7	11.2	10.2	9.2	8.2

Table A.2: Location of wave gauges during Test B. Subscripts indicate gauge number; x,y are cross-shore and longshore distances in coordinate system defined in Chapter 2. All distances measured in meters.

run	x_1	y_1	x_{2-10}	y_2	y_3	y_4	y_5	y_6	y_7	y_8	y_9	y_{10}
21	4.0	13.2	11.4	16.7	15.7	14.7	13.65	12.7	11.2	10.2	9.2	8.2
22	4.0	13.2	11.4	16.7	15.7	14.7	13.65	12.7	11.2	10.2	9.2	8.2
23	4.0	13.2	11.4	16.7	15.7	14.7	13.65	12.7	11.2	10.2	9.2	8.2
24	4.0	13.2	11.4	16.7	15.7	14.7	13.65	12.7	11.2	10.2	9.2	8.2
25	4.0	13.2	11.4	16.7	15.7	14.7	13.65	12.7	11.2	10.2	9.2	8.2
26	4.0	13.2	11.4	16.7	15.7	14.7	13.65	12.7	11.2	10.2	9.2	8.2
27	4.0	13.2	11.4	16.7	15.7	14.7	13.65	12.7	11.2	10.2	9.2	8.2
28	4.0	13.2	11.4	16.7	15.7	14.7	13.65	12.7	11.2	10.2	9.2	8.2
29	4.0	13.2	8.0	16.7	15.7	14.7	13.65	12.7	11.2	10.2	9.2	8.2
30	4.0	13.2	12.5	17.7	15.2	14.25	13.85	13.35	13.2	12.2	11.2	9.2
31	6.0	16.2	12.75	17.7	15.2	14.25	13.85	13.35	13.2	12.2	11.2	9.2
32	6.0	16.2	13.25	17.7	15.2	14.3	13.9	13.4	13.25	12.2	11.2	9.2
33	6.0	16.2	13.75	17.7	15.2	14.3	13.9	13.4	13.25	12.2	11.2	9.2
34	6.0	16.2	13.75	17.7	15.2	14.3	13.9	13.4	13.25	12.2	11.2	9.2
35	6.0	16.2	12.2	17.7	15.2	14.3	13.9	13.4	13.25	12.2	11.2	9.2
36	6.0	16.2	12.2	17.7	15.2	14.3	13.9	13.4	13.25	12.2	11.2	9.2
37	6.0	16.2	12.2	17.7	15.2	14.3	13.9	13.4	13.25	12.2	11.2	9.2
38	6.0	16.2	12.2	17.7	15.2	14.3	13.9	13.4	13.25	12.2	11.2	9.2
39	6.0	16.2	10.0	17.7	15.2	14.3	13.9	13.4	13.25	12.2	11.2	9.2
40	6.0	16.2	10.5	17.7	15.2	14.3	13.9	13.4	13.25	12.2	11.2	9.2

Table A.3: Location of wave gauges during Test C. Subscripts indicate gauge number; x,y are cross-shore and longshore distances in coordinate system defined in Chapter 2. All distances measured in meters.

run	x_1	y_1	x_{2-10}	y_2	y_3	y_4	y_5	y_6	y_7	y_8	y_9	y_{10}
1	4.0	13.2	11.0	17.2	16.2	15.2	14.7	13.63	12.7	11.7	10.7	9.2
2	4.0	13.2	11.0	17.2	16.2	15.2	14.7	13.63	12.7	11.7	10.7	9.2
3	4.0	13.2	-	-	-	-	-	-	-	-	-	-
4	4.0	13.2	-	-	-	-	-	-	-	-	-	-
5	4.0	13.2	-	-	-	-	-	-	-	-	-	-
6	4.0	9.2	11.0	17.2	16.2	15.2	14.7	13.63	12.7	11.7	10.7	9.2
7	4.0	9.2	11.0	17.2	16.2	15.2	14.7	13.63	12.7	11.7	10.7	9.2
8	-	-	-	-	-	-	-	-	-	-	-	-
9	4.0	9.2	-	-	-	-	-	-	-	-	-	-
10	4.0	9.2	-	-	-	-	-	-	-	-	-	-
11	6.0	9.2	-	-	-	-	-	-	-	-	-	-
12	6.0	9.2	10.0	17.2	16.2	15.2	14.7	13.63	12.7	11.7	10.7	9.2
13	6.0	9.2	10.0	17.2	16.2	15.2	14.7	13.63	12.7	11.7	10.7	9.2
14	6.0	11.2	-	-	-	-	-	-	-	-	-	-
15	6.0	11.2	-	-	-	-	-	-	-	-	-	-
16	6.0	11.2	-	-	-	-	-	-	-	-	-	-
17	4.0	11.2	-	-	-	-	-	-	-	-	-	-
18	4.0	11.2	-	-	-	-	-	-	-	-	-	-
19	4.0	11.2	-	-	-	-	-	-	-	-	-	-
20	7.0	9.2	-	-	-	-	-	-	-	-	-	-

Table A.4: Location of wave gauges during Test C. Subscripts indicate gauge number; x,y are cross-shore and longshore distances in coordinate system defined in Chapter 2. All distances measured in meters.

run	x_1	y_1	x_{2-10}	y_2	y_3	y_4	y_5	y_6	y_7	y_8	y_9	y_{10}
21	7.0	9.2	11.4	17.2	16.2	15.2	14.7	13.63	12.7	11.7	10.7	9.2
22	7.0	9.2	11.4	17.2	16.2	15.2	14.7	13.63	12.7	11.7	10.7	9.2
23	7.0	9.2	-	-	-	-	-	-	-	-	-	-
24	9.0	9.2	-	-	-	-	-	-	-	-	-	-
25	9.0	9.2	-	-	-	-	-	-	-	-	-	-
26	6.0	17.2	10.0	17.2	16.2	15.2	14.7	13.63	12.7	11.7	10.7	9.2
27	8.0	12.2	13.0	17.2	16.2	15.2	14.7	13.63	12.7	11.7	10.7	9.2
28	9.0	13.63	12.45	17.2	16.2	15.2	14.7	13.63	12.7	11.7	10.7	9.2
29	9.0	13.63	12.8	17.2	16.2	15.2	14.7	13.63	12.7	11.7	10.7	9.2
30	10.0	13.63	13.15	17.2	16.2	15.2	14.7	13.63	12.7	11.7	10.7	9.2
31	8.0	13.63	-	-	-	-	-	-	-	-	-	-
32	8.0	13.63	-	-	-	-	-	-	-	-	-	-
33	8.0	16.2	10.8	17.2	16.2	15.2	14.7	13.63	12.7	11.7	10.7	9.2
34	7.0	9.2	-	-	-	-	-	-	-	-	-	-

Table A.5: Location of wave gauges during Tests D-G. Subscripts indicate gauge number; x,y are cross-shore and longshore distances in coordinate system defined in Chapter 2. All distances measured in meters.

run	x_1	y_1	x_{2-10}	y_2	y_3	y_4	y_5	y_6	y_7	y_8	y_9	y_{10}
1	7.0	9.2	13.0	17.2	16.2	15.2	14.7	13.63	12.7	11.7	10.7	9.2
2	8.0	9.2	12.8	17.2	16.2	15.2	14.7	13.63	12.7	11.7	10.7	9.2
3	8.0	13.63	10.0	17.2	16.2	15.2	14.7	13.63	12.7	11.7	10.7	9.2
4	7.0	13.63	11.15	17.2	16.2	15.2	14.7	13.63	12.7	11.7	10.7	9.2
5	9.0	13.63	10.8	17.2	16.2	15.2	14.7	13.63	12.7	11.7	10.7	9.2
6	9.0	9.2	12.55	17.2	16.2	15.2	14.7	13.63	12.7	11.7	10.7	9.2
7	6.0	9.2	13.15	17.2	16.2	15.2	14.7	13.63	12.7	11.7	10.7	9.2
8	6.0	12.2	13.3	17.2	16.2	15.2	14.7	13.63	12.7	11.7	10.7	9.2
9	6.0	13.63	-									
10	7.0	12.2	11.0	17.2	16.2	15.2	14.7	13.63	12.7	11.7	10.7	9.2
11	8.0	12.2	10.4	17.2	16.2	15.2	14.7	13.63	12.7	11.7	10.7	9.2
12	7.0	17.2	9.0	17.2	16.2	15.2	14.7	13.63	12.7	11.7	10.7	9.2
13*	7.0	17.2	9	17.2	16.2	15.2	14.7	13.63	12.7	11.7	10.7	9.2

Appendix B

ADV LOCATIONS FOR ALL EXPERIMENTS

Table B.1: Location of ADV's during Test B. Subscripts indicate sensor number; x,y are cross-shore and longshore distances in coordinate system defined in Chapter 2. All distances measured in meters.

run	x_1	x_2	x_3	y_1	y_2	y_3	z_1	z_2	z_3
1	10.85	10.85	10.85	13.15	13.75	14.15	0.03	0.03	0.03
2	14.0	13.0	12.3	8.2	8.2	8.2	0.03	0.03	0.03
3	14.0	13.0	12.3	9.2	9.2	9.2	0.03	0.03	0.03
4	14.0	13.0	12.3	10.2	10.2	10.2	0.03	0.03	0.03
5	14.0	13.0	12.3	11.2	11.2	11.2	0.03	0.03	0.03
6	14.0	13.0	12.3	12.2	12.2	12.2	0.03	0.03	0.03
7	14.0	13.0	12.3	15.2	15.2	15.2	0.03	0.03	0.03
8	14.0	13.0	12.3	16.2	16.2	16.2	0.03	0.03	0.03
9	14.0	13.0	12.3	6.2	6.2	6.2	0.03	0.03	0.03
10	14.0	13.0	12.3	3.2	3.2	3.2	0.03	0.03	0.03
11	12.25	12.25	12.25	13.15	13.75	14.15	0.03	0.03	0.03
12	12.85	12.85	12.85	13.15	13.75	14.15	0.03	0.03	0.03
13	13.35	13.35	13.35	13.15	13.75	14.15	0.03	0.03	0.03
14	13.85	13.85	13.85	13.15	13.75	14.15	0.025	0.025	0.025
15	11.25	11.25	11.25	13.15	13.75	14.15	0.03	0.03	0.03
16	11.25	10.0	9.0	16.2	16.2	16.2	0.03	0.03	0.03
17	11.25	10.0	9.0	15.2	15.2	15.2	0.03	0.03	0.03
18	11.25	10.0	9.0	14.2	14.2	14.2	0.03	0.03	0.03
19	11.25	10.0	9.0	13.65	13.65	13.65	0.03	0.04	0.05
20	11.25	10.0	9.0	13.65	13.65	13.65	0.06	0.08	0.10

Table B.2: Location of ADV's during Test B. Subscripts indicate sensor number; x,y are cross-shore and longshore distances in coordinate system defined in Chapter 2. All distances measured in meters.

run	x_1	x_2	x_3	y_1	y_2	y_3	z_1	z_2	z_3
21	11.25	10.0	9.0	13.65	13.65	13.65	0.09	0.12	0.15
22	11.25	10.0	9.0	13.2	13.2	13.2	0.03	0.03	0.03
23	11.25	10.0	9.0	12.2	12.2	12.2	0.03	0.03	0.03
24	11.25	10.0	9.0	11.2	11.2	11.2	0.03	0.03	0.03
25	11.25	10.0	9.0	10.2	10.2	10.2	0.03	0.03	0.03
26	11.25	10.0	9.0	9.2	9.2	9.2	0.03	0.03	0.03
27	11.25	10.0	9.0	8.2	8.2	8.2	0.03	0.03	0.03
28	11.25	10.0	9.0	6.2	6.2	6.2	0.03	0.03	0.03
29	10.0	10.3	10.5	13.65	13.65	13.65	0.10	0.10	0.10
30	11.5	11.8	12.0	12.95	12.95	12.95	0.03	0.03	0.03
31	11.5	11.8	12.0	13.13	13.13	13.13	0.03	0.03	0.03
32	11.5	11.8	12.0	13.3	13.3	13.3	0.03	0.03	0.03
33	11.5	11.8	12.0	13.5	13.5	13.5	0.03	0.03	0.03
34	11.5	11.8	12.0	13.5	13.5	13.5	0.03	0.03	0.03
35	11.5	11.8	12.0	13.72	13.72	13.72	0.03	0.03	0.03
36	11.5	11.8	12.0	13.95	13.95	13.95	0.03	0.03	0.03
37	11.5	11.8	12.0	14.13	14.13	14.13	0.03	0.03	0.03
38	11.5	11.8	12.0	14.37	14.37	14.37	0.03	0.03	0.03
39	12.4	12.65	12.8	12.2	12.2	12.20	0.03	0.03	0.03
40	12.4	12.65	12.8	14.58	14.58	14.58	0.03	0.03	0.03

Table B.3: Location of ADV's during Test C. Subscripts indicate sensor number; x,y are cross-shore and longshore distances in coordinate system defined in Chapter 2. All distances measured in meters.

run	x_1	x_2	x_3	y_1	y_2	y_3	z_1	z_2	z_3
1	10.88	10.88	10.88	13.2	13.0	12.8	0.03	0.03	0.03
2	10.88	10.88	10.88	13.9	13.7	13.5	0.03	0.03	0.03
3	10.88	10.88	10.88	14.4	14.2	14.0	0.03	0.03	0.03
4	10.3	10.5	10.7	13.0	13.0	13.0	0.03	0.03	0.03
5	10.3	10.5	10.7	13.2	13.2	13.2	0.03	0.03	0.03
6	10.3	10.5	10.7	13.4	13.4	13.4	0.03	0.03	0.03
7	10.3	10.5	10.7	13.6	13.6	13.6	0.03	0.03	0.03
8	10.3	10.5	10.7	13.7	13.7	13.7	0.03	0.03	0.03
9	10.3	10.5	10.7	13.9	13.9	13.9	0.03	0.03	0.03
10	10.3	10.5	10.7	14.2	14.2	14.2	0.03	0.03	0.03
11	10.3	10.5	10.7	14.4	14.4	14.4	0.03	0.03	0.03
12	11.3	11.5	11.7	12.8	12.8	12.8	0.03	0.03	0.03
13	11.3	11.5	11.7	13.0	13.0	13.0	0.03	0.03	0.03
14	11.3	11.5	11.7	13.2	13.2	13.2	0.025	0.025	0.025
15	11.3	11.5	11.7	13.4	13.4	13.4	0.03	0.03	0.03
16	11.3	11.5	11.7	13.6	13.6	13.6	0.03	0.03	0.03
17	11.3	11.5	11.7	13.7	13.7	13.7	0.03	0.03	0.03
18	11.3	11.5	11.7	13.9	13.9	13.9	0.03	0.03	0.03
19	11.3	11.5	11.7	14.2	14.2	14.2	0.03	0.04	0.05
20	11.3	11.5	11.7	14.4	14.4	14.4	0.06	0.08	0.10

Table B.4: Location of ADV's during Test C. Subscripts indicate sensor number; x,y are cross-shore and longshore distances in coordinate system defined in Chapter 2. All distances measured in meters.

run	x_1	x_2	x_3	y_1	y_2	y_3	z_1	z_2	z_3
21	10.3	10.5	10.7	12.8	12.8	12.8	0.03	0.03	0.03
22	10.3	10.5	10.7	12.6	12.6	12.6	0.03	0.03	0.03
23	9.6	10.5	10.7	12.6	12.6	12.6	0.03	0.03	0.03
24	9.6	10.5	10.7	13.63	13.63	13.63	0.03	0.03	0.03
25	9.6	10.5	10.7	14.4	14.4	14.4	0.03	0.03	0.03
26	12.3	10.5	10.7	9.2	9.2	9.2	0.03	0.03	0.03
27	12.3	10.5	10.7	12.2	12.2	12.2	0.03	0.03	0.03
28	12.3	10.5	10.7	11.8	11.45	11.2	0.03	0.03	0.03
29	12.65	10.5	10.7	11.8	11.45	11.2	0.03	0.03	0.03
30	13.0	10.5	10.7	11.8	11.45	11.2	0.03	0.03	0.03
31	13.15	10.5	10.7	11.8	11.45	11.2	0.03	0.03	0.03
32	13.4	10.5	10.7	11.8	11.45	11.2	0.03	0.03	0.03
33	12.2	10.5	10.7	11.8	11.45	11.2	0.03	0.03	0.03
34	11.5	10.5	10.7	13.6	13.6	13.6	0.03	0.03	0.03

Table B.5: Location of ADV's during Tests D-G. Subscripts indicate sensor number; x,y are cross-shore and longshore distances in coordinate system defined in Chapter 2. All distances measured in meters.

run	x_1	x_2	x_3	y_1	y_2	y_3	z_1	z_2	z_3
1	11.5	11.7	12.0	13.6	13.6	13.6	0.03	0.03	0.03
2	11.5	11.7	12.0	13.0	13.0	13.0	0.03	0.03	0.03
3	11.5	11.7	12.0	14.2	14.2	14.2	0.03	0.03	0.03
4	12.65	12.65	12.65	11.8	11.45	11.2	0.03	0.03	0.03
5	12.2	12.2	12.2	11.8	11.45	11.2	0.03	0.03	0.03
6	12.4	12.4	12.4	11.8	11.45	11.2	0.03	0.03	0.03
7	13.0	13.0	13.0	11.8	11.45	11.2	0.03	0.03	0.03
8	13.15	13.15	13.15	11.8	11.45	11.2	0.03	0.03	0.03
9	13.4	13.4	13.4	11.8	11.45	11.2	0.03	0.03	0.03
10	12.3	12.65	13.4	9.2	9.2	9.2	0.03	0.03	0.03
11	12.3	12.65	13.4	15.2	15.2	15.2	0.03	0.03	0.03
12	10.9	11.2	11.5	9.2	9.2	9.2	0.03	0.03	0.03
13*	10.9	11.2	11.5	9.2	9.2	9.2	0.03	0.03	0.03